Ion Impact Chemistry in the System Ti-O

Ion Impact Chemistry in the System Ti-O

by

THOMAS E. PARKER, B.Eng.

A Thesis
Submitted to the School of Graduate Studies
in Partial Fulfilment of the Requirements
for the Degree
Master of Engineering

McMaster University

April, 1973

TO BEVERLEY

MASTER OF ENGINEERING
(Metallurgy and Materials Science)

McMASTER UNIVERSITY
Hamilton, Ontario

TITLE: Ion Impact Chemistry in the System Ti-O

AUTHOR: Thomas E. Parker, B.Eng. (McMaster University)

SUPERVISOR: Professor Roger Kelly

NUMBER OF PAGES: xiv, 150

SCOPE AND CONTENTS:

This thesis considers the characterization of the phenomenon of the induced conductivity changes in TiO_2 under the influence of krypton and oxygen ion bombardment and the damage layer associated with these changes. The investigation included the examination of irradiated and unirradiated specimens (variously-single crystals and polycrystals), using electron microscopy techniques to reveal surface structural alterations; electrical conductivity measurements to assess the response to irradiation; dissolution experiments of the bombarded region to estimate the thickness and radioactive inert gas marker release to monitor the annealing stages of the damage.

The results include the observation of lower oxide formation under ion impact and its identification as Ti_2O_3 and suggest a technique for producing lower oxides of transition metal oxides that have a semiconductor to metal transition of technological interest.

ACKNOWLEDGMENTS

I wish to express my sincere appreciation to Professor Roger Kelly for his continuing interest in this project during the past two years. His contagious enthusiasm for experimental work and the stimulating discussions have made the time most rewarding and enjoyable.

I would be truly remiss if I did not acknowledge Ms. Beverley Spence who imparted a sense of balance to this academic endeavour.

I also wish to thank Hussein M. Naguib (now at Cairo University) for his experimental assistance at the outset of the investigation.

This project was supported by a generous grant from the Geological Survey of Canada, Ottawa to Dr. Kelly and by an equally generous McMaster University Dalley Fellowship to the author.

TABLE OF CONTENTS

Page

APPENDICES

Page

LIST OF ILLUSTRATIONS

Page

Page

LIST OF TABLES

SECTION 1

Introductory Comments

The ion bombardment of solids (oxides and metals) is well known to cause the following processes to occur: (i) - ejection of surface atoms from the solid (sputtering), (ii) - radiation damage in the near-surface region as a result of the particle energy being dissipated along its range, (iii) - surface changes in terms of the growth of characteristic topographies and (iv) - occasional deeper lying effects due to radiation enhanced diffusion or channeling. A plethora of experimental work can be found in the literature concerning a wide range of ion types, ion energies, and substrates. From these results, as reviewed for example by Navinšek |6|, one can conclude that a criterion based upon the total dose or fluence of the bombarding species seems reasonable in the characterization of the damage. In particular, for the case of heavy-ion bombardment three general dose regions are evident:

(I) $<10^{15}$ ions/cm^2

(II) $10^{15} - 10^{17}$ ions/cm^2

(III) $>10^{17}$ ions/cm^2

For dose levels in Region I ($<10^{15}$ ions/cm^2) the damage may be said to be "atomic" in that it consists of individual point defects, clusters, and extended defects (e.g. dislocations, loops, stacking faults) |1,2|. In Region II (10^{15} - 10^{17} ions/cm^2), the damage may consist of amorphization |3,4|, crystallization of amorphous zones |5|, or large clusters and hence is of a microscopic nature. Region III (>10^{17} ions/cm^2) or the so called "high" dose level includes topographical alterations such as the generation of facets, grooves and steps |6|, and chemical changes at the surface or in the interior |7,8|. It is particularly with this "high" dose region of ion bombardment that the observations of this thesis are concerned.

Previous high dose experiments at McMaster and elsewhere including the bombardment of unary and binary targets have yielded information about the particle-solid interactions and induced damage generally in terms of two macroscopic properties, (a) the electrical conductivity since it is sensitive to radiation damage and is readily measured and (b) the (crystal) structure before and after bombardment. One might expect the same general trend in the changes of either of these properties with ion bombardment of various targets, for example, intuitively, such that radiation damage (lattice disruption) causes a decrease in conductivity. However, experiments indicate that drastic increases or decreases in electrical conductivity may occur. For instance, V_2O_5 and MoO_3 |8| under the influence of Kr bombardment exhibited striking electrical conductivity increases by factors of 5×10^5 and 10^{13} respectively; hydrogen ion bombardment of Al_2O_3 and MgO to doses greater than 10^{17} ions |9| caused a factor of 10^6 increase in the conductivity which annealed within minutes at room temperature; 65 KeV Ne bombardment (10^{17} ions) of ZrO_2 |10| yielded increased conductivity and a subsequent enhanced oxidation rate of oxide-metal sandwiches. Alternatively, neutron bombardment of Cr_2O_3 |11| caused a significant electrical conductivity decrease, a result also true of the neutron bombardment of U_3Si |12| and Ne-bombarded Si |4|.

Examples of structural alterations indicate an equally diverse response to bombardment. 10 KeV oxygen ion bombardment of FeS_2 |13| to a dose of 7×10^{16} ions yielded a double layer structure of Fe_3O_4 on the FeS_2 substrate; Cu single crystals exposed to 10 KeV oxygen ions |14,15| produced a surface oxide of Cu_2O characterized by the relation (100) Cu_2O// (100) Cu compared to the usual relationship (111) Cu_2O//(100) Cu for thermal oxide; Kr bombardment of MoO_3 and V_2O_5 |8| resulted in preferential oxygen loss and crystallization to lower oxides whereas many cubic binary substances (e.g. CaO, NiO and CaF_2) are generally insensitive to irradiation |56|. Furthermore, structural alterations were not confined to the outer surface. Oxygen ion irradiation of LiF |37| produced platelets of Li on $\{100\}_{LiF}$ planes, a result also shown for thermal neutron irradiation (thence fissioning) of LiF |36|.

One final rather unique response to irradiation is the case of high temperature N^+ bombardment (7×10^{17} ions/cm^2)

of high purity molybdenum in which voids were produced and formed a regular body-centred cubic superlattice in the target |7|.

Clearly then the types of material behaviour in an energetic ion beam taken to high doses are diverse and complex, and in the spirit of these opening comments, this thesis addresses itself to the problem of characterizing the induced conductivity hence radiation damage in the transition metal oxide TiO_2 (rutile) under the influence of inert gas (Kr) and oxygen ion bombardment.

SECTION 2

The Structural and Electrical Conductivity Changes in TiO_2 Sintered Pellets under Kr-ion Bombardment

2.1 Introductory comments

Radiation-damage effects may be conveniently measured, albeit indirectly, by measuring the electrical conductivity as a function of the total dose or "fluence" of the bombarding species. This procedure was adopted in investigating the Kr and oxygen ion radiation response of bulk polycrystalline TiO_2(rutile), and subsequently, in conjunction with electron diffraction examination of the surface, the electrical conductivity changes were reconciled with the structural alterations observed.

This section describes the experimental procedure used and the results obtained from bulk samples of the oxide.

2.2 Specimen preparation

The initial experiments involved using TiO_2 in the form of sintered pellets approximately 10 mm in diameter and 5mm in height in the unfired condition. However in the sintered condition, pellets pressed from the chemically pure oxide powder (Table 2-I(A)) were subject to surface and bulk cracking due to density gradients introduced during the pressing operation. Since a discontinuous surface is unacceptable for conductivity measurements, an organic binder, which would readily volatilize during heating, was introduced into the oxide powder prior to pressing†. The resultant pellets were fired at 1280°C ($\sim .74\ T_{melting}$) for a period of 24 hours, then furnace cooled to room temperature. All firings were in air at this relatively low temperature to avoid serious oxygen loss from the specimens. Subsequently, the pellets were ground to produce the necessary smooth surface for four-point probe electrical conductivity measurements |48,49|. Refiring to 1000°C for 1 hour followed by furnace cooling annealed the surface damage introduced by the mechanical treatment.

2.2.1 Surface structure determination - In order to verify that the sinters were in fact TiO_2 and substantially unaltered by using a binder, structural determinations were made using the back reflection electron diffraction mode (BRD) of the Philips EM 300 electron microscope, (which is particularly amenable to surface structure evaluations) operated usually at 80 KV corresponding to a camera constant λL, of 1.48 ± .02 Å-cm. The diffraction patterns of pellets without and with the binder are shown in Figures 2.1 and 2.2 respectively. The respective analyses are given (Table 2-I(B)) and include the deviation from the accepted "d" values for rutile. Experimental and

---

† In this case the binder was triethylene glycol, although the choice was arbitrary.

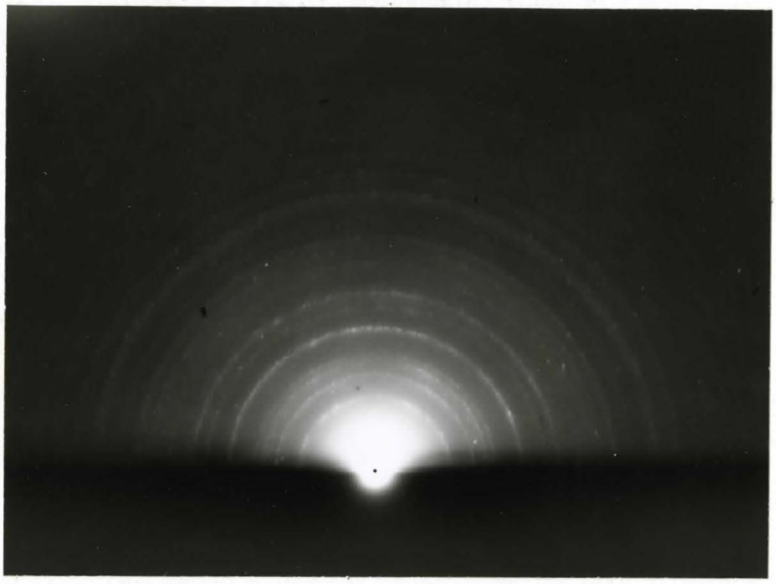

Figure 2.1 Sintered TiO_2 powder (no binder) using back reflection electron diffraction (BRD).

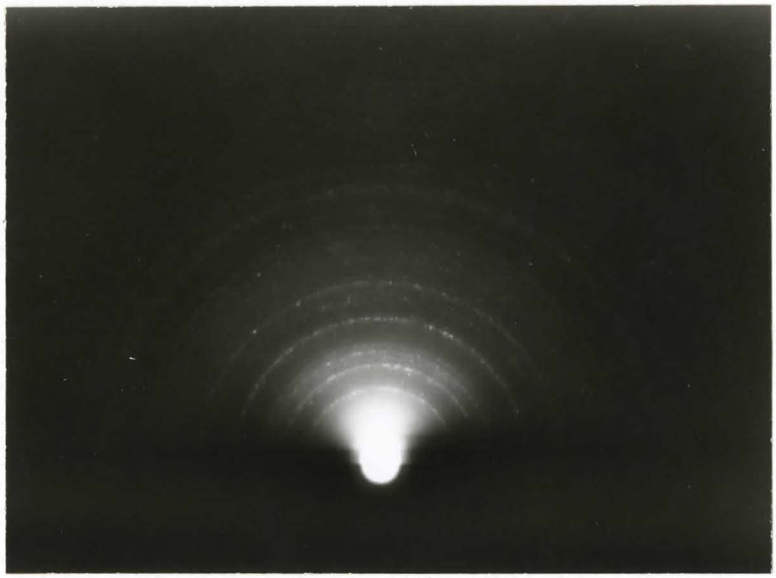

Figure 2.2 Sintered TiO_2 powder (binder - Triethylene glycol).

TABLE 2-I(A) TiO_2* (anhydrous)
chemical analysis

water soluble salts	0.02%
arsenic (As)	0.0001%
iron (Fe)	0.005%
lead (Pb)	0.002%
zinc (Zn)	0.002%

* Fisher Scientific Co., New Jersey, U.S.A.

accepted planar (d) spacings indicate that the surface, the region of interest, was of a fine polycrystalline TiO_2 rutile structure, a result that was established by comparison with the intensities and "d" spacings of some 16 members of the Ti-O system. (Refer to Appendix I for an electron microscopy analysis discussion and Ti-O oxide data.)

2.2.2 Surface appearance - The light buff coloured sintered pellets exhibited a fine grain size as illustrated by the light microscope micrograph of Figure 2.3 and the scanning electron micrograph of Figure 2.4. Except for the largest grains, the surface is a rather open network of 1-5μ grains joined by necks formed during sintering.

2.2.3 Electrical conductivity (σ) of the sintered pellets -

Determination of σ by a linear four-point D.C. probe technique and analysis using the appropriate Valdes relation

TABLE 2-I(B) Analyses of BRD patterns of sintered TiO_2 pellets

(a) Sintered TiO_2 powder (no binder) Fig. 2.1				(b) Sintered TiO_2 powder + binder (Triethylene glycol) Fig. 2.2				(c) Data for TiO_2 (rutile)†		
Ring #	I/Io (expt'l)	d (expt'l) (Å)	Error (%)	Ring #	I/Io (expt'l)	d (expt'l) (Å)	Error (%)	I/Io	d (Å)	{hkl}
1	80	3.31	+1.8	1	100	3.32	+2.1	80	3.252	110
2	40	2.54	+2.0	2	60	2.56	+2.8	60	2.490	101
								20	2.298	200
3	40	2.21	+0.9	3	60	2.23	+1.8	40	2.190	111
4	40	2.07	+0.7					40	2.055	210
5	100	1.70	+0.6	4	100	1.71	+1.2	80	1.689	211
								60	1.625	220
6	20	1.47	-0.7	5 (doublet)	40	1.49	+0.7	40	1.481	002
						1.44	-1.0	40	1.454	310
7	80	1.35	-0.8	6	60	1.36	-0.1	40	1.361	301
								20	1.348	112

† X-ray data |44|

Figure 2.3 Light micrograph of a sintered TiO_2 pellet surface (800x).

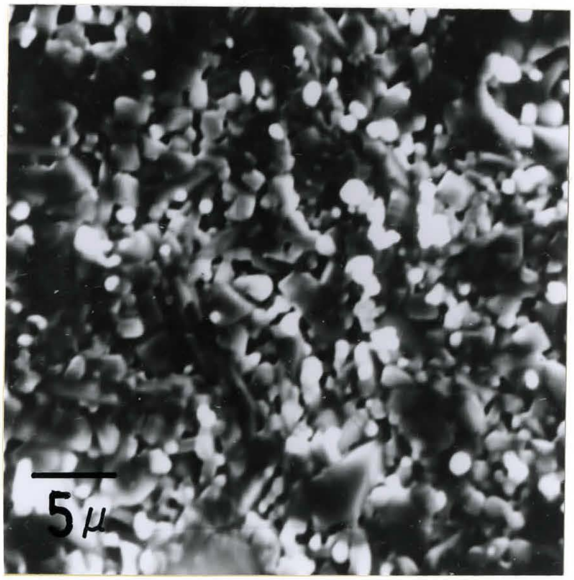

Figure 2.4 SEM micrograph of sintered TiO_2 pellet surface (2150x).

(Equation II-2, Appendix II) confirmed the expected essentially non-conductive nature of the pellets with σ(bulk) typically $\sim 1 \times 10^{-7}$ ohms^{-1}-cm^{-1}. Literature values of σ for single crystal rutile at 300°K are 10^{-8} ohm^{-1}-cm^{-1} |17|, and 10^{-7} ohm^{-1}-cm^{-1} |16|.

2.3 Experimental results of the low current Kr-ion bombardment of TiO_2

2.3.1 Colour changes - On subjecting the pellets to 30 KeV, 6 μamp, Kr-ion bombardment at R.T. the obvious observation was that the colour of the exposed surface gradually changed with ion dose from the initial buff to a final dark grey at the highest doses ($>10^{17}$ ions/cm^2). This type of colour change had previously been observed for V_2O_5 and MoO_3 |8| and subsequently for Nb_2O_5 |18| and WO_3 |19|. Figure 2.5 shows the striking changes for TiO_2 as well as WO_3 and V_2O_5. Colour change observations are summarized in Table 2-II. The colour change in TiO_2 was accompanied by an equally extreme change in the electrical conductivity.

TABLE 2-II A comparison of TiO_2, MoO_3, V_2O_5, WO_3 and Nb_2O_5 bombardment colours.

Oxide	Reference	Initial Colour	Final† Colour
TiO_2	this thesis	light buff	dark grey
MoO_3	|8|	pale yellow	black
V_2O_5	|8|	yellow	black
WO_3	|19|	pale green	black
Nb_2O_5	|18|	white	dark grey

† for the case of TiO_2 (as well as MoO_3, V_2O_5, Nb_2O_5 and WO_3) darkening is consistent with oxygen loss |20|.

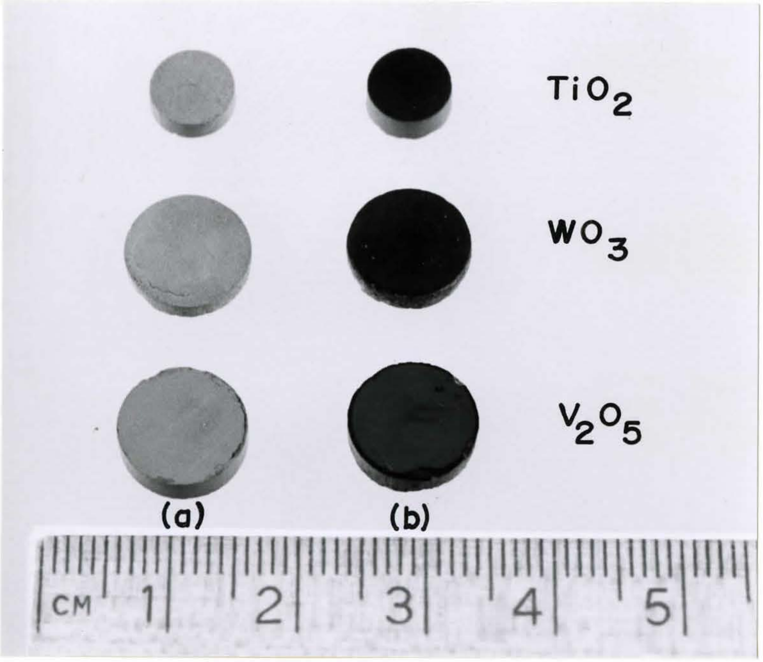

Figure 2.5 Colour change due to Kr ion bombardment

(a) before bombardment
(b) after bombardment of $>10^{17}$ ions/cm^2.

2.3.2 Electrical conductivity measurements - Typical results for a four-point D.C. probe measurement (refer to Appendix II) of the bombarded pellets are shown in Figure 2.6 (curve (A)) for the continuous 30 KeV, 6 μamp, Kr-ion bombardment of TiO_2 (i.e. every point represents a separate sample rather than one incremented sample). The ordinate is the recorded (I/V) value in units of ohm^{-1} and the abscissa, the ion dose or fluence in units of $\mu amp\text{-}min/cm^2$ as determined by measuring the ion beam current, time of exposure and beam area as discussed in Appendix III.

Each separate value of (I/V) represents an average of 18 measurements, which include 3 values of probe current within the ohmic response region, both polarities, and 3 positions on the sample in order to avoid or reduce serious error due to beam inhomogenieties and possible specimen polarization. Ordinate error bars included in Figure 2.6 represent ± 1 standard deviation about the mean value, while the abscissa error bars represent an estimated "worst" error in the dose of ±20%.

2.3.3 Ohmic behaviour - At every dose level except the very lowest ($<5\ \mu amp\text{-}min/cm^2$) the behaviour was ohmic an example of which is shown in Figure 2.7 for a 40 KeV Kr-ion bombardment to a dose of $290\ \mu amp\text{-}min/cm^2$ (1.5×10^{17} $ions/cm^2$). As shown, the ohmic response extended to approximately 1 mA and allowed a reliable (I/V) value to be found over that current range.

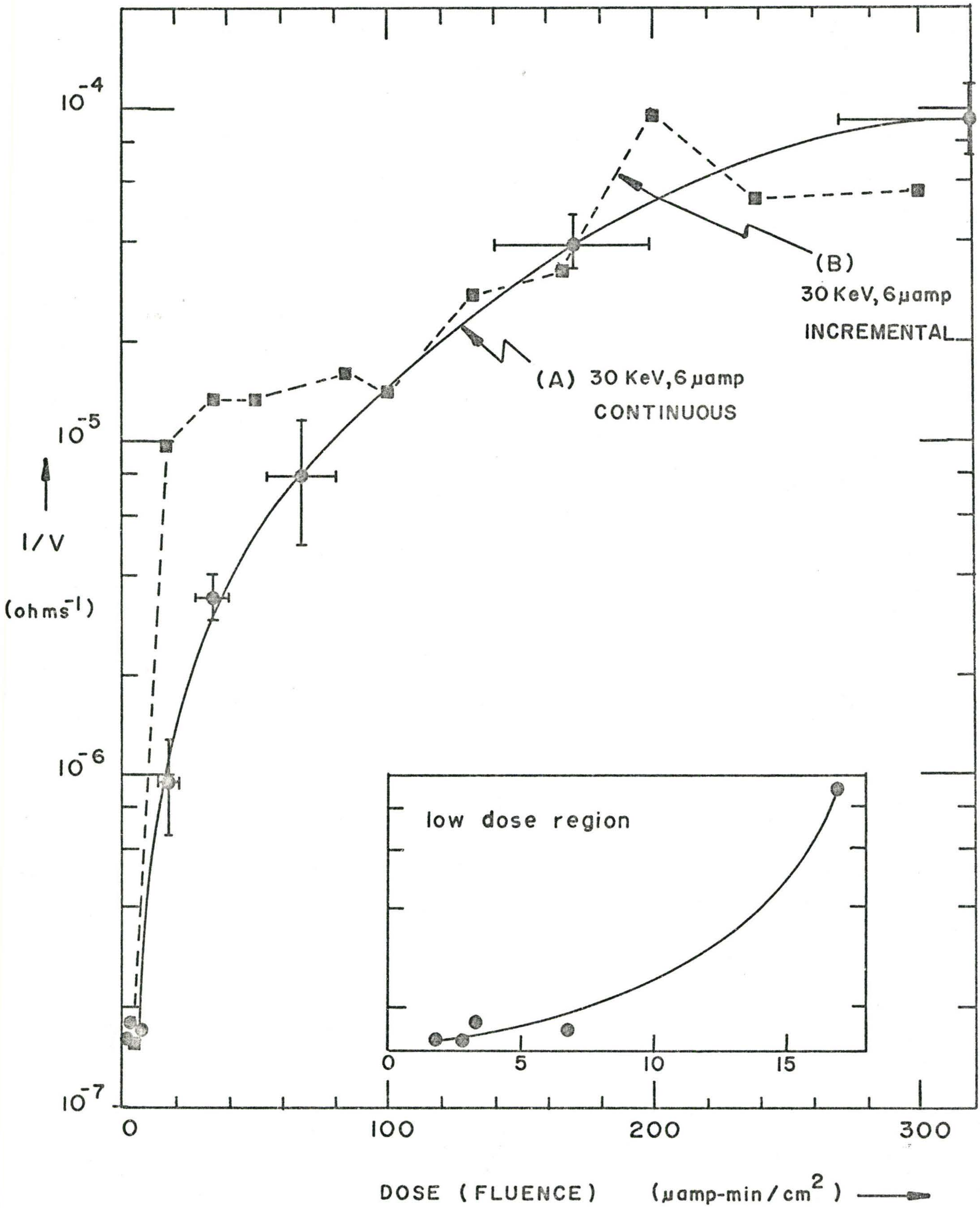

Figure 2.6 Induced conductivity (I/V) as a function of Kr-ion dose (Fluence):

(A) - continuous bombardment (B)-Incremental or step-wise bombardment

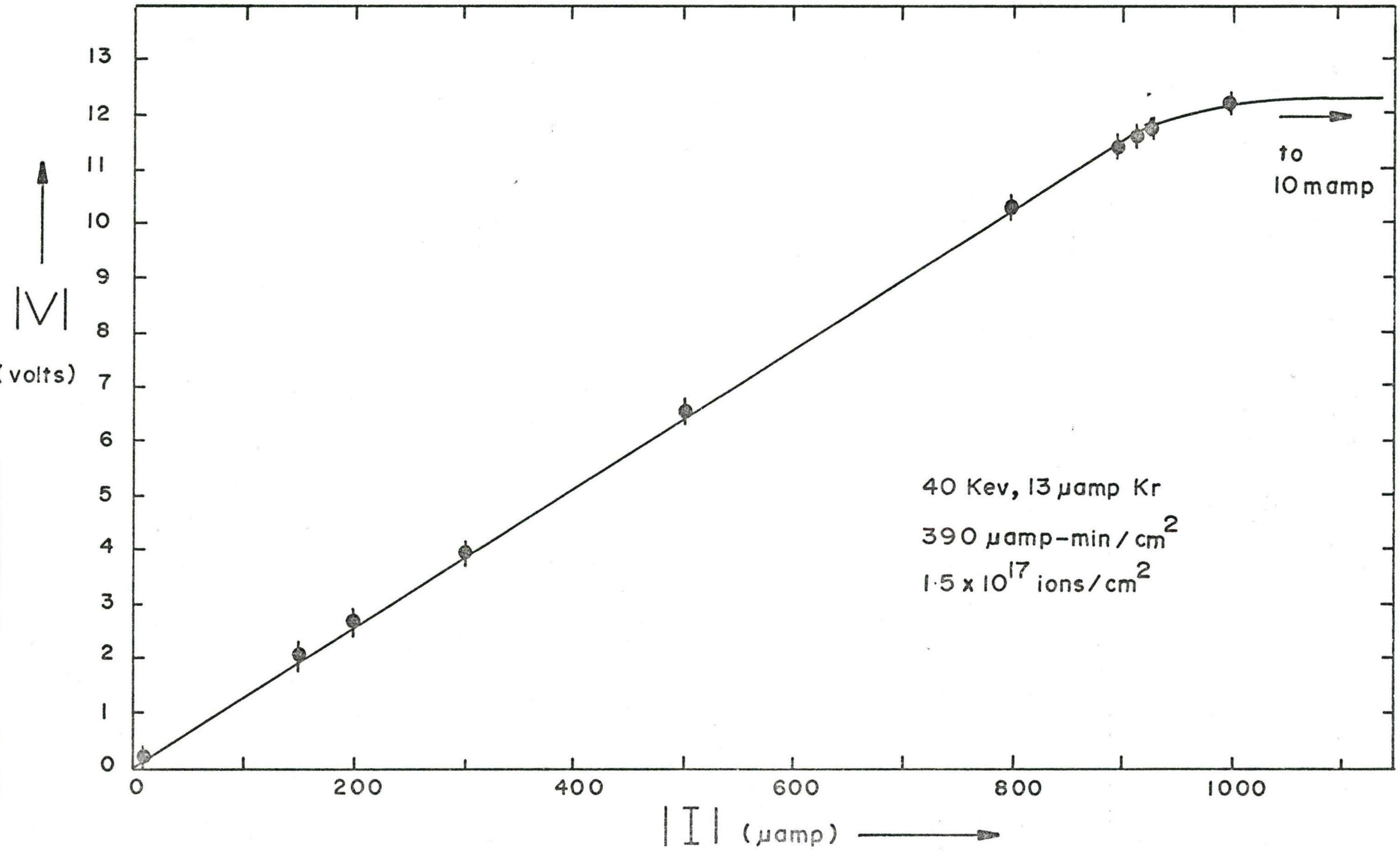

Figure 2.7 Ohmic response of a Kr bombarded TiO_2 pellet

2.3.4 Permanent nature of the induced conductivity - Intermittent (I/V) measurements of bombarded pellets over extended periods of time indicated no change in the induced conductivity level (Figure 2.8) within experimental error, unlike that for MoO_3 and V_2O_5 |8| which appeared to decrease significantly over short periods of time (days). The decrease for MoO_3 and V_2O_5, it is suggested could have been due in part to the destruction of the conductive layer by the movement of the probes on and off the sample especially since these oxides were quite soft in the sintered condition and the conductive layer was extremely thin (200-2000 Å |8|). This uncertainty does not arise in the case of TiO_2 due to the extreme hardness of the pellet compact, which retains the integrity of its surface through repeated conductivity measurements. Further, a comparison of the melting points of the three oxides indicates that one might possibly expect oxygen diffusion at R.T. hence a loss in conductivity, for MoO_3 ($Tm = 795^oC$) and V_2O_5 ($tm = 690^oC$) but certainly not for TiO_2 ($Tm = 1825^oC$), for which the conductivity remained unchanged. On the other hand, if diffusion occurred one would then expect the original colour to reappear, however this was not the case for TiO_2 nor for MoO_3 and V_2O_5.

2.3.5 Features of the (I/V) vs dose (fluence) graphs - The semi-log plot, Figure 2.6(A), illustrates the dramatic increase in the electrical conductivity which can be considered to be made up of three basic regions:

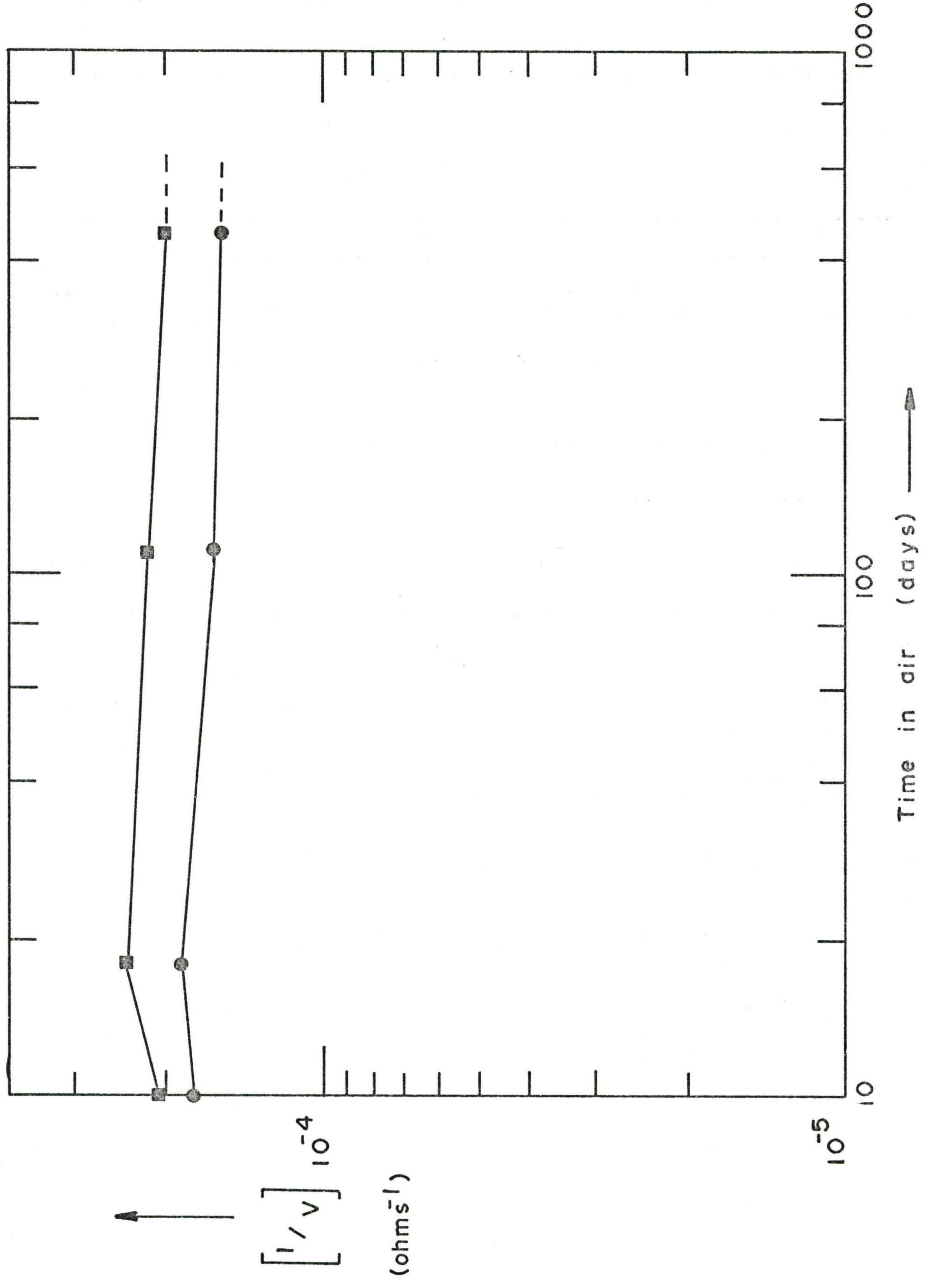
[1/V]
(ohms⁻¹)
10⁻⁴
10⁻⁵
10
100
1000
Time in air (days)

Region I - (<10 μamp-min/cm^2)
(<4 x 10^{15} ions/cm^2)

An incubation period in which (I/V) remained effectively at the low initial value of 10^{-7} ohm^{-1} (c.f. low dose region as discussed in Section 2.3.6).

Region II - (10 μamp-min/cm^2 < dose < 300 μamp-min/cm^2)
or (4 x 10^{15} ions/cm^2 < dose < 1.1x10^{17} ions/cm^2)

A rapid increase in the induced (I/V) through approximately three orders of magnitude to a saturation level of 1 x 10^{-4} ohm^{-1} at the upper limit. Similar values of 1-2 x 10^{17} ions/cm^2 to induce saturation were found also for MoO_3 and V_2O_5 |8|.

Region III - (>300 μamp-min/cm^2)
(>1.1x10^{17} ions/cm^2)

The induced (I/V) increase remained at a constant level of 1x10^{-4} ohm^{-1} and though not indicated in Figure 2.6 did so even to three times the dose to induce saturation. This phenomenon would be expected for a constant surface thickness of altered material, wherein the rate of production of newly altered oxide is balanced by the rate of sputtering or removal of the altered layer.

2.3.6 Low dose induced conductivity (<5 μamp-min/cm^2) - As previously stated the ohmic behaviour did not apply at the very lowest doses where the potential measured for a specified D.C. current fluctuated. This could have been due in part to high circuit noise at low I.

2.3.7 Incremental vs continuous bombardment - Although results of all bombardments (Figure 2.6 and Figure 2.9) with Kr of various energies and beam currents exhibited the same basic behaviour namely, a rapid increase in (I/V) to a saturation level, the continuous bombardment gave a more smooth response (c.f. Figure 2.6 curves (A) and (B)). Stepwise or incremental bombardment entailed irradiating one specimen incrementally and required opening the accelerator for each (I/V) measurement. Since the bombardment caused preferential oxygen loss, as shown in Section 2.3.8, repeated evacuation and pressurization could have affected the surface sputtering phenomena. Nevertheless, the incremental bombardments serve to reveal a significant discontinuity in the growth of (I/V) with dose, such that the (I/V) growth increase appears in some (though not all) experiments to change at 2-4 x 10^{16} ions/cm^2. This dose will be shown to correspond to that at which Ti_2O_3 first appears.

2.3.8 Surface structural changes during bombardment - The series of pellets used to generate Figure 2.6 curve (A) were investigated with respect to surface structure using the back reflection electron diffraction technique (BRD) |Appendix I|. Table 2-III summarizes the experimental parameters and the corresponding induced (I/V), surface structure and diffraction pattern results. Figure 2.10(a) is the diffraction pattern of TiO_2 (rutile) and is included as a comparison with the bombardment induced structures.

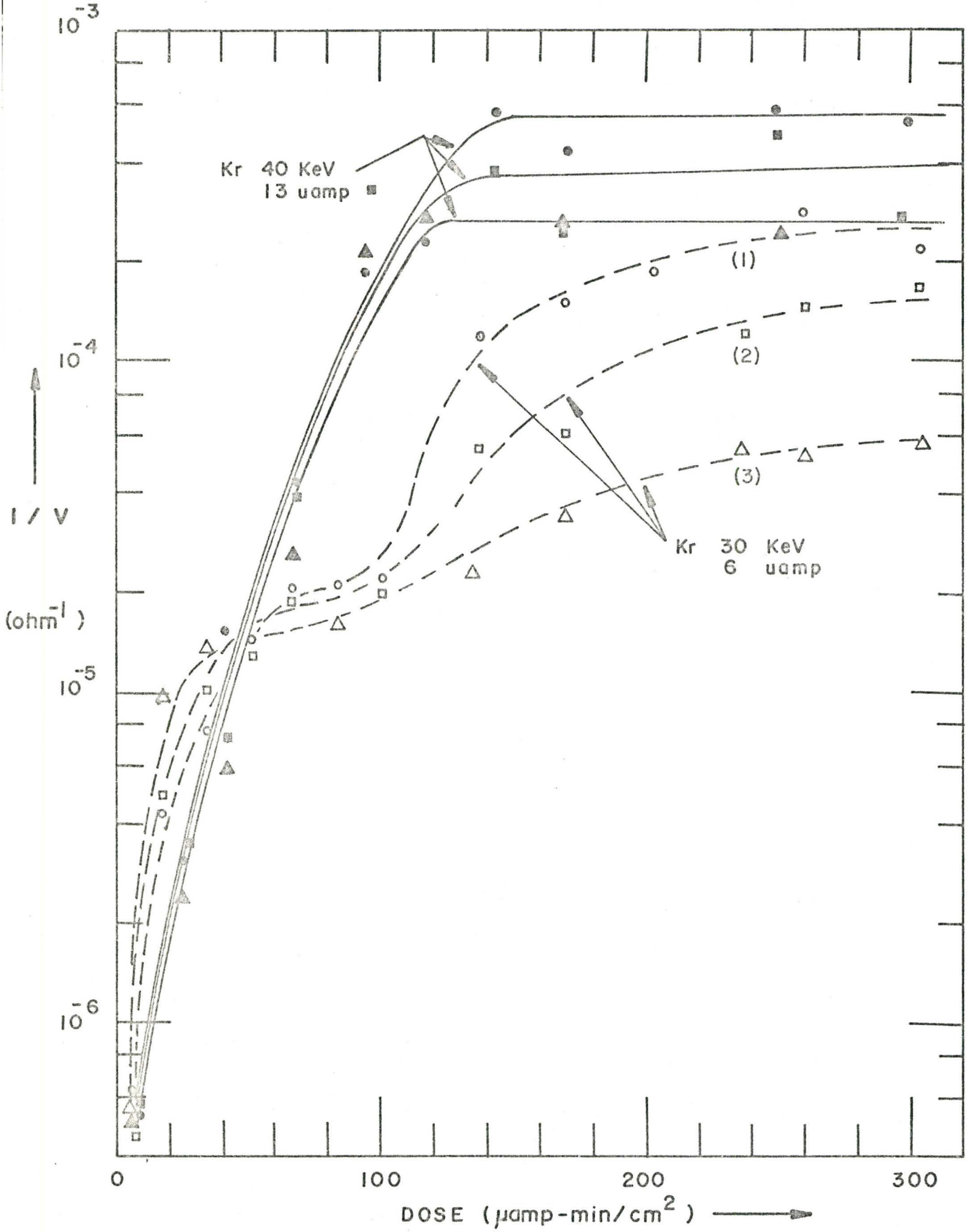

Figure 2.9 (I/V) response to Kr ion bombardment - TiO_2 pellets.

TABLE 2-III Structural and (I/V) development in a TiO_2 pellet bombarded with 30 KeV Kr ions

Accelerating Voltage (KeV)	Ion Beam Current (μamp)	Dose (fluence) μamp-min/cm²	Dose (fluence) ions/cm²	Induced Conductivity (I/V)	Structure	Fig.
30	6	0	0	-	Rutile TiO_2	2.10(a)
"	"	1.7	6.3×10^{14}	1.6×10^{-7}	cryst + amor*	
"	"	3.4	1.3×10^{15}	1.8×10^{-7}	cryst + amor	
"	"	6.8	2.5×10^{15}	1.7×10^{-7}	all amor	2.10(b)
"	"	17	6.4×10^{15}	9.4×10^{-7}	generally amor	
"	"	34	1.3×10^{16}	5.3×10^{-6}	amor + small regions of polycryst Ti_2O_3	
"	"	68	2.5×10^{16}	7.8×10^{-6}	increasing amount of Ti_2O_3	
"	"	170	6.4×10^{16}	3.8×10^{-5}		
"	"	340	1.3×10^{17}	9.1×10^{-5}	Surface all Ti_2O_3	2.10(c)

* amor = amorphous

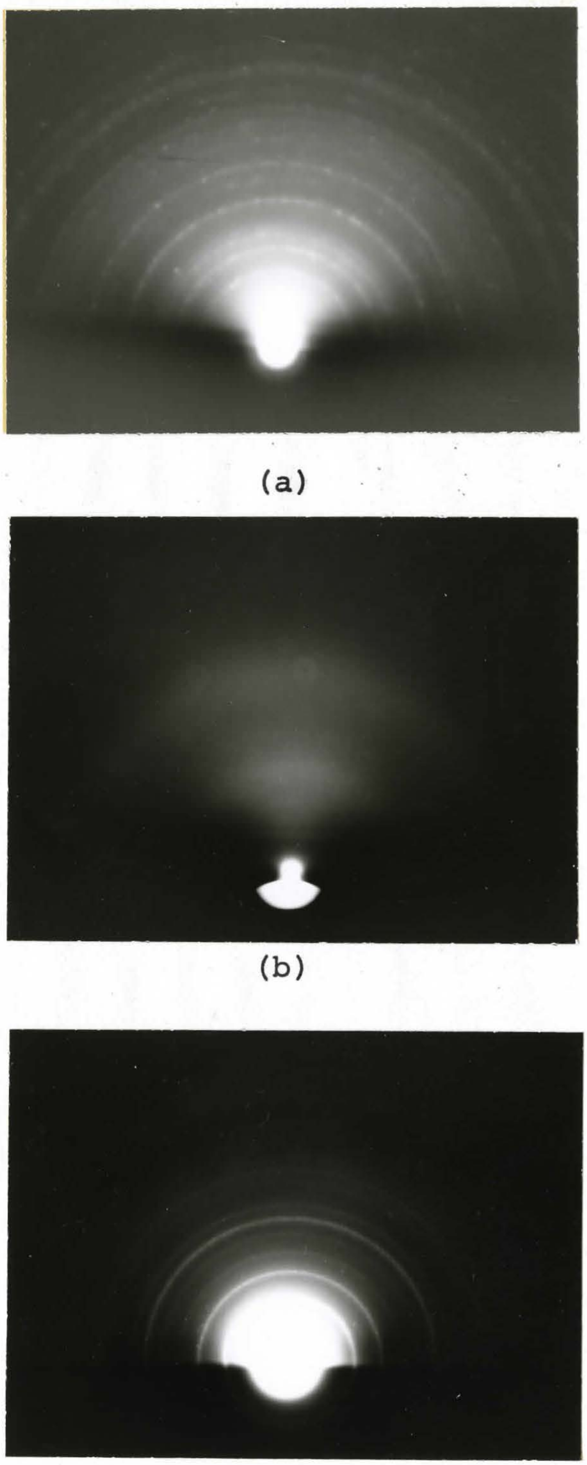

(a)

(b)

(c)

Figure 2.10 BRD patterns corresponding to the structures (a) before bombardment (TiO_2), (b) after low dose, (c) after Kr bombardment to $>10^{17}$ ions/cm^2.

After even the smallest doses (6.3×10^{14} ions/cm^2) regions of the surface have become amorphous (Figure 2.10(b)) evidenced by the characteristic halos. The fraction of the surface covered by the amorphous material increased until a dose of 6.8 μamp-min/cm^2 (2.5×10^{15} ions/cm^2) at which level the entire surface had amorphized. Low dose (6×10^{14} ions/cm^2 to 4.5×10^{15} ions/cm^2) bombardments have previously been attributed to produce amorphization of the surface region |53|, a phenomenon also exhibited by many other materials (e.g. SiO_2 , WO_3, Al_2O_3, MoO_3, V_2O_5, etc. |8,3|). Faint ring patterns were visible occasionally in conjunction with the amorphous halos. Analysis indicated the patterns to be rutile and probably were generated from the underlying crystalline TiO_2 substrate. Since the diffraction information may be considered to be that from the first few atomic layers of the specimen in BRD, it is clear that the amorphousness induced by the ion bombardment is also confined to the first few atomic layers. The amorphous layer persisted to a fluence of approximately 68 μamp-min/cm^2 (2.5×10^{16}/cm^2) at which point a few small regions of crystalline material, different from the original polycrystalline rutile were observable. Analysis of these patterns of which an example is given in Table 2-IV in comparison with the 16 Ti-O oxide members listed in Appendix I, suggested the new crystalline regions were Ti_2O_3. This fraction of the surface converted to the new phase increased with increasing ion dose until the entire surface had transformed to Ti_2O_3 (Figure 2.10(c)).

TABLE 2-IV Analysis of Kr-ion bombardment induced structure

Bombardment Structure (Figure 2.10(c))			Ti_2O_3 (X-ray data)[†]			
Ring #	I/Io * (expt'l)	d (expt'l) (Å)	d (Ti_2O_3) (Å)	I/Io	(hkl)	Error (%)
1	100	3.80	3.735	60	102	+1.7
2	62	2.71	2.710	60	014	0.0
?	(very faint)	2.52	2.580	60	110	-2.2
3	10	2.21	2.244	40	113	-1.5
			2.122	10	202	-
4	10	1.90	1.868	40	204	+1.7
5	35	1.71	1.705	100	116	+0.3
			1.639	20	212	-
6	15	1.56	1.513	40	214	+3.1
			1.490	60	300	-

[†] |44|

* microdensitometer trace

2.3.9 The correlation between colour, electrical conductivity and structural changes - The correlation between the colour, structural changes and (I/V) with dose are therefore clear. The initial bombardment causes the surface to amorphize during which the (I/V) stabilizes at a very low value near the initial value for rutile and the colour becomes slightly darker. Continued bombardment produces a net preferential loss, though perhaps not escape, of oxygen and thus (a) Ti_2O_3 regions are formed, (b) the (I/V) correspondingly increases very rapidly as the number of regions increases, and (c) the colour darkens to grey. The entire surface is finally transformed to Ti_2O_3, the (I/V) increase saturates at $1x10^{-4}ohm^{-1}$, and further the colour change to dark grey is completed. The colour change due to oxygen loss is consistent with the observations of other workers |20|, who recorded a colour change to black at even the lowest oxygen losses, as caused by thermal reduction or H_2 gas reduction. Interestingly, however most work on colour changes (i.e. colour centers) in TiO_2 has been unsuccessful, presumably due to the reliance on inadequate techniques (such as U.V. light) for disturbing the TiO_2 lattice |70|. The conductivity level of the specimens is consistent with a surface transformation to the suboxide, Ti_2O_3 in that this oxide has a high intrinsic electrical conductivity level compared to TiO_2. Table 2-V lists various values for the bulk conductivity of Ti_2O_3. Included is a value determined by the four-point probe measurement of Ti_2O_3 powder fused in a standard evaporator unit† at a pressure of 10^{-5} Torr.

---

† CVE-14, Bendix, Rochester, N.Y.

The resultant specimen was analyzed using BRD to have the Ti_2O_3 structure.

2.3.10 An estimate of the thickness W, of the conducting layer - The geometry of an irradiated specimen has been established to be two-layered; a thin conducting layer of Ti_2O_3 on an essentially non-conducting substrate. If an "average" value of the Ti_2O_3 bulk conductivity is taken from Table 2-V to be $2x10^{+1} \pm 0.5x10^{+1}$ ohm^{-1}-cm^{-1}, the thickness W of the altered layer may be estimated using the appropriate Valdes relation (Equation II-5, Appendix II) hence,

TABLE 2-V Ti_2O_3-R.T. conductivity values

σ (ohm^{-1} -cm^{-1})	Reference
$1x10^{+1}$	|21|
$1.25x10^{+1}$	|22|
$2.5x10^{+1}$	|23|
$1.2x10^{+1}$	|this thesis|

$$W(cm) = (I/V) \left(\frac{1}{\sigma}\right)_{Ti_2O_3} \left(\frac{\ln 2}{\pi}\right) \qquad (2.1)$$

where the assumption has been made that the layer W, is infinitely thin compared to the probe spacing. Therefore for 30 KeV, 6 μamp, Kr-ion bombardment of TiO_2 to a high fluence ($>10^{17}$ ions/cm^2) where (I/V) $\sim 1x10^{-4}$ ohm^{-1}, and assuming an average bulk conductivity for Ti_2O_3 of $2x10^{+1}$ ohm^{-1}-cm^{-1}, the corresponding "average" thickness is 110 Å. Further, if the error in measuring (I/V) is considered as ± 1 standard deviation and considering a spread of $\sigma(Ti_2O_3)$ literature values of $2 \times 10^{+1} \pm 0.5 \times 10^{+1}$ ohm^{-1}-cm^{-1}, then the uncertainty in the average thickness estimate of 110 Å is an "error region" as shown in Figure II.2, Appendix II extending from W = 70 to 170 Å. This estimate is significant when considering the mechanism involved in the lower oxide production |Section 8|; for example, is the effect collisional or diffusional?

2.4 The effect of altering accelerator parameters

2.4.1 Are the induced conductivity variations due to specimen heating?

- Two experimental observations prompted an examination of the response of TiO_2 pellets as a function of the ion beam current. Firstly, since low current but high dose irradiations require long time periods in the accelerator, higher currents and abbreviated exposure times were attempted, though maintaining the same total dose. However as Figure 2.9 illustrates (c.f. 6 μamp vs 13 μamp) the resultant (I/V) response was not the same. Secondly, pellets loaded onto one target and irradiated consecutively to the same dose or dose increment did not exhibit the same (I/V) values (c.f. 30 KeV, 6 μamp Kr pellets 1,2,3 - Figure 2.9). In fact the last sample to be irradiated (i.e. 1 in the 30 KeV group) had the highest saturation (I/V) and it was evident that the target support had become heated during the bombardment.

In order to evaluate, (1) the effect of ion beam heating of the target or alternatively, (2) of bombarding a target other than at R.T., two series of experiments were initiated.

2.4.2 Varying the ion beam current - TiO_2 sintered pellets were bombarded at various ion beam currents in the 0-40 μamp range adjusting the times appropriately to maintain a total fluence of 200 μamp-min/cm^2. The results (Figure 2.11) indicate three distinct regions:

I < 12 μamp - minor specimen heating in the ion beam.
II > 12 and < 20 μamp - a transitory region.
III > 20 μamp - severe specimen heating causing an enhanced value of (I/V).

Clearly to generate reproducible results, all irradiations should be for example consistently in the low current region to avoid spurious heating effects.

2.4.3 Varying the target temperature - Recalling that pellets on one target support exhibited graduated (I/V) response, that is the (I/V) increased from the first bombarded to the last, it would be expected that a pellet at high temperature would have a higher induced (I/V) than a pellet at low temperature at the same dose level. Separate high and low temperature stages |refer to Appendix III| were used to investigate the induced (I/V) as a function of target temperature keeping all other experimental parameters (current, accelerating voltage, time) constant with the results given in Figure 2.12. Between -125°C and 200°C there is effectively an exponential increase in (I/V) with temperature, yet at the highest temperature (380°C) a seemingly unexpected decrease appeared. This was later explained as due to concurrent annealing as damage was introduced. Here probably lies the

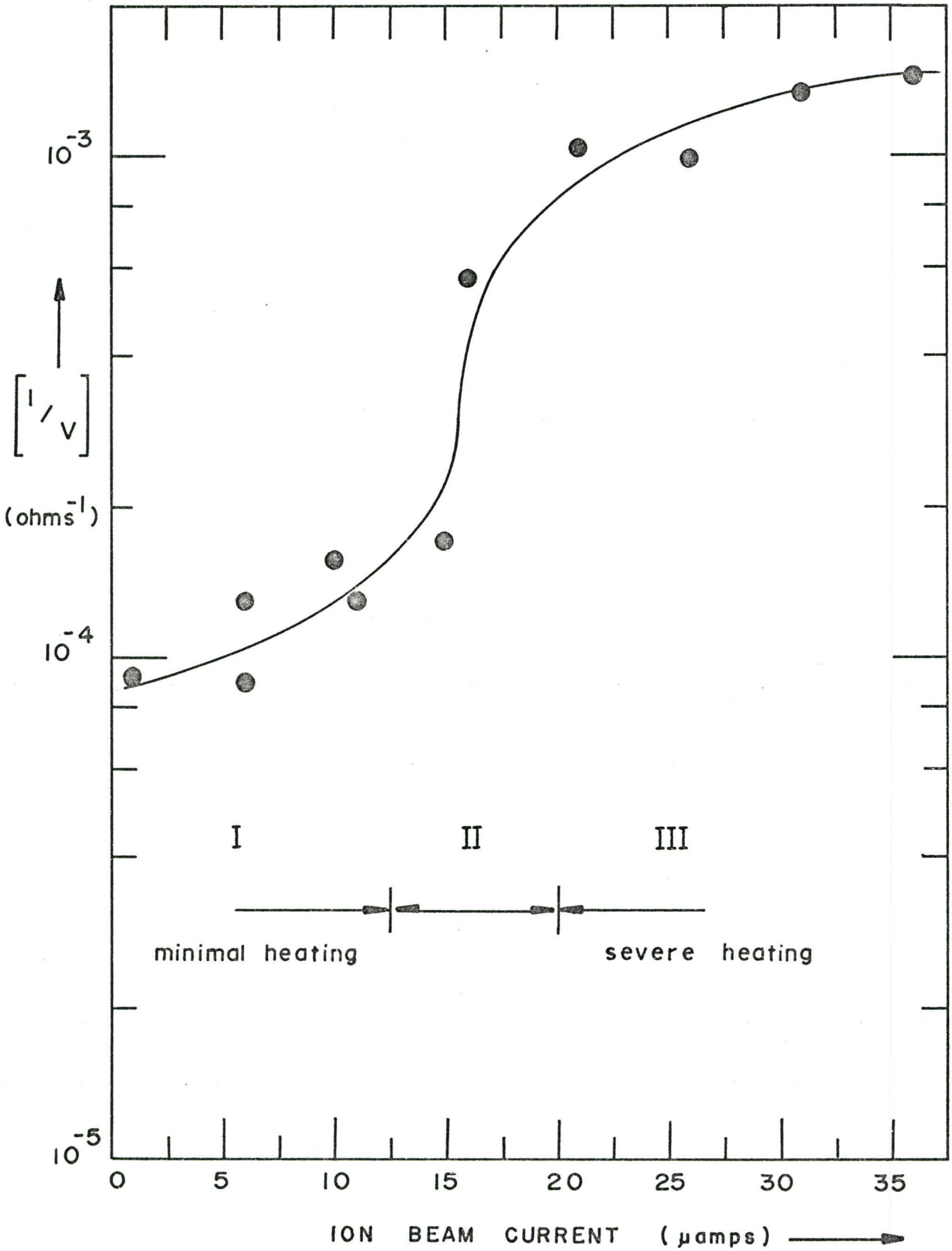

Figure 2.11 Induced conductivity (I/V) as a function of Kr ion beam current I, maintaining a total dose (fluence) of 200 μamp/min cm^2 using 30 KeV, Kr ions.

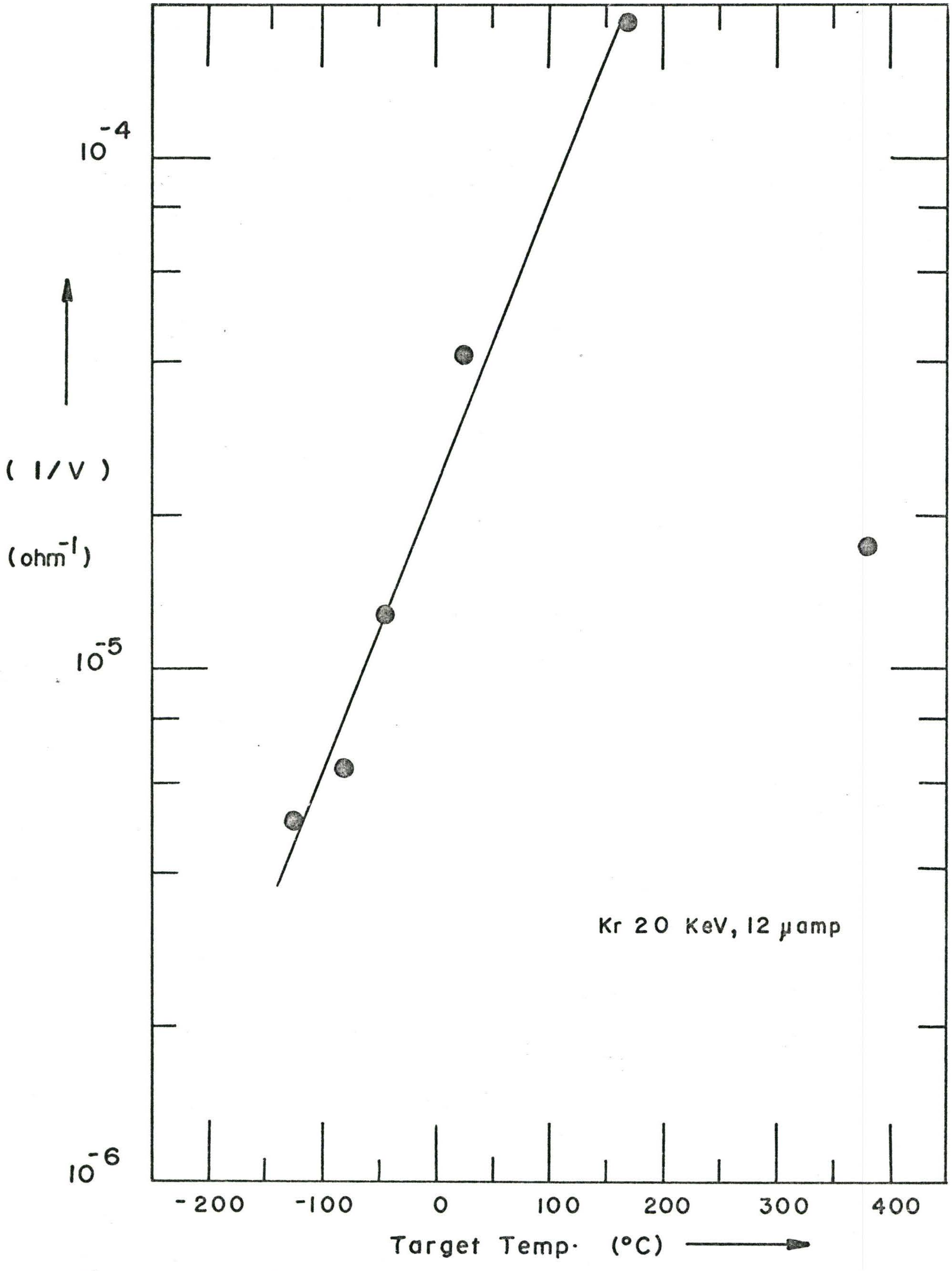

Figure 2.12 Induced conductivity (I/V) as a function of target temperature (T) in an energetic beam of 20 KeV, 12 μ amp, Kr to a total dose of 200 μamp-min/cm^2.

explanation of the variation of induced (I/V) versus dose of specimens 1, 2 and 3 in Figure 2.9. During the incremental dose given specimen 3, the target support gradually heated, hence the incremental dose given 2 was not at R.T. but at an elevated temperature. Specimen 1 was at a still higher temperature. Hence if the pellets were bombarded separately within experimental error the (I/V) curves would be the same.

2.4.4 Bombarding with oxygen ions - Substituting 30 KeV oxygen ions instead of Kr had a dramatic effect on the induced (I/V) with increasing dose (Figure 2.13). At saturation the (I/V) due to oxygen is only $3\text{x}10^{-6}$ - in fact negligible compared to the response to 30 KeV Kr ions. Intuitively, this might have been expected. Since inert gas (Kr) bombardment produced a net oxygen loss from the lattice, bombarding with oxygen, although producing the same effect (an (I/V) increase) could reintroduce more oxygen hence minimize the overall oxygen loss. The discussion of the mechanisms involved in the interpretation of these results appears in Section 8.

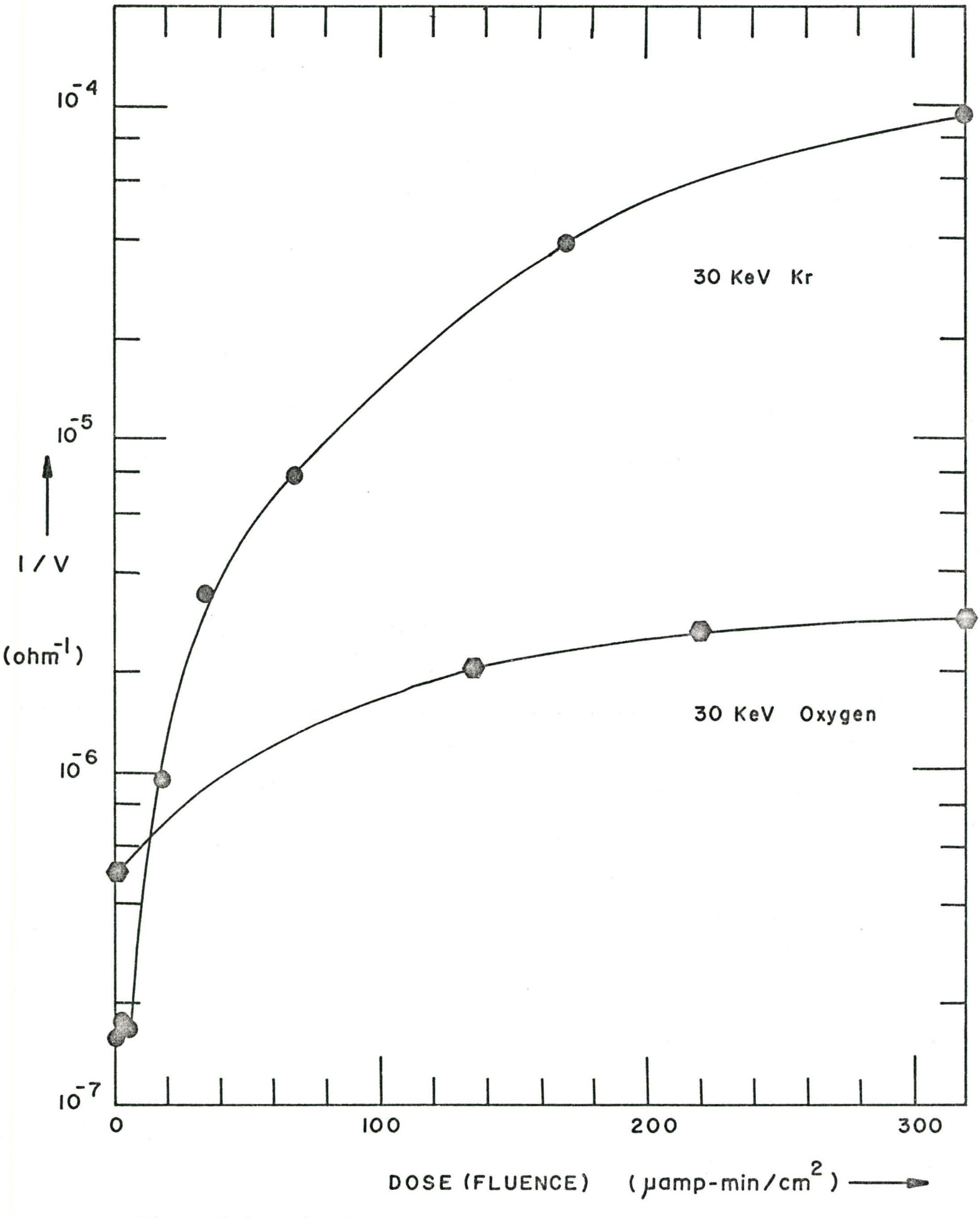

Figure 2.13 (I/V) response in a 30 KeV oxygen beam

SECTION 3

Annealing of the Altered Layer on the Sintered Pellets and Gas Release Experiments

3.1 Preliminary annealing in air

A pellet of TiO_2 bombarded with a 40 KeV, 20 μamp, Kr-ion beam to a dose in the saturation region was annealed isochronally by heating in increments of 50°C for 10 minutes in air. After each increment the electrical conductivity was monitored by the four-point probe technique. This annealing behaviour is shown in Figure 3.1 and exhibited the following characteristics:

(i) - below 200°C no annealing took place hence the induced structure was stable to this temperature.

(ii) - above 250°C the induced conductivity rapidly decreased so that by 500°C the (I/V) had almost returned to the initial conductivity of TiO_2 ($\sim 10^{-7}$ ohm^{-1}). There is no inconsistency then, in recording a lower than expected (I/V) when the target temperature exceeds 250°C (Figure 2.12) and the (I/V) response to target temperature may be rationalized as consisting during bombardment above 250°C of two competitive processes: a radiation damage mechanism to produce Ti_2O_3 and annealing of the induced damage.

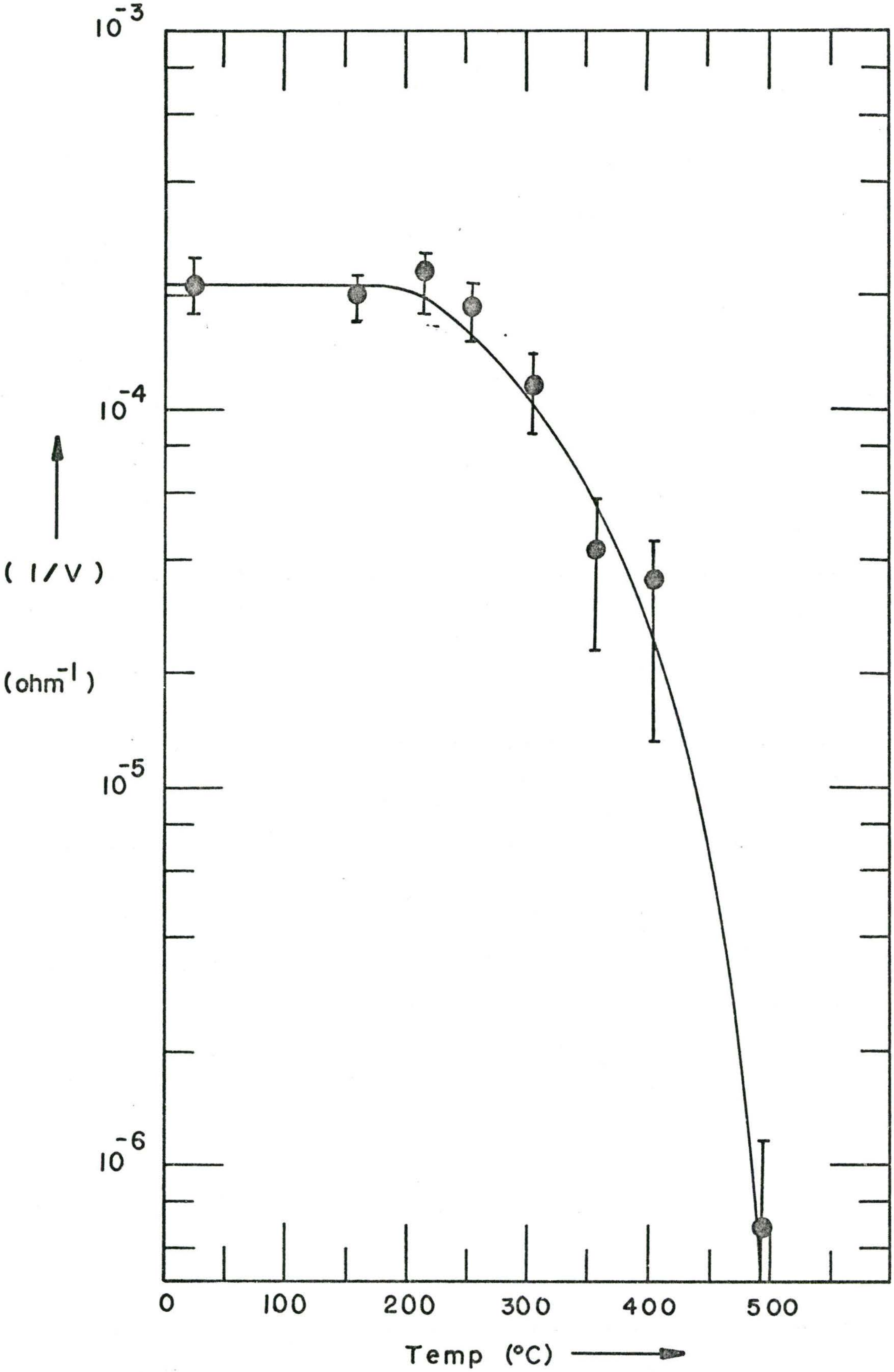

Figure 3.1 Isochronal annealing (10 min. steps) of the induced conductivity of TiO_2 bombarded with Kr ions to $>10^{17}$ ions/cm^2.

3.2 Gas release experiments

3.2.1 General comments

In order to more fully investigate the annealing of the Ti_2O_3 layer, gas release experiments similar to |53| were carried out as described in Appendix IV. Briefly, specimens of TiO_2 were bombarded with inactive Kr to a dose commensurate with complete surface transformation to Ti_2O_3. Subsequently, a tracer dose or "label" of radioactive ${}_{36}Kr^{85}$ was introduced and the release of this gas was monitored by a G.M. counter. Annealing was affected at a furnace-programmed rate of 25C°/min in a regulated flow of an inert gas (He).

3.2.2 Experimental results

Figure 3.2 contains the results as the rate of gas release, fractional activity remaining, and fractional conductivity remaining with respect to temperature. Two distinct peaks at 610°C and 880°C respectively* are evident in the rate of gas release spectrum. An interesting feature of the (I/V) annealing is that the results in He were almost identical to the isochronal annealing results in air (Figure 3.1). Since the (I/V) annealing of the altered layer (R.T. to 500°C) is independent of the atmosphere, this suggests that the annealing mechanism is an internal

---

* Similar double-maxima spectra for Kr^{85} release from TiO_2 were previously recorded |53|, however the doses involved were an order of magnitude less than in this investigation.

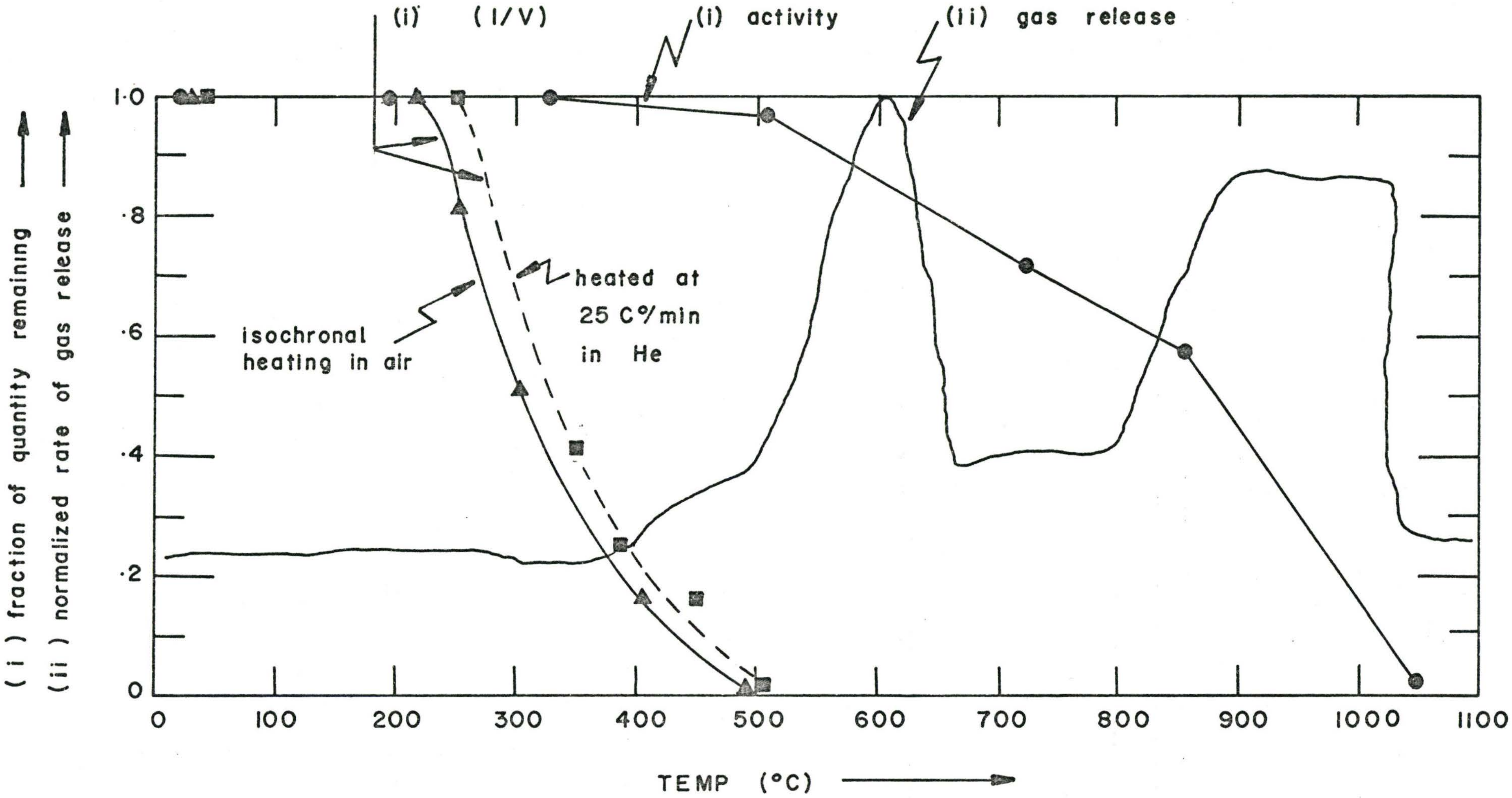

Figure 3.2 Gas release annealing of the Ti_2O_3 altered layer on TiO_2 pellets in terms of the rate of radioactive label release, fractional activity and conductivity remaining.

"reshuffling" and does not, for example, involve an inward diffusion of oxygen from the pellet environment. Further, this would suggest also that oxygen is lost during bombardment by a collisional mechanism such that Kr ions enter the solid and displace oxygen from the lattice sites. The lattice has effectively decreased its stoichiometry, (i.e. perhaps by a shear mechanism) and the oxygen could precipitate internally and could be reintroduced later into the lattice by specimen heating. Since it is generally accepted that one may associate gas release peaks with gross structural changes |54| in many oxide systems, specimens straddling the maxima at 610°C and 880°C were investigated using the BRD technique with the following results:

3.2.3 Distinct annealing regions and structures

R.T. to 200°C	No structural or (I/V) changes .
200 to 500°C	The surface amorphized and the conductivity rapidly decreased to less than 10% of its original value, but at the same time there was an almost negligible activity loss.
500 to 650°C	The gas release rate maximized at 610°C indicating some concurrent structural change. Although, up to this peak the amorphous structure dominated, there was by 550°C (Figure 3.3) a visible ordering as evidenced by the fine ring marked with an arrow.

650 to 800°C	Gas release stabilized at a rather high level above the background activity. The clearly crystalline nature of the surface (Figure 3.4) at 775°C suggests that the peak at 610°C corresponds to an amorphous to crystalline transition. Analysis of Figure 3.4, shown in Table 3-I indicated the presence of Ti_4O_7, whence a net gain in oxygen content.
800 to 1000°C	At 905°C near the start of the second maximum, the surface structure was not sharply crystalline but suggested the occurrence of some transition (Figure 3.5).
>1000°C	The rate of gas release decreased to a low level, almost all the "label" having been released. The diffraction pattern at 1110°C (Figure 3.6) exhibits a well defined crystal structure that appeared to be a higher oxide of the Ti_nO_{2n-1} homologous series, perhaps Ti_5O_9 or Ti_6O_{11}.

Figure 3.3 BRD pattern of Ti_2O_3 altered layer annealed to 555°C.

Figure 3.4 BRD pattern of Ti_2O_3 altered layer annealed to 775°C.

TABLE 3-I

Analysis of BRD pattern of Figure 3.4

Diffraction pattern		Ti_4O_7†	
I/I_o (expt'l)	d(expt'l) Å	d (accepted) Å	I/I_o
100	5.50	5.267	40
30	4.38	4.278	80
10	3.76	3.772	40
100 (doublet?)	3.41	3.384 3.353	100 70
80	2.86	2.912 2.819	60 100
80	2.68	2.633	80
80	2.50	2.526 2.479	80 80
80	2.41	2.425	80

† |44,45,46|

Figure 3.5 BRD pattern of Ti_2O_3 altered layer annealed to 905°C.

Figure 3.6 BRD pattern of Ti_2O_3 altered layer annealed to 1110°C.

3.3 Structural evolution and conclusions

The following overall structural scheme is apparent from the bombardment and annealing diffraction information:

Bombardment:

$$\mathrm{TiO_2(rutile)} \rightarrow \mathrm{TiO_2(amorphous)} \rightarrow \mathrm{TiO_x(amorphous)} \rightarrow \mathrm{Ti_2O_3(crystalline)}$$

Annealing (in He):

$$\mathrm{Ti_2O_3(crystalline)} \rightarrow \mathrm{TiO_x(amorphous)} \rightarrow \underset{610^{\circ}\mathrm{C}}{\mathrm{Ti_4O_7(crystalline)}} \rightarrow \underset{1110^{\circ}\mathrm{C}}{\mathrm{Ti_nO_{2n-1}(crystalline)}}$$

During the annealing sequence, $\mathrm{TiO_x}$(amorphous) must have at some point the $\mathrm{Ti_3O_5}$ stoichiometry. $\mathrm{Ti_3O_5}$ is of particular technological interest because the semiconductor to metallic transition that occurs at 175°C is of sufficient magnitude (a factor of 14 to 15, |24|) that $\mathrm{Ti_3O_5}$ is a potential material for thermal devices, temperature controllers, etc. |25|. The controlled annealing of bombardment induced surface transformation of $\mathrm{TiO_2}$ to $\mathrm{Ti_2O_3}$, suggests a rather novel technique for producing this and other intermediate oxides in thin-film form.

SECTION 4

Bombardment Induced Changes in Single Crystal Rutile in an Energetic Beam of Kr ions

4.1 General

Induced conductivity has been adequately illustrated in the case of TiO_2 sintered pellets. However, since V_2O_5 and MoO_3 |8| which exhibited similar behaviour, were also sinters it was deemed necessary to verify that the effect was not just a result of the state of aggregation of the oxide. Consequently, rutile single crystals were subjected to Kr-ion irradiations.

4.2 Bombarding perpendicular to the prepared surface

4.2.1 Experimental - A rutile single crystal was bombarded incrementally with a 40 KeV, 10 μamp beam of Kr at R.T. along a path almost perpendicular to the prepared surface up to doses commensurate with surface transformation to Ti_2O_3 for pellets.

4.2.2 Results and discussion - The expected (I/V) increase did not in fact occur and after an initially rapid increase, the (I/V) went through a maximum then returned to a constant value of approximately 3×10^{-6} ohm^{-1} (Figure 4.1 - curve (A)) as compared to 1×10^{-4} for pellets exposed to the same high levels. Considering that the process of $TiO_2 \xrightarrow{Kr} Ti_2O_3$

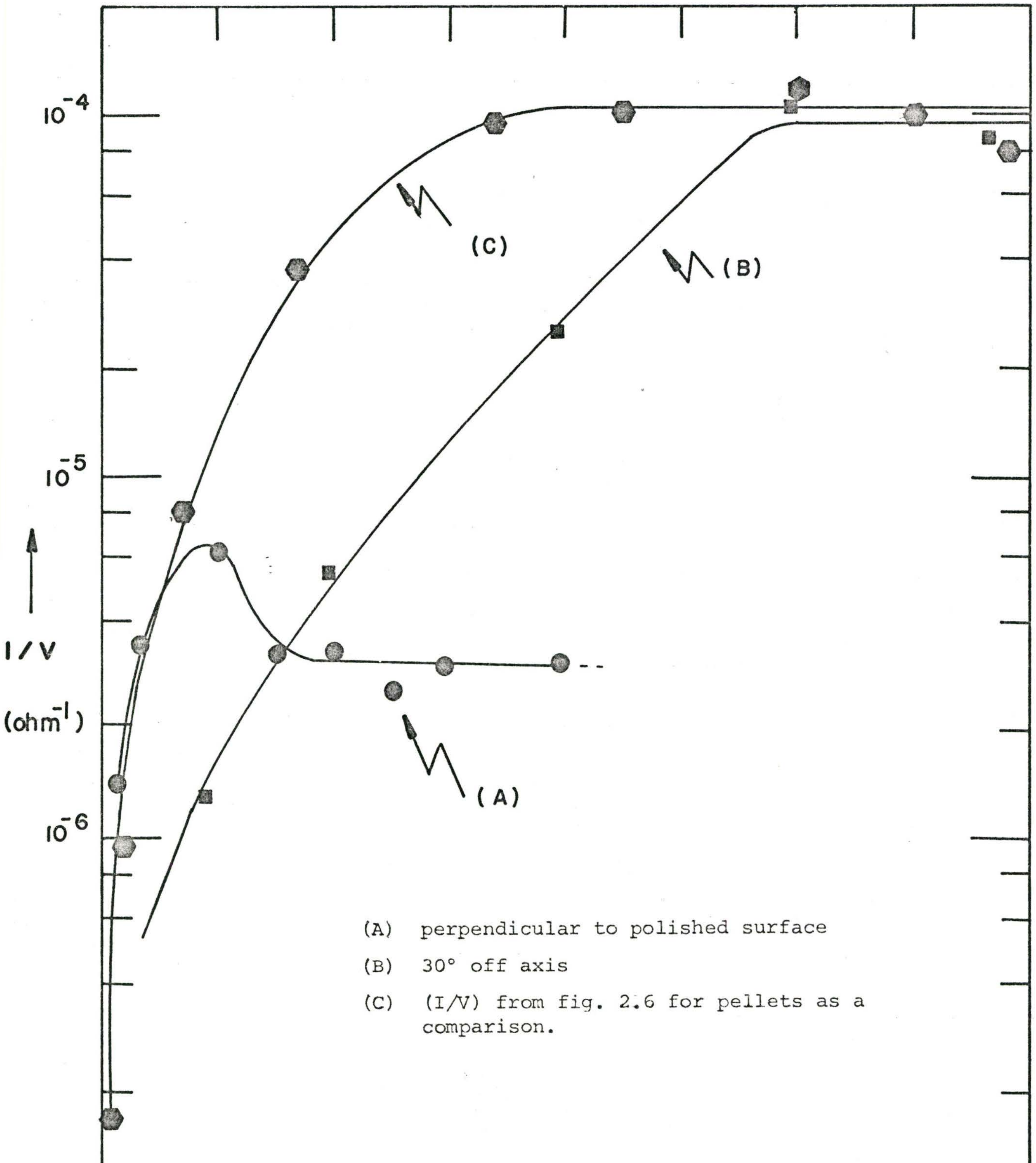

(A) perpendicular to polished surface

(B) 30° off axis

(C) (I/V) from fig. 2.6 for pellets as a comparison.

Figure 4.1 (I/V) response of single crystal rutile to Kr ion bombardment.

necessarily involves either the preferential sputtering of oxygen from the surface to produce vacancies that diffuse inward or the preferential "lattice knock-off" of oxygen internally, if a significant portion of the ion beam is channeled (which is highly probable near a low index direction in the single crystal), the electronic stopping component $\frac{dE}{dx}_{e}$ of the total stopping power $\frac{dE}{dx}_{T}$ would predominate. As a result the normal nuclear stopping component $\frac{dE}{dx}_{\eta}$ required for lattice ejection of oxygen would not occur. In a random target such as the finely polycrystalline TiO_2 sinters $\frac{dE}{dx}_{\eta}$ is a main contributor to $\frac{dE}{dx}_{T}$ at these low accelerating voltages |29|. Equally significant is the decrease in surface sputtering yield when bombarding along a low index direction |72|.

4.3 Crystal orientation

The orientation of a single crystal specimen was determined using the back-reflection X-ray diffraction Laue technique as described in Appendix V. Poles of zones were identified by comparing the interplanar angles measured from a stereographic projection of the Laue spot pattern, with those generated from a computer program based on the data for tetragonal TiO_2 (rutile). Analysis revealed that bombardment perpendicular to the prepared surface was along the normal to the low index {100} plane. A high degree of channeling is therefore a reasonable result, since sighting along the <100> in a rutile single crystal reveals a rather "open" network.

4.4 Off-axis bombardment

4.4.1 General - A rutile single crystal was bombarded with 30 KeV, 6 μamp, Kr arbitrarily at 30° from the prepared surface normal, in order to decrease the effect of channeling. In the case of ion-implanted indium in single crystal Si at R.T. |26|, an 8° shift from the <111> axis reduced the channeling so effectively that the range of the Indium ions could be predicted to an excellent first approximation using a simple Gaussian distribution having a mean projected range and standard deviation calculated by Johnson and Gibbons |27|. These range values are calculated based on the integral equations of the L.S.S. theory of stopping in a random target (refer to Section 5).

4.4.2 Results - Figure 4.1-(B) illustrates the single crystal (I/V) response to off-axis bombardment, and now exhibits the same features as the oxide sinter counterpart, although these have been shifted to higher doses:

Region I - (<50 μamp-min/cm^2) - an incubation period in which the (I/V) is small and not well defined.

Region II - (100 μamp-min/cm^2 < dose < 600 μamp-min/cm^2) - a rapid increase in (I/V) with increasing ion fluence.

Region III - (>600 μamp-min/cm^2) - (I/V) has saturated and remains constant at a value of 1×10^{-4} ohm^{-1}, the same as that for pellets, and the single crystal surface had a greyish tint.

BRD investigation revealed the structural changes which occurred during bombardment. The starting single crystal surface exhibited the expected well defined and readily analysable spot pattern (Figure 4.2 (a),(b)), characteristic of tetragonal rutile. At the saturation (I/V) level a decidedly polycrystalline surface structure had developed (600 μamp-min/cm^2 - Figure 4.3) and in the spirit of the pellet specimens probably has a stoichiometry less than TiO_2 although the pattern was not analysable.

4.5 Annealing of the damage layer

An attempt at "sharpening" the diffraction pattern was made. The damaged crystal was annealed in vacuum (1×10^{-6} mm Hg) to avoid oxygen pickup to 750°C and held at temperature for 15 minutes with the unexpected result that the damage annealed almost totally and the spot pattern, Figure 4.4 was that of the starting rutile crystal (Figure 4.2). The observation of a spot pattern suggests that annealing proceeded toward the surface, such that the reintroduction of oxygen into the lattice was effected by oxygen already precipitated therein (this could be caused mainly by a collisional process rather than surface sputtering). Otherwise, if residual oxygen in the vacuum diffused inward, one would have expected polycrystalline TiO_2 on the surface. This notion of an internally precipitated oxygen source is consistent with the previous results (Section 3.2.2) that indicated the equivalence of heating pellets in air or He.

(a) (b)

Figure 4.2 (a) Surface structure (BRD) of single crystal rutile prepared surface
(b) Indexed spot pattern of (a).

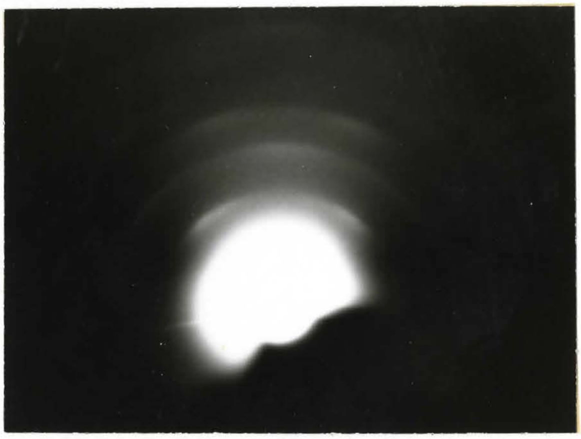

Figure 4.3 Rutile single crystal surface structure after 2.2 x 10^{17} ions/cm^2 of Kr.

Figure 4.4 Post bombardment vacuum annealed single crystal rutile surface structure .

SECTION 5

Kr-ion Distribution in TiO_2

5.1 Depth distribution of ions

5.1.1 General

Experimentally, the bombardment of TiO_2 with Kr has been shown to drastically alter the surface stoichiometry, an alteration which is necessarily intimately related to the response of the target to energetic Kr ions. In particular, an energetic ion injected into a material will undergo collisions or interactions with both the nuclei and electrons of that target. In so doing, the ion loses its energy and eventually comes to rest at some position characteristic of the ion, its energy, and the target material. However since the energy loss events occur randomly in a random target, the ion rest position is not the same for each monoenergetic ion but may be represented by a distribution in terms of $<R_p>$ the ion mean range projected along an axis parallel to the incident beam, and $<\Delta R_p>$ a similarly projected mean standard deviation. Figure 5.1(a) shows R, the total range of an ion and R_p its projection along the incident beam direction while Figure 5.1(b) indicates the projected range distribution of all such ions.

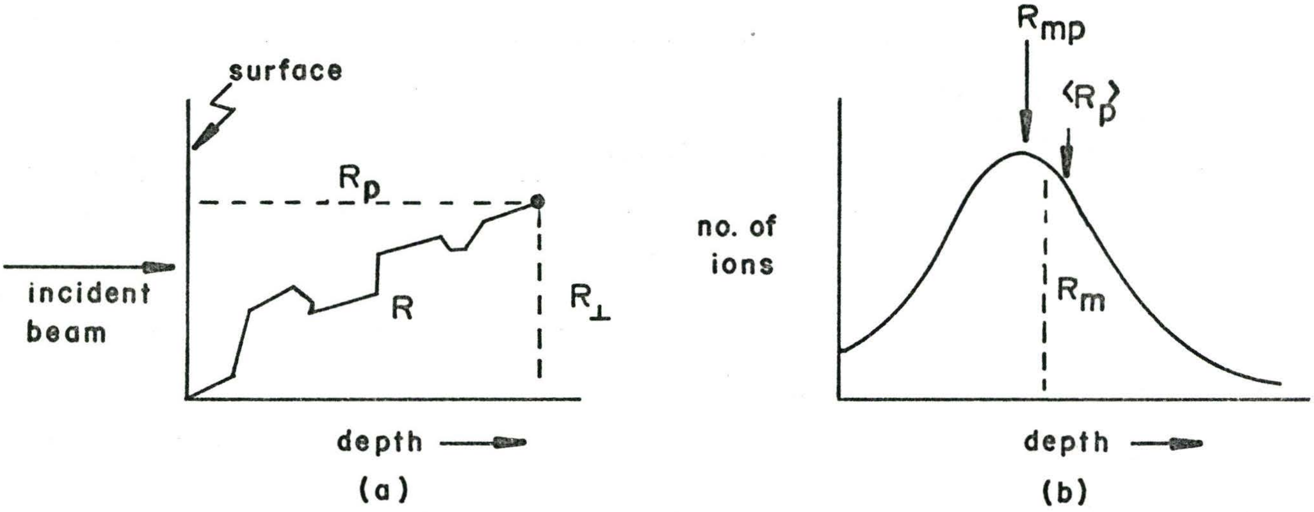

Figure 5.1 (a) Definition of an ion range in terms of R_p, the projected range;

(b) An ion range distribution characterized by R_{mp} (the most probable range), $<R_p>$ (the mean projected range), and R_m (the median range).

The latter may be characterized by R_{mp} the most probable range, R_m the median range (at which one half of all the ions have been stopped), and $\langle R_p \rangle$ the mean projected range. For an exact normal Gaussian distribution R_{mp}, R_m and $\langle R_p \rangle$ would coincide however experimentally the ion distribution is skewed and these quantities are not the same.

For a crystalline target, these same interactions or collisional processes occur but with an additional feature. If a low index crystallographic direction or plane lies close to the incident beam direction, an inordinate portion of the beam will penetrate to great depths, that is, "channeling" occurs |40|. Ions that have been channeled lose their energy by a series of low energy loss "steering" interactions averaged over many atoms in the channel wall. While violent termination of this channeling may occur, the mechanism is not well known and numerical solution of the ion distribution is not yet possible if channeling is considered. However, off-axis bombardment |26| or exclusive use of finely polycrystalline or amorphous targets ensures a great suppression of the channeled portion of the energetic beam, and the range distributions are then well described by the amorphous stopping theory of Lindhard, Scharff and Schiøtt (L.S.S.) |29|.

5.1.2 Energy loss mechanisms - Two mechanisms account for the energy loss from an ion of energy less than 1 MeV namely nuclear stopping and electronic stopping. Nuclear stopping $\frac{dE}{dx}_{\eta}$, involves the elastic collisions of the ions and target nuclei and produces most of the angular scattering. Nuclear stopping in fact dominates at low ion energies. Electronic stopping $\frac{dE}{dx}_e$, involves the energy loss in the inelastic (ion/target-electron) interactions and represents most of the energy loss, for example in a channeled beam. This is also the dominant process at very high ion energies. Therefore the total stopping power, $\frac{dE}{dx}_T$ is given by:

$$\frac{dE}{dx}_T = \frac{dE}{dx}_\eta + \frac{dE}{dx}_e \qquad (5\text{-}1)$$

and <R> the total range of the ion in the material is defined by:

$$\langle R \rangle = \int_o^E \frac{dE}{-\frac{dE}{dx}_\eta - \frac{dE}{dx}_e} \qquad (5\text{-}2)$$

The quantity of interest experimentally is the depth of penetration of the ion below the target surface (i.e. $\langle R_p \rangle$), and the projected range theory of L.S.S. provides the basis for the numerical calculation, by defining the probability density functions, $p(R_p,E)$ and $q(R_\perp,E)$ for a particle ending up in a given differential element of volume, from which an integral range equation may be derived. A more detailed description of the L.S.S. theory will not be given here as other authors |73,74,52,27| have already provided adequate summaries.

5.2 Application of the L.S.S. Range Theory to the case of Kr bombarded TiO_2 to generate ion profiles

5.2.1 Mean projected range ($<R_p>$) values

Mean projected ranges, $<R_p>$ and projected standard deviations, $<\Delta R_p>$ have been tabulated |27| for many combinations of impinging ions and target substrates, utilizing the L.S.S. projected range theory. Though the combination Kr on TiO_2 does not occur in the tabulation, nevertheless, since ranges in a compound are approximated by those for an element of the same atomic number except for a scaling factor due to the different atomic densities |27,29| range values for TiO_2 may be estimated.

The error in representing a binary target as a unary target should not be too great when, as with TiO_2 the atomic weights are not too dissimilar. Figure 5.2 and Figure 5.3 include all the Kr range data of Johnson and Gibbons plus additional data |75| at 10, 20, 30 and 40 KeV in terms of $<R_p>$ in $\mu g/cm^2$ as a function of the target charge ($\bar{Z}_2$) and mean atomic mass ($\bar{M}_2$) respectively. Over the range of targets and energies, a marked <u>linear</u> dependence of $<R_p>$ versus $\bar{Z}_2$ and $\bar{M}_2$ is illustrated. Serious deviation occurs only where the elements of the binary target are widely separated in the periodic table (i.e. the mean mass or charge approach is no longer valid: e.g. WO_3, Nb_2O_5, Ta_2O_5). Since for TiO_2 ($\bar{M}_2 = 26.6$; $\bar{Z}_2 = 12.6$) Ti and O are reasonably close, one would expect an interpolation of the data to yield acceptable $<R_p>$ values.

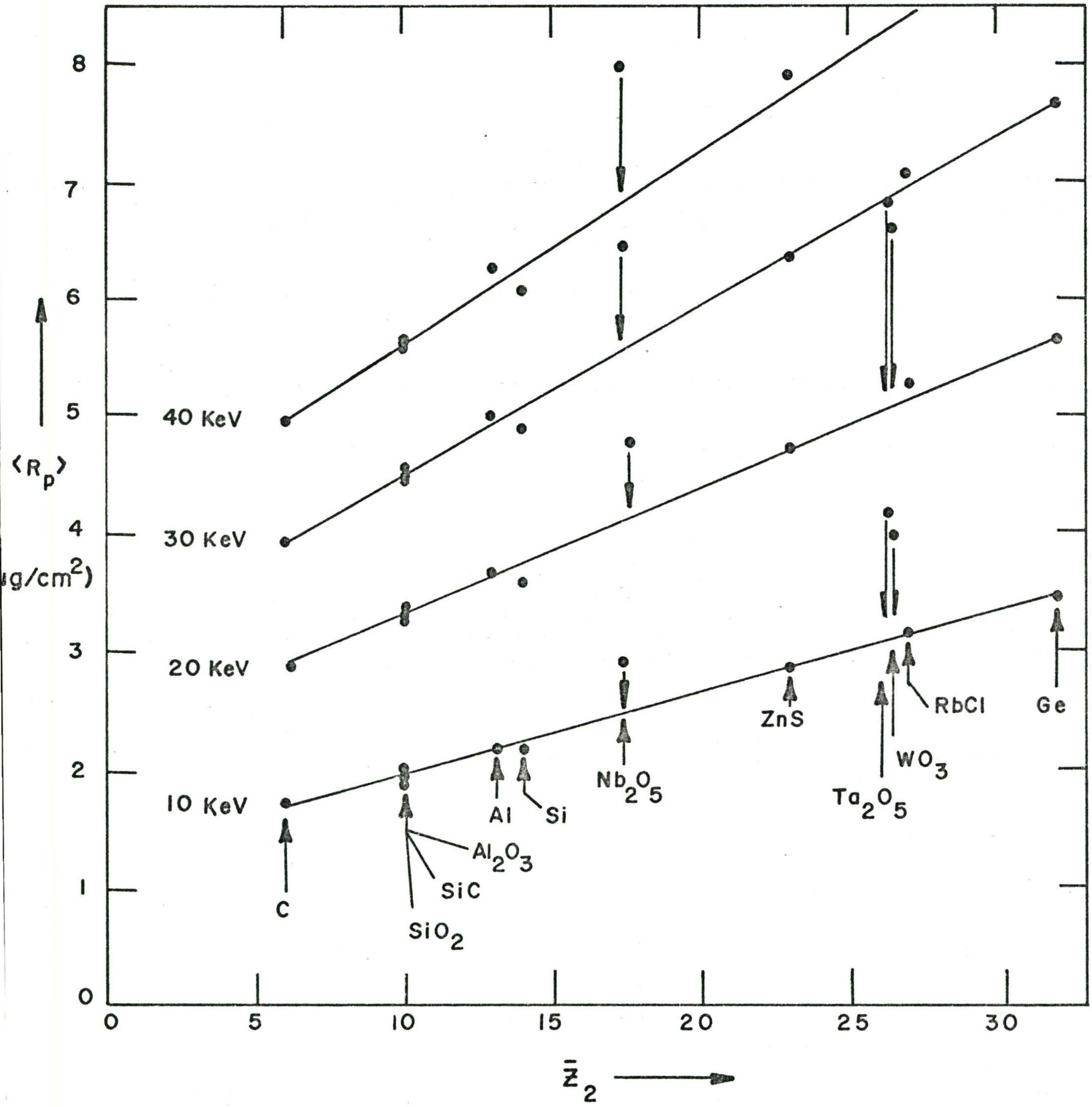

Figure 5.2 Mean projected ranges ($\langle R_p \rangle$)of Kr ions in various targets in units of $\mu g/cm^2$ as a function of the mean atomic number ($\bar{Z}_2$) of the target.

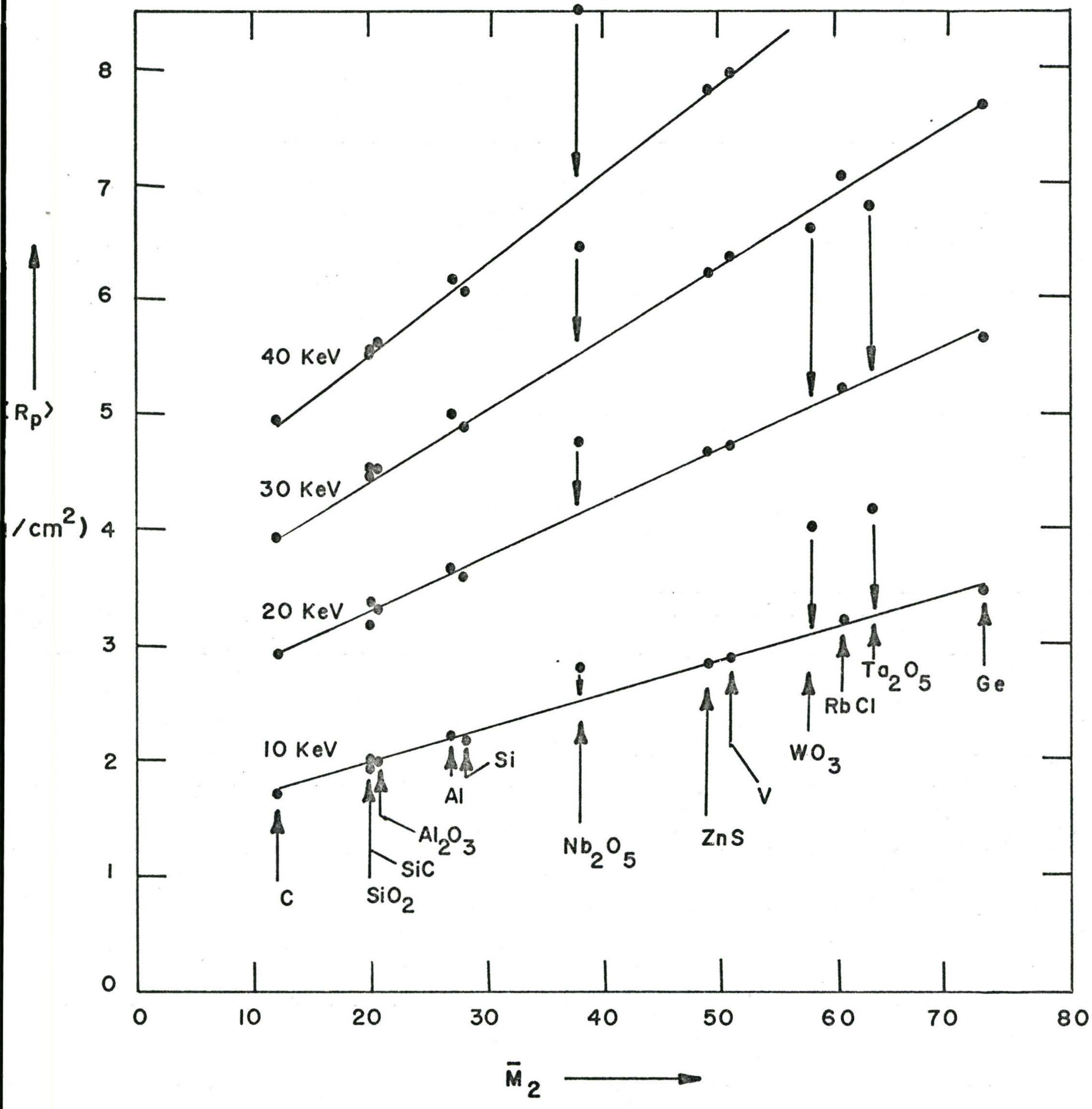

Figure 5.3 Mean projected ranges ($<R_p>$) of Kr ions in μg/cm^2 as a function of mean mass ($\bar{M}_2$) of the target material.

Table 5-I contains a summary of these interpolations, including standard deviations $\langle \Delta R_p \rangle$ based on an atomic density scaling of $\langle \Delta R_p \rangle$ data for Al ($M = 27$, $Z = 13$) [27].

TABLE 5-I TiO_2 - Kr ion Range Values

E_1 (KeV)	$\langle R_p \rangle$ ($\mu g/cm^2$)	$\langle R_p \rangle$ (Å)	$\langle \Delta R_p \rangle$ (Å)
10	2.10	79	18
20	3.55	84	30
30	4.80	113	41
40	6.05	142	50

Since the surface TiO_2 transformed to Ti_2O_3 at high Kr doses, the effect on the Kr ion range had to be considered. Figure 5.4 contains $\langle R_p \rangle$ versus Kr ion energy for TiO_2 and Ti_2O_3. Since there is only a slight reduction in $\langle R_p \rangle$ for the target material, there would be no significant variation in the Kr ion range during the bombardment, even though the target first amorphizes (hence $\langle R_p \rangle$ of L.S.S. strictly applies) and then forms fine polycrystalline Ti_2O_3 on the surface.

5.2.2 Integral ion-concentration profiles.

When measuring bombardment ion concentration invariably the experimental quantity measured is the integral concentration remaining in the specimen, as for example given by the sectioning of a target bombarded with radioactive $_{36}Kr^{85}$.

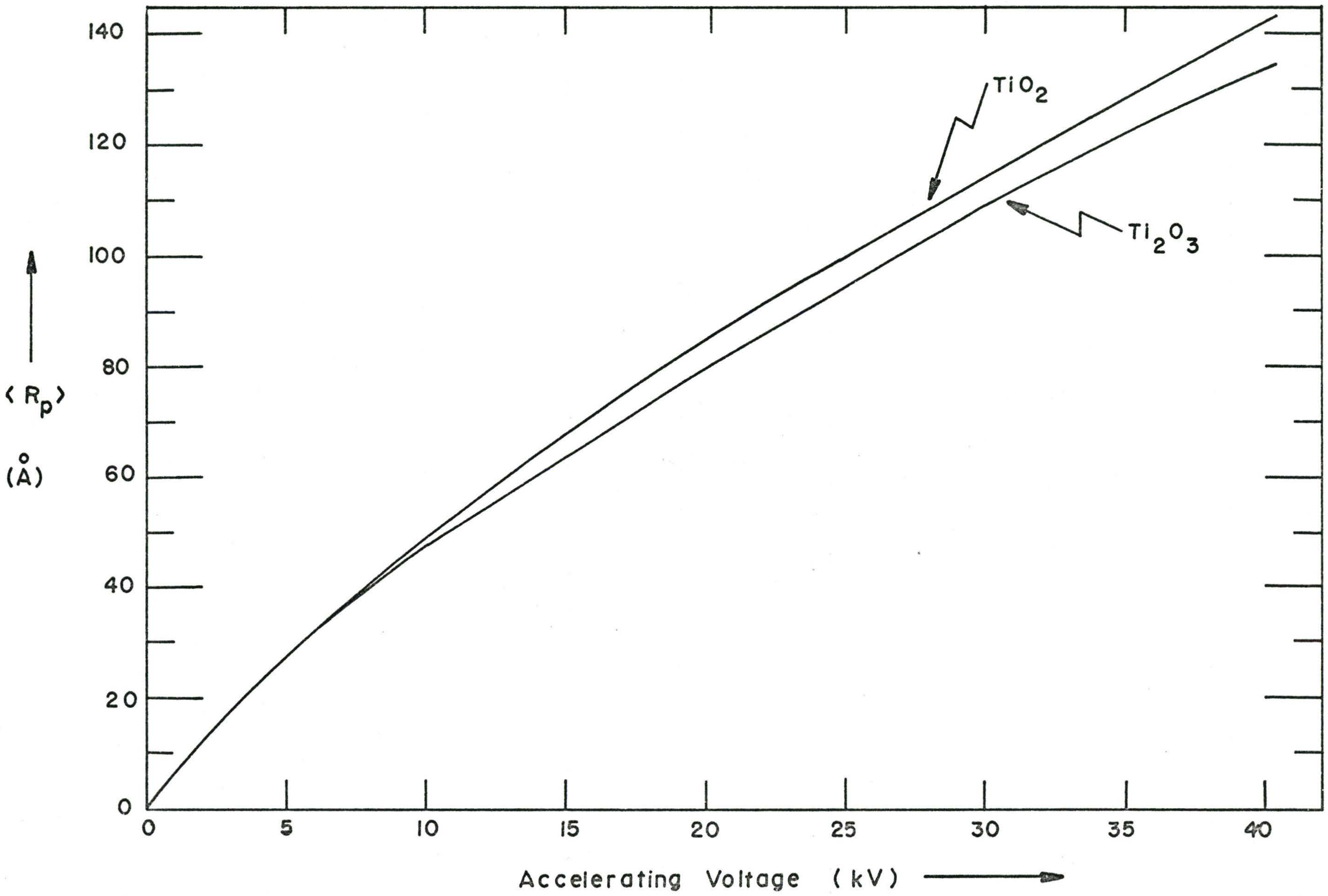

Figure 5.4 Mean projected range of Kr ions in TiO_2 and Ti_2O_3 as a function of the accelerating voltage (V).

Assuming a random target and no surface sputtering, the differential ion concentration profile ($F(x)$) will be similar to the normal Gaussian distribution, though will be given more exactly by Edgeworth's Expansion in terms of spatial moments:

$$F(x)dx = dx(2\pi\mu_2)^{-\frac{1}{2}} \exp(-\xi^2/2)\; f(\xi) \qquad (5.3)$$

where

$$f(\xi) \simeq 1 - (\tfrac{1}{6})(\mu_3/\mu_2^{3/2})(3\xi - \xi^3) + \tfrac{1}{24}(\mu_4/\mu_2^{2} - 3)$$

$$(3-6\xi^2 + \xi^4) - \ldots$$

and $\mu_n = \langle\Delta x^n\rangle = \langle(x - \langle x\rangle)^n\rangle$ = spatial (central) moments (5.4)

and $\xi = (x - \langle x\rangle)/\mu_2^{\frac{1}{2}}$ (5.5)

Taking only the first term yields the simple Gaussian distribution of width $\mu_2^{\frac{1}{2}}$ (i.e. $\langle\Delta R_p\rangle$) centred around the mean $\langle x\rangle$ (i.e. $\langle R_p\rangle$). Therefore at any point x from the surface of the target, the deposited ion differential concentration will be (where $\mu_2^{\frac{1}{2}} = \mu$ = standard deviation):

$$C_{diff}(x)\; dx = \frac{dx}{\sqrt{2\pi}\mu} \exp\left[-\left(\frac{x - \langle x\rangle}{\sqrt{2}\mu}\right)^2\right] \qquad (5.6)$$

Likewise, the integral concentration at any point, x, the quantity usually measured in a dissolution or sectioning experiment, is found by integrating Equation 5.6 from x → ∞:

$$C^{\text{integral}}(x) \approx \frac{1}{\sqrt{\pi}} \int_{\frac{x-\langle x\rangle}{\sqrt{2}\mu}}^{\infty} e^{-t^2} dt \tag{5.7}$$

which is the well known "error function", i.e.

$$C^{\text{integral}}(x) \approx \tfrac{1}{2}\text{erfc}\left[\frac{x-\langle x\rangle}{\sqrt{2}\mu}\right] \tag{5.8}$$

Evaluating the argument from the range data (Section 5.2.1) and the erfc function from tables |28|, integral concentration profiles were determined for 10, 20, 30 and 40 KeV Kr in TiO_2 (Figure 5.5). These profiles represent therefore the integral concentration of Kr left at a specific depth in the specimen assuming a random target where the dose level is sufficiently low that no significant surface sputtering has occurred.

5.2.3 The effect of surface sputtering

During irradiation, while the surface transformation to Ti_2O_3 is occurring, surface sputtering (surface atom ejection) also occurs. Since the dose to (I/V) saturation exceeds 10^{17} ions/cm^2 it is expected that a considerable depth will have been sputtered (c.f. anodic TiO_2 |30|), a feature confirmed by sputtering experiments of TiO_2 sintered pellets.

A sputtering coefficient S (mean atoms of the target sputtered/incident ion) can in principle be determined by simply measuring the weight loss against ion dose. Care in interpreting the weight loss is essential however, because

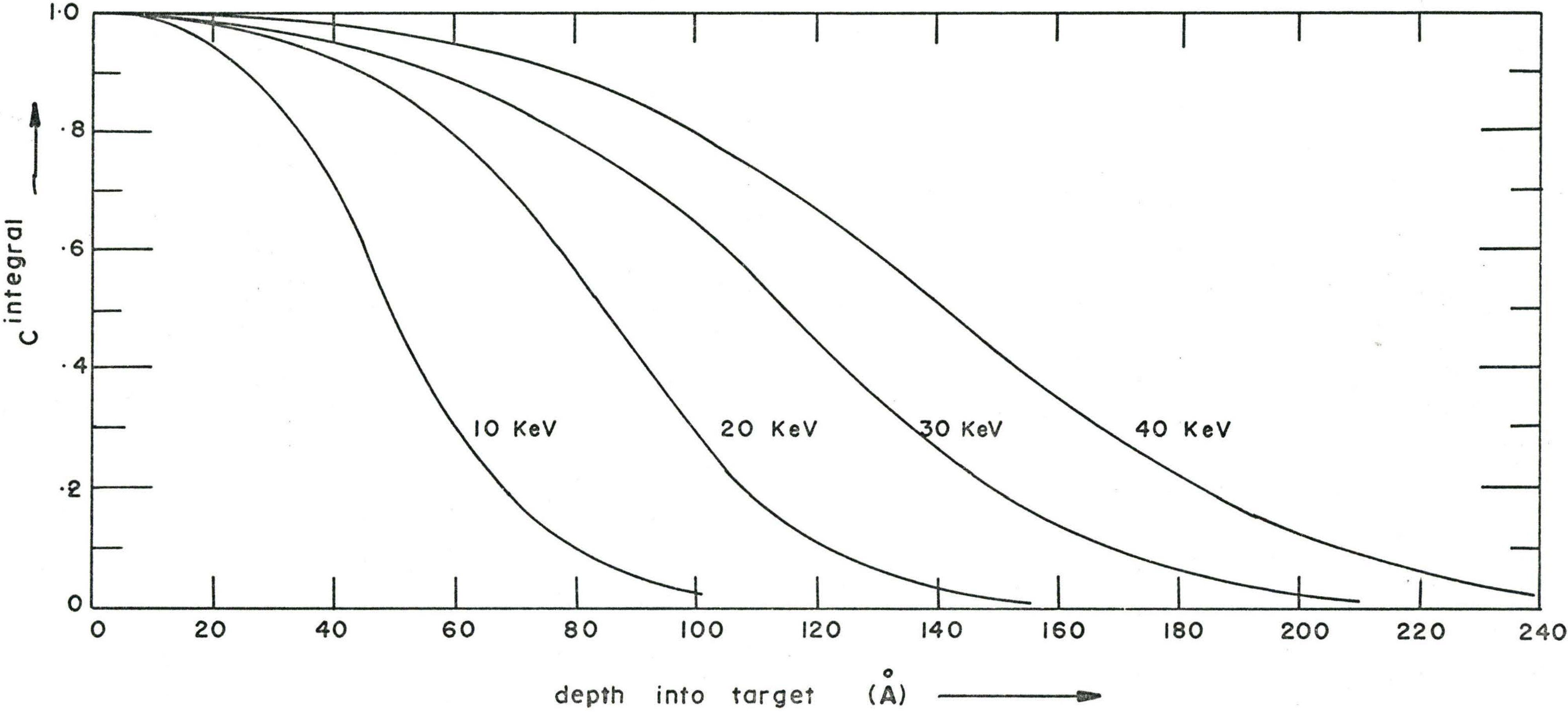

Figure 5.5 Integral concentration profiles of Kr in a random TiO_2 target

ions become trapped in the target material and are subject to what has been called "gas sputtering".

Figure 5.6 illustrates the activity versus dose of $_{36}Kr^{85}$ bombarded TiO_2. Although a rapid increase in activity occurs, the increase saturates at approximately 60 μamp-min/cm^2 - an energy dependent threshold |52|. Above this value incident ions, ions trapped in the target and target atoms interact; gas sputtering and target sputtering therefore occur to such an extent that the rate of ion introduction is balanced by loss through gas sputtering. In the <u>saturation</u> region then, the weight loss is a true measure of the TiO_2 sputtered with time, with the qualification that we realize that S so determined, is for Kr saturated TiO_2.

Analysis of the weight vs dose curve (Figure 5.7) in the linear region yielded, for 30 KeV, 10 μamp, Kr:

$$S = 4.2 \text{ mean atoms/incident Kr ion}$$

which agrees with the value extrapolated from low energy TiO_2 sputtering data |30|.

The thickness of material sputtered during ion bombardment of energy E, ion beam current B, and time t, is given by the relation |3|:

$$c = |Bt \cdot S(E)|/N \qquad (5.9)$$

where N is the atomic density (9.65×10^{22} atoms/cm^3 for TiO_2). Therefore at a high dose of say 1×10^{17} ions the thickness sputtered would be approximately 450 Å, an appreciable distance when compared to the $\langle R_p \rangle$ at 30 KeV which was shown to be 113 Å. One must conclude that the ideal Kr ion integral concentration must be modified for this surface sputtering.

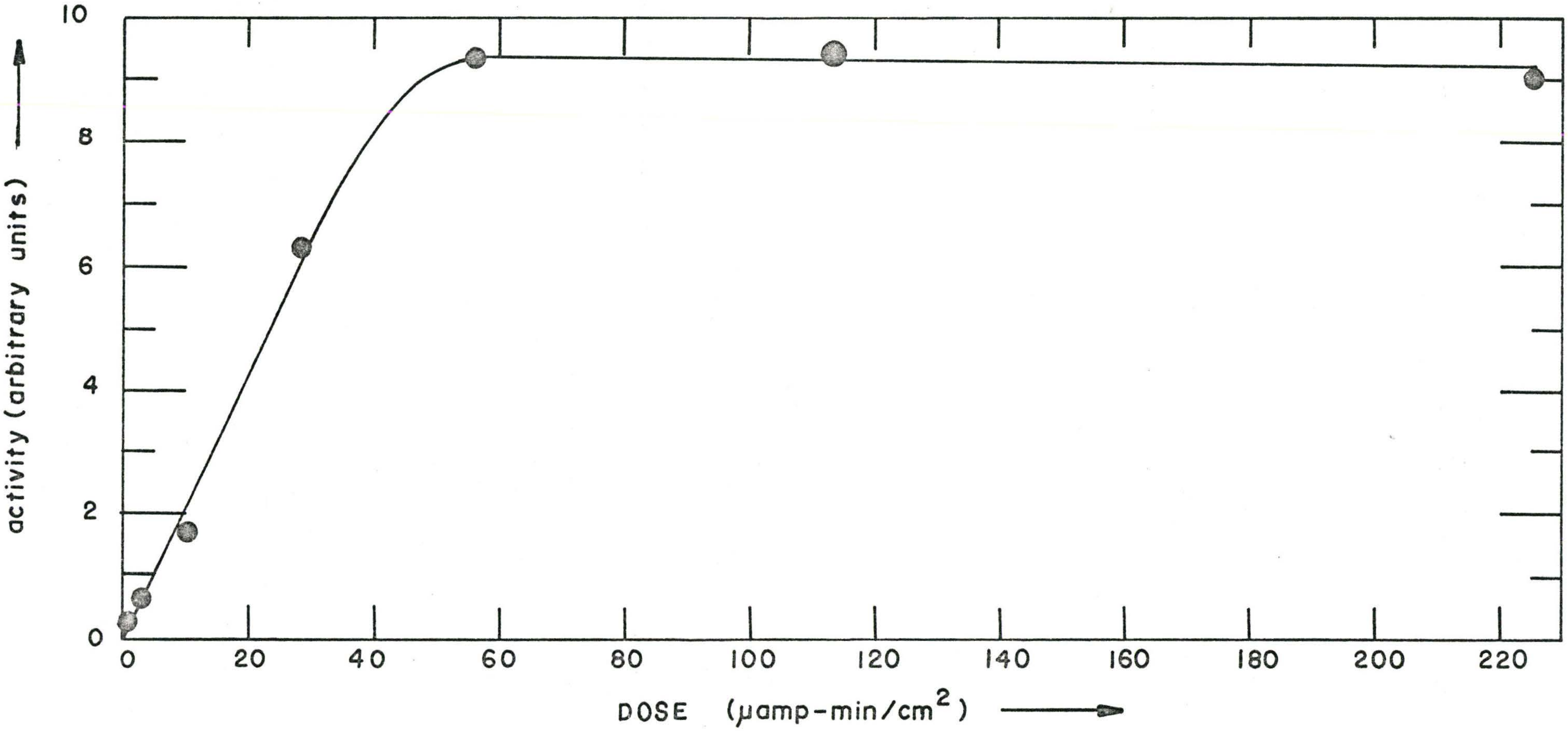

Figure 5.6 Activity remaining in a TiO_2 sample as a function of the Kr ion dose.

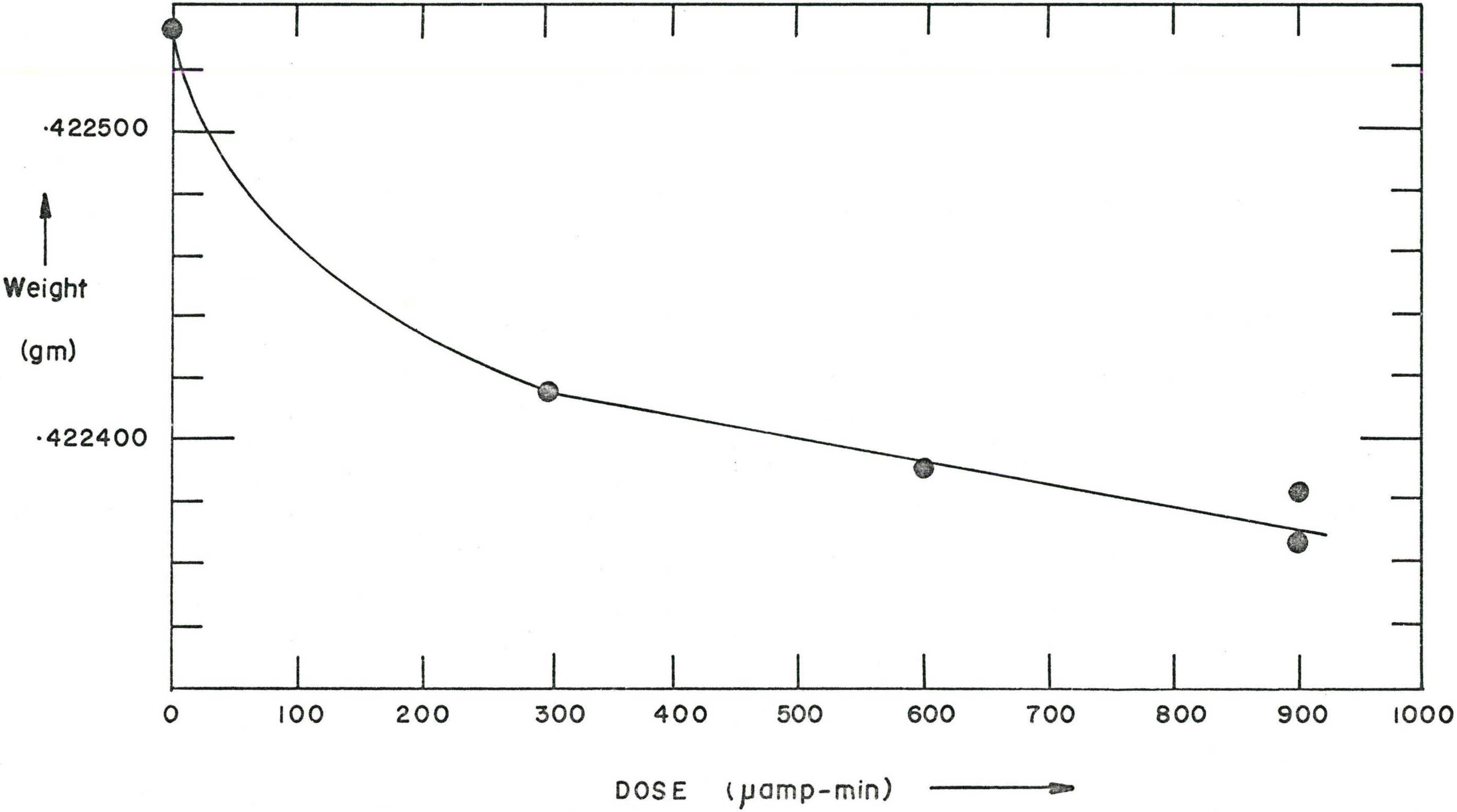

Figure 5.7 TiO_2 sample weight loss due to sputtering as a function of Kr ion dose.

5.2.4 Kr ion integral concentration profiles with a moving boundary resulting from surface sputtering:

If no surface sputtering occurred the differential Kr ion concentration profile in TiO_2 would take on the typical form of Figure 5.8 curve (A) with mean projected range $<x>$ defined with respect to the surface $x = 0$. This would be true at time $t = 0$ for the case of surface sputtering, such that at any point x_1 we have,

$$C^{diff}(x_1,0) = \frac{1}{\sqrt{2\pi}\mu} \exp - \left[\frac{(x_1-<x>)^2}{2\mu^2}\right] \qquad (5.10)$$

where μ = standard deviation $<\Delta R_p>$ or 2nd moment of the Edgeworth expansion of the Gaussian distribution

$<x>$ = the mean projected range $<R_p>$, as before.

However at any time $t > 0$, the newly formed differential profile will have moved toward the right as shown by curve (B) in Figure 5.8 since some surface depth is sputtered. The newly formed profile associated with the new surface would be at the same point x_1,

$$C^{diff}(x_1,t) = \frac{1}{\sqrt{2\pi}\mu} \exp - \left[\frac{(x_1 - vt - <x>)^2}{2\mu^2}\right] \qquad (5.11)$$

where v is the velocity of the moving surface as defined by the sputtering rate. Hence, at any point x_1, the <u>total</u> differential concentration of the Kr will be the sum of <u>all</u> the profiles generated in the specific time interval $t = 0$ to $t = T$:

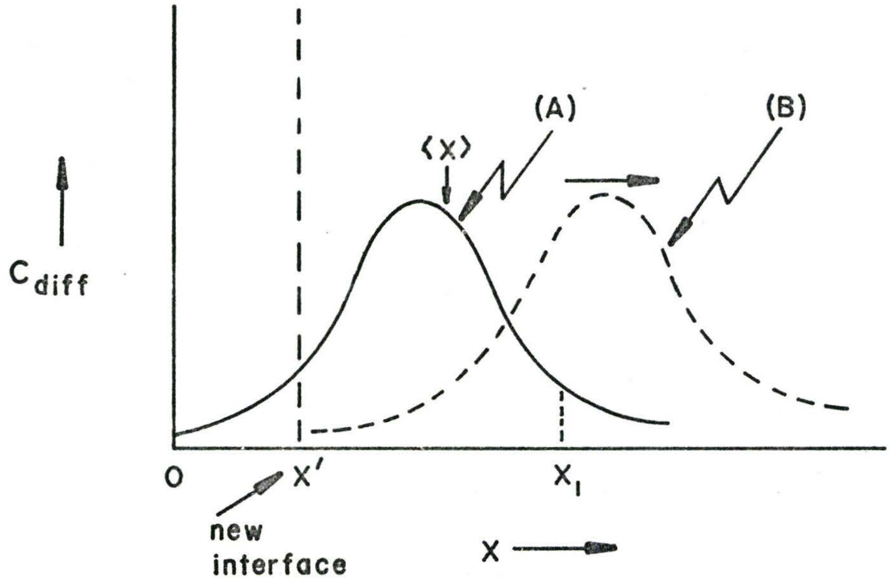

Figure 5.8 An ion concentration profile:

(A) without surface sputtering and

(B) with a distance x' sputtered away.

$$C^{diff}(x_1,T)_{total} = \int_0^T AC^{diff}(x_1,t)\,dt = \frac{A}{\sqrt{2\pi}\mu}\int_0^T \exp -\left[\frac{(x_1-vt-\langle x\rangle)^2}{2\mu^2}\right] dt$$

$$A = \text{a constant} \qquad (5.12)$$

which is solved by changing variables and the corresponding limits of integration with the result that at the point x_1;

$$C^{diff}(x_1,T)_{total} = \frac{A}{2v}\left[\operatorname{erfc}\left(\frac{x_1-vT-\langle x\rangle}{\sqrt{2}\mu}\right) - \operatorname{erfc}\left(\frac{x_1-\langle x\rangle}{\sqrt{2}\mu}\right)\right] \qquad (5.13)$$

However as previously mentioned, the quantity of interest and that found experimentally is the integral concentration, and therefore the total differential concentration must be integrated from x to ∞ such that:

$$C^{int}(x_1,T) = \frac{A}{2v}\int_x^\infty \left[\operatorname{erfc}\left(\frac{x_1-vT-\langle x\rangle}{\sqrt{2}\mu}\right) - \operatorname{erfc}\left(\frac{x_1-\langle x\rangle}{\sqrt{2}\mu}\right)\right] dx \qquad (5.14)$$

Again the integration proceeds by a change of variables and integration limits to yield the integral concentration remaining in the sample beyond any point x as:

$$C^{int}(x_1,T) = \frac{A}{2v}\left\{\operatorname{ierfc}\left(\frac{x_1-vT-\langle x\rangle}{\sqrt{2}\mu}\right) - \operatorname{ierfc}\left(\frac{x_1-\langle x\rangle}{\sqrt{2}\mu}\right)\right\} \qquad (5.15)$$

However, the profile of interest is that which is generated by the new surface at depth x' = vT at the end of bombardment and which has an analytical solution since the integrals of error functions are known and tabulated |28|. Thus substituting x + vT for x_1 where x is the distance measured from the instantaneous surface in equation 5.15 gives:

$$C^{int}(x+vT,T) = \frac{A}{2v}\left\{\text{ierfc}\left(\frac{x - \langle x\rangle}{\sqrt{2}\mu}\right) - \text{ierfc}\left(\frac{x + vT - \langle x\rangle}{\sqrt{2}\mu}\right)\right\} \quad (5.16)$$

Since a high dose bombardment is equivalent to forming $C^{int}(x + vT,T)$ over a very long time (i.e. T → ∞) the integral concentration profile may be approximated by the steady state expression, which with respect to the new surface at x' has the form:

$$C^{int}(x,\infty) = \frac{A}{2v}\left\{\text{ierfc}\left(\frac{x - \langle x\rangle}{\sqrt{2}\mu}\right)\right\} \quad (5.17)$$

$$\approx \frac{\sqrt{2}\mu}{2\langle x\rangle}\left\{\text{ierfc}\left(\frac{x - \langle x\rangle}{\sqrt{2}\mu}\right)\right\} \quad (5.18)$$

where the second expression is normalized.

This expression has been evaluated numerically in Figure 5.9-(A) for the mean projected range and standard deviation for 30 KeV Kr in TiO_2 and in this form is applicable to the dissolution experiments used to estimate the altered layer thickness, W.

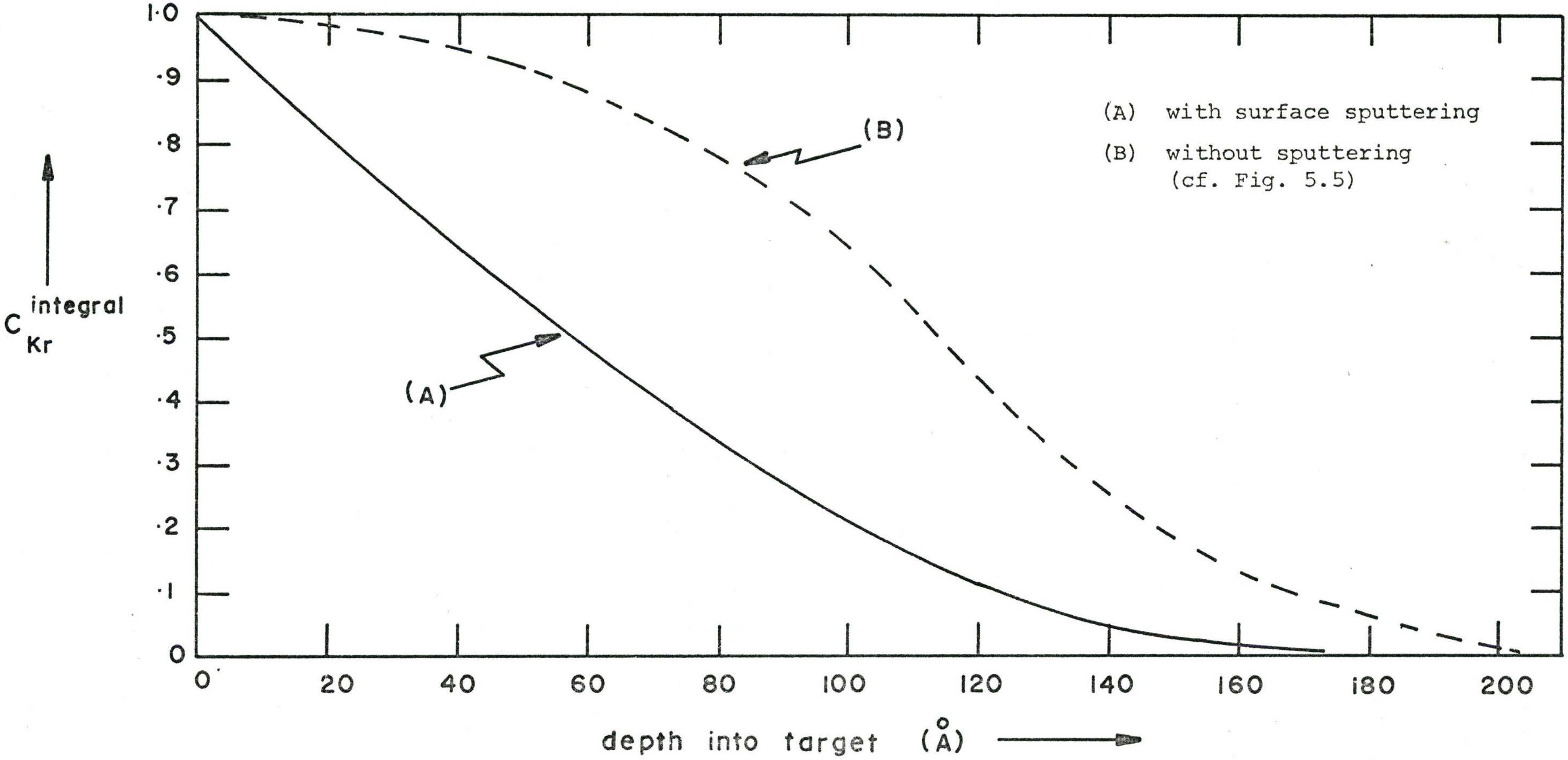

Figure 5.9 An integral concentration profile for 30 KeV Kr in TiO_2 as a function of the depth into the solid.

SECTION 6

Estimates of the Altered Layer Thickness, W, on Pellets and Single Crystals

6.1 W, based on electrical conductivity measurements

This approach has been considered already (Section 2.3.10). For an assumed bulk conductivity (σ) for Ti_2O_3 of $2 \times 10^{+1} \pm 0.5 \times 10^{+1}$ ohm^{-1}-cm^{-1} and a measured (I/V) of 1×10^{-4} (± 1 std. dev.) and invoking Valdes case #7 for an infinitely thin conducting layer on a non-conducting substrate, W must be 110 Å within an error range extending from 70 to 170 Å.

6.2 W, based on electron diffraction observations

This approach has also been previously discussed (Section 2.3.8) in which it was argued that the amorphous layer, hence the later altered layer, must be only of the order of 100 Å in order to have a diffraction pattern of the substrate generated in occasional back-reflection plates.

6.3 W, based on dissolution experiments

6.3.1 General - Dissolution experiments of a radioactive-ion labelled target are often valuable in determining the depth of alteration introduced by ion bombardment. For example, TiO_2 transforms to Ti_2O_3 on the surface, however the question

(Sections 6.1 and 6.2 notwithstanding) of the thickness remains. If a suitable solvent is chosen which dissolves the altered layer at a much faster rate than the substrate, the overall dissolution of the specimen will effectively stop when the substrate is reached. Such dissolution experiments were carried out on both single crystal and polycrystalline TiO_2.

6.3.2 Single crystal rutile - (a) Single crystal specimens were bombarded along the <100> with Kr ions to various dose levels followed by the introduction of a ${}_{36}Kr^{85}$ radioactive label. The crystals were then dissolved in 10% HF saturated in NH_4F and the activity measured after dissolution intervals. The results in Figure 6.1 are those expected for no surface layer alteration. The lowest doses do not damage TiO_2 appreciably hence the dissolution is exceedingly slow. As the dose increases the crystal sustains some damage and dissolves at a faster rate. However there is no surface alteration present and the dissolution curves simply reflect the Gaussian type ion distribution buildup that would be expected as the channeling component decreases. Even at the highest dose there is no rapid dissolution of the surface, followed by a cessation of the dissolution. (b) - Bombarding 30° from the <100> axis yielded the curves of Figure 6.2. Since (I/V) induced by off-axis bombardment was similar to that for pellets that transformed to Ti_2O_3 on the surface, one would expect a drastic change in the dissolution behaviour from that of Figure 6.1. The curves (Figure 6.2) do in fact exhibit

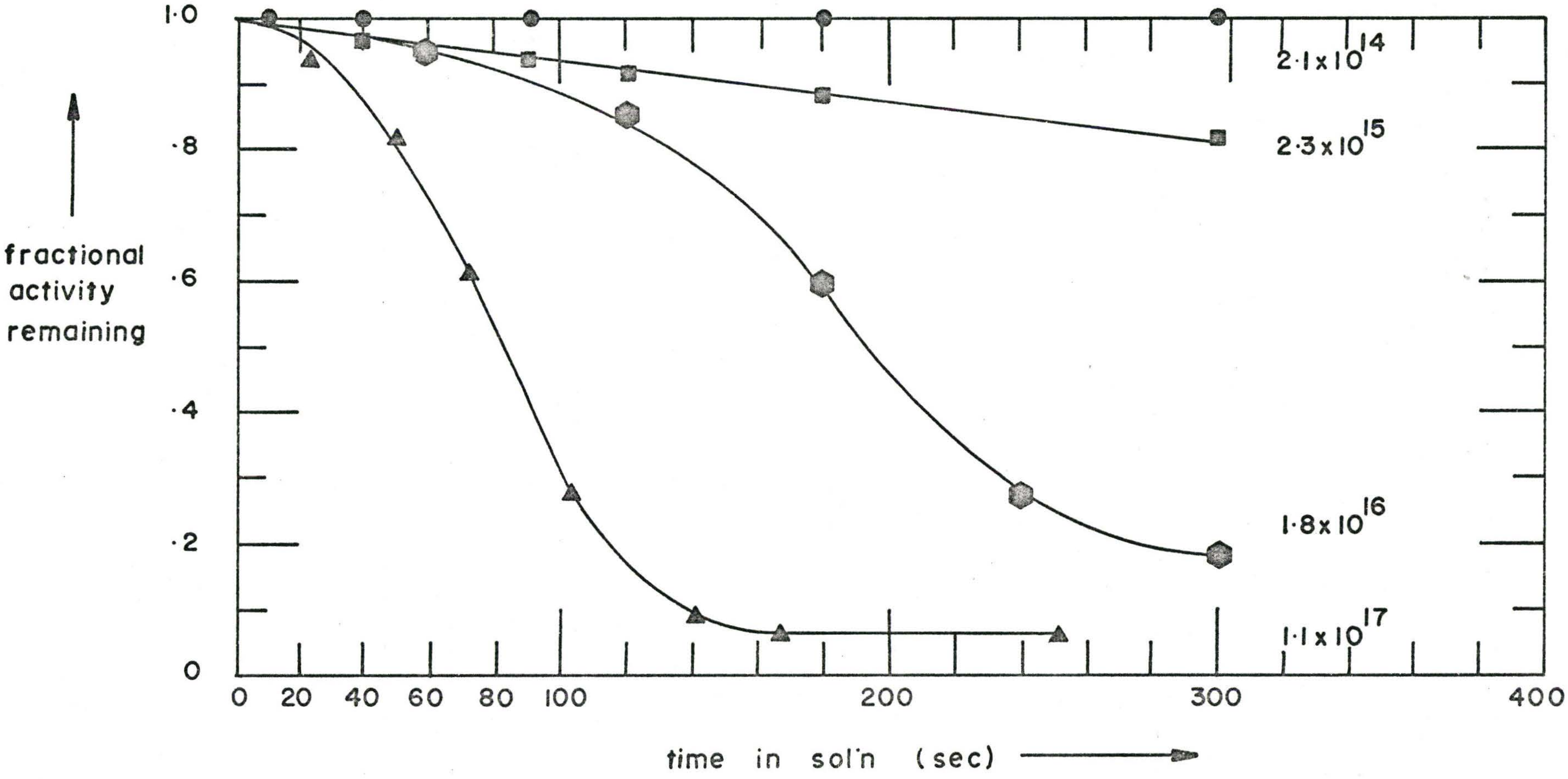

Figure 6.1 Fractional activity remaining vs Time in solution for TiO$_2$ single crystal rutile bombarded perpendicular to the prepared surface with Kr to the indicated dose.

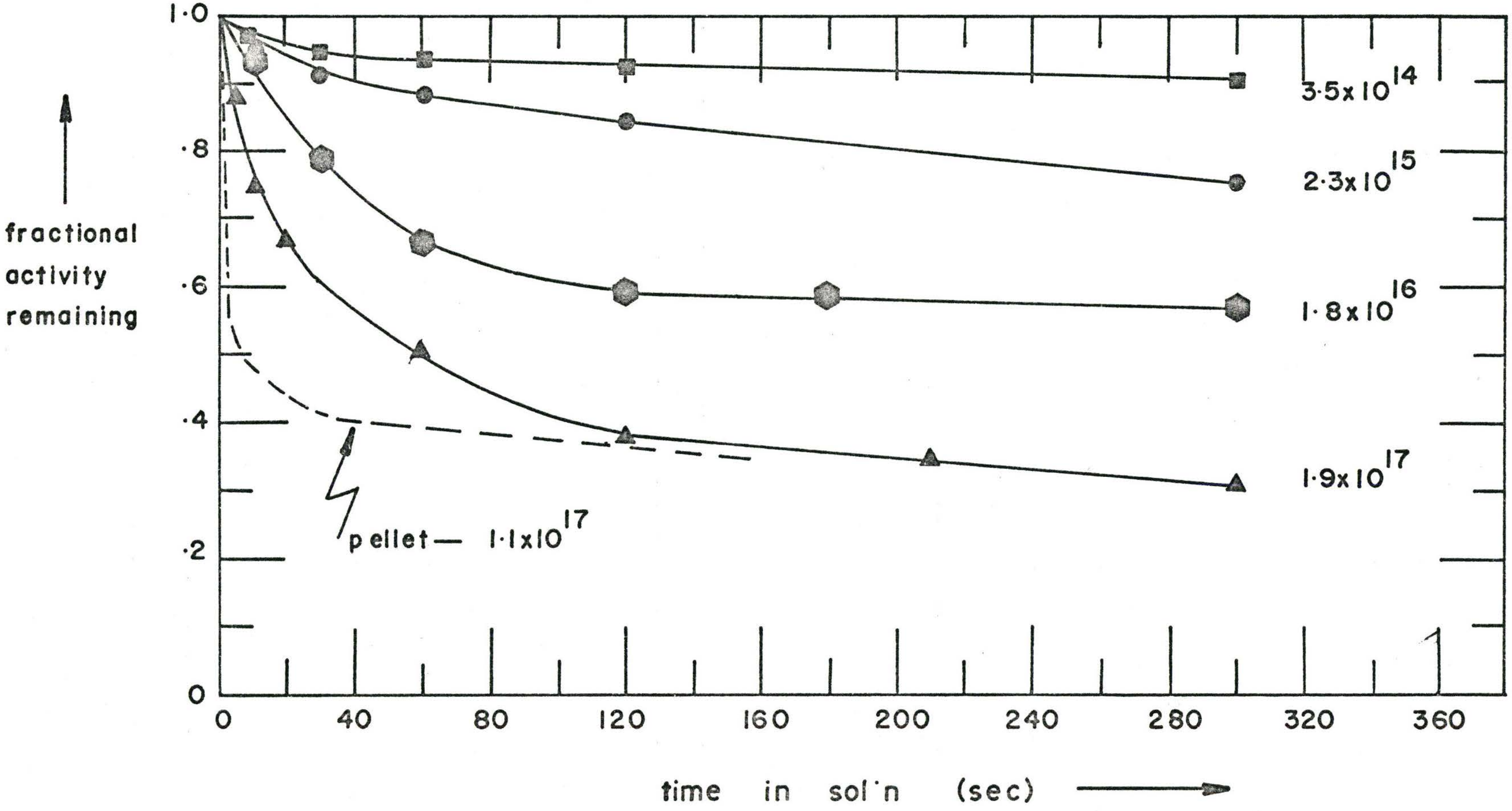

Figure 6.2 Fractional activity remaining vs time in solution for single crystal rutile bombarded at 30° off axis with Kr ions.

the unmistakable characteristic of rapid dissolution of an altered layer followed by slow dissolution of the substrate. Note that even at the highest dose the onset of "slow" dissolution occurs when there is still a large fraction of the label in the material. In the 1.9×10^{17} ions/cm^2 bombardment then, the depth of the alteration may be known if the integral ion concentration profile is known. Even though the specimen is single crystalline, off-axis bombardment closely approximates a random target arrangement (Section 4.4.1). Assuming that to be true, one would expect a Kr-ion profile in the single crystal to be that of Figure 5.9-(A). From Figure 6.2 for 1.9×10^{17} ions/cm^2, rapid dissolution stops while .35 to .40 of the original activity remains. The corresponding depth from Figure 5.9-(A) is 70 to 80 Å. (With no surface sputtering (Figure 5.9-(B)) the altered thickness would be approximately 125 to 130 Å.)

6.3.3 Polycrystalline rutile - sintered pellet - Figure 6.2 also includes the dissolution curve for a high dose ($>10^{17}$ ions/cm^2) pellet of TiO_2. Note that the residual activity at the onset of slow dissolution is almost that of the single crystal. Hence, W is again approximately 70 to 80 Å (or 125-130 Å) in reasonable agreement with the other methods of estimation.

SECTION 7

Bombardment Induced Changes in Thin Films of TiO_2 and Ti in Energetic Krypton and Oxygen-ion Beams.

Enhanced (I/V) response has been demonstrated for sintered TiO_2 powder compacts and rutile single crystals. Therefore it was attempted to show that the effect also held for thin films of TiO_2 bombarded with Kr, since one would expect Ti_2O_3 again to be formed and readily identified since thin films are particularly amenable to structural analysis in transmission electron diffraction (T.E.D.). The expected lower oxide formation was not found and the response of the amorphous sputtered thin films was to crystallize to rutile in the direct ion beam and to anatase in the surrounding heat affected zones.

Alternatively, evaporated thin films of Ti metal were bombarded with oxygen to determine whether Ti_2O_3 is the final stable product via this route. Interestingly electron diffraction revealed the formation of TiO (NaCl type) and this substance persisted to doses beyond 10^{17} oxygen ions/cm^2.

7.1 TiO_2 Sputtered Thin Films

7.1.1 Preparation - Thin films of TiO_2 were prepared by the D.C. reactive sputtering of a Ti metal cathode onto NaCl substrates in a atmosphere of 50% Ar/O_2. The apparatus used was similar to that shown in Figure 7.1. A glow discharge of Ar was induced by a potential placed between the Ti cathode and the anode, the latter serving to hold the NaCl substrates. The Ar accelerated to the Ti target caused sputtering of the Ti, which then impinged on the NaCl and reacted with the oxygen to form an amorphous or crystalline thin film of the highest stoichiometry in the Ti-O system namely TiO_2. Deposited films were floated off the substrate by dissolution of the NaCl in distilled H_2O and subsequently mounted on Cu or Pt specimen grids for examination in the Philips EM-300 operated in the transmission mode |Appendix I|.

7.1.2 Structures of R.T. sputtered films - Figure 7.2(a) is a transmission micrograph (9200x) of an "as-deposited" reactively sputtered film. The corresponding diffraction pattern, Figure 7.2(b) illustrates the amorphous nature, hence the uncertainty in the stoichiometry, a result previously reported |31| for the vacuum evaporation of titanium dioxide films onto rocksalt. In order to crystallize the films into one of the TiO_2 forms (rutile, brookite or anatase), (i) thermal and (ii) electron beam heating were attempted.

(i) Furnace heating of the as-deposited film in air at 800°C for 20 hours in an attempt to produce rutile† yielded

---

† Although rutile, anatase and brookite have the same stoichiometry, $\langle R_p \rangle$ values will differ due to varied atomic densities |27|, hence to assure structural consistency (e.g. pellets, single crystals, and thin films) it was necessary to try to produce rutile thin films.

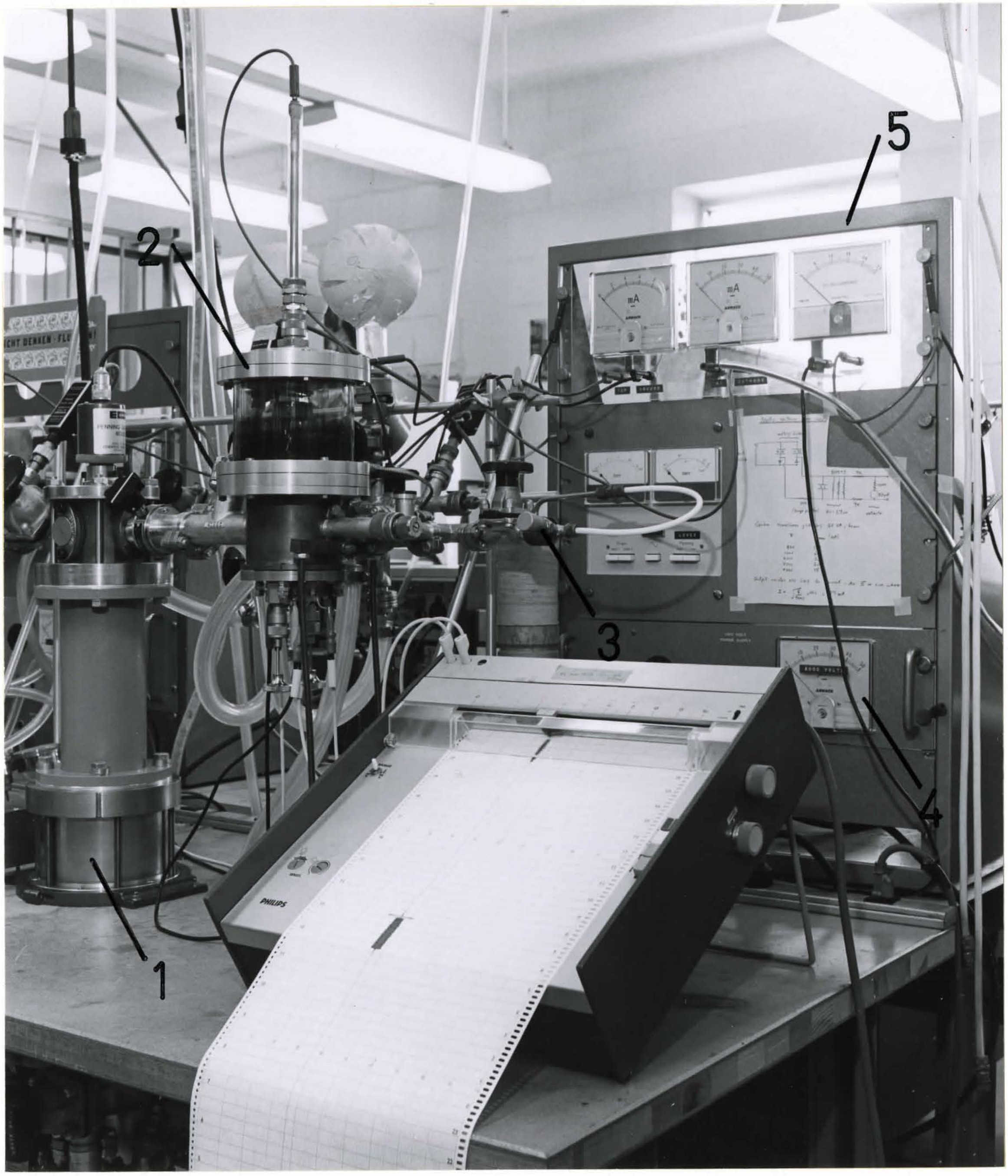

Figure 7.1 Reactive Sputtering Apparatus; 1 - vacuum system; 2 - specimen chamber; 3 - gas mixture feed; 4 - sputtering power supply; 5 - pressure, current metering system.

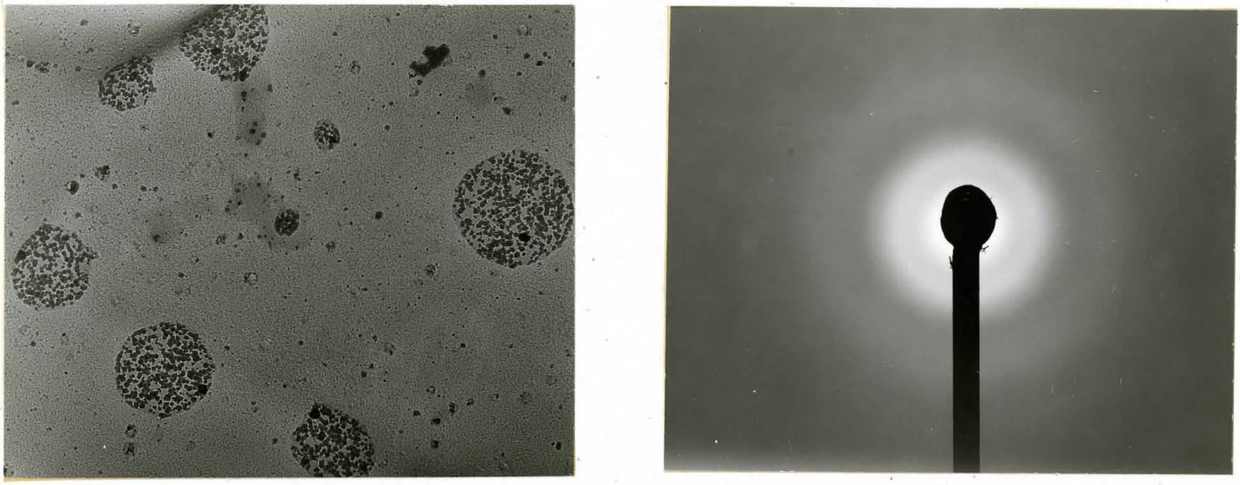

(a) (b)

Figure 7.2 As deposited thin film of amorphous (TiO_x) in (a) Transmission - 9,200 x and (b) diffraction.

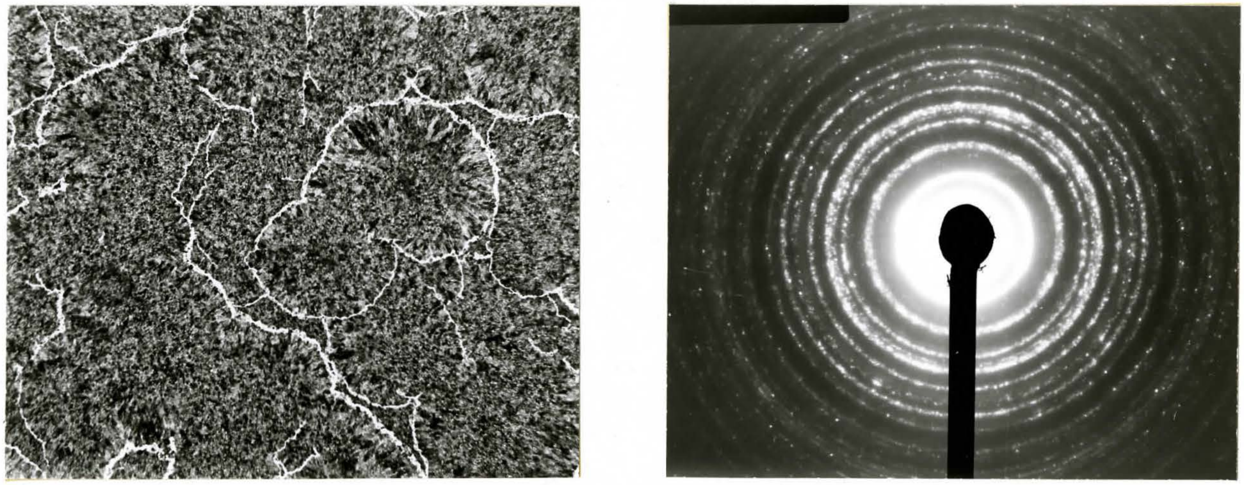

(a) (b)

Figure 7.3 TiO_x sputtered film heated in air at 800°C for 20 hours (a) in transmission 10,600x and (b) in diffraction (Anatase).

TABLE 7-I - Analysis of diffraction pattern 7.3(b)

Thin Film		Anatase - ASTM #4-0479	
I/Io (expt'l)	d(expt'l) (Å)	d (Å)	I/Io
100	3.51	3.51	100
20	2.41	2.435	9
10	2.35	2.379	22
20	2.31	2.336	9
60	1.87	1.891	33
40	1.74	?	
50	1.69	1.699	21
50	1.65	1.665	19
80	1.47	1.480	13
20	1.35	1.367	5
20	1.33	1.337	5
20	1.25	1.264	10

the fine polycrystalline structure of Figure 7.3(a). Analysis (Table 7.I) of the corresponding diffraction pattern (Figure 7.3(b)) showed the film to be anatase. Increasing the temperature to 1050°C again in an effort to produce rutile promoted only grain growth - the film remained anatase.

(ii) Heating in a low intensity electron beam, crystallized the film as evidenced by a crystallization front (Figure 7.4) moving across the specimen. Ahead of the front the film was still amorphous but behind, the film had transformed as before to a very fine polycrystalline anatase.

7.1.3 Hot substrate deposition - The stage used for R.T. sputtering was designed also as a hot stage, and in this mode further films were reactively sputtered in a 50% Ar/O_2 mixture. At a substrate temperature of 250°C, the "as-deposited films (Figure 7.5(a)) were now fine grained crystalline anatase (Figure 7.5(b)). At a still higher temperature 335°C, again the as-deposited films were crystalline (Figure 7.6(a)) however the diffraction pattern (Figure 7.6(b)) was now that characteristic of TiO_2-brookite (Table 7-II).

In none of the sputtered films was the rutile structure encountered, namely neither in furnace heating in air, nor in electron beam heating, nor in hot substrate sputtering. Hence "as-deposited" films were bombarded with Kr.

7.1.4 Bombarding TiO_2 thin films with Kr ions - As deposited R.T. sputtered films were bombarded with 30 KeV Kr through a 1000 mesh Cu grid. The irradiated specimen then consisted

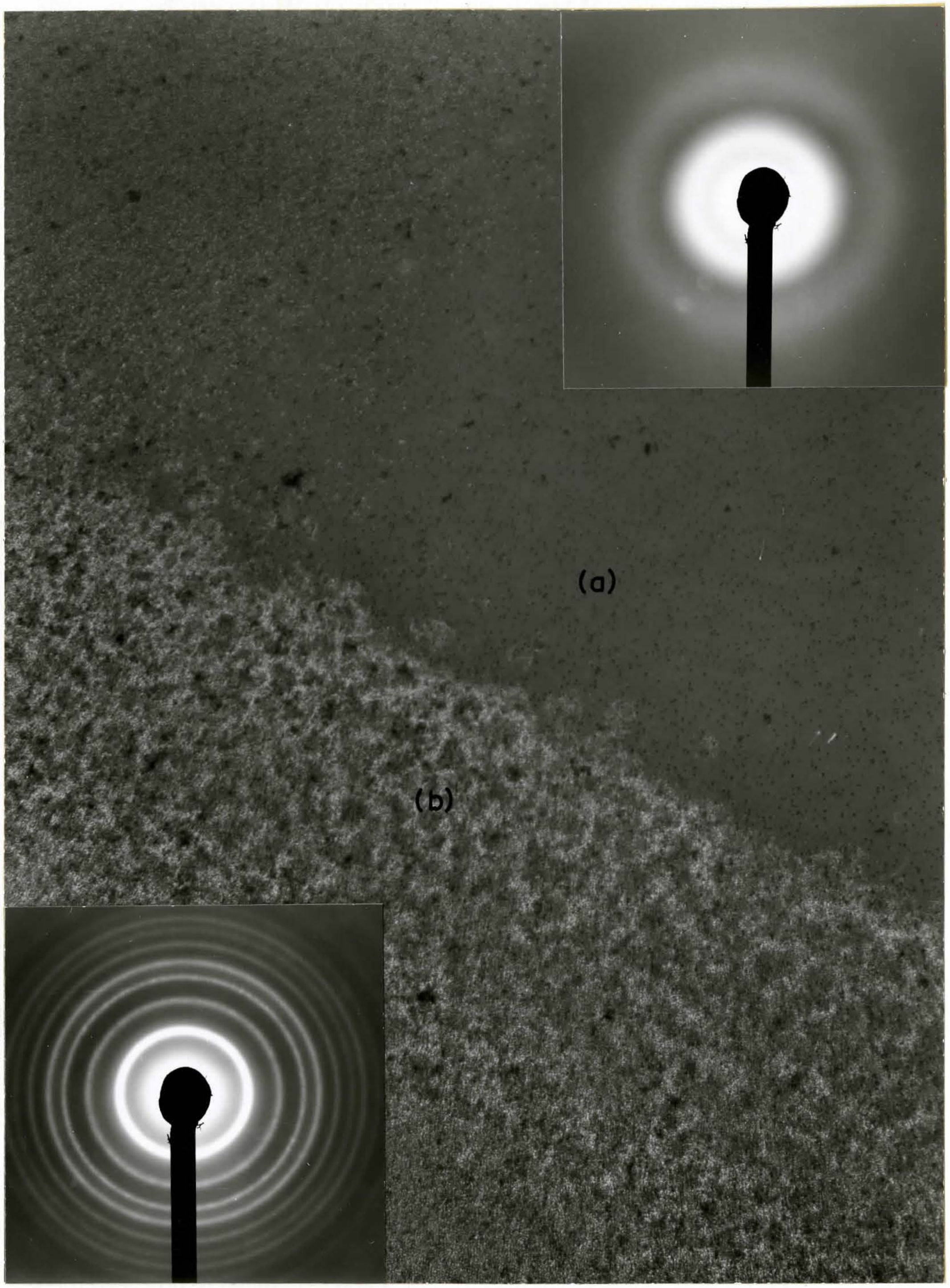

Figure 7.4 Electron beam heating of R.T. TiO_x sputtered thin film showing the crystallization front between (a) the amorphous and (b) the crystalline anatase phases.

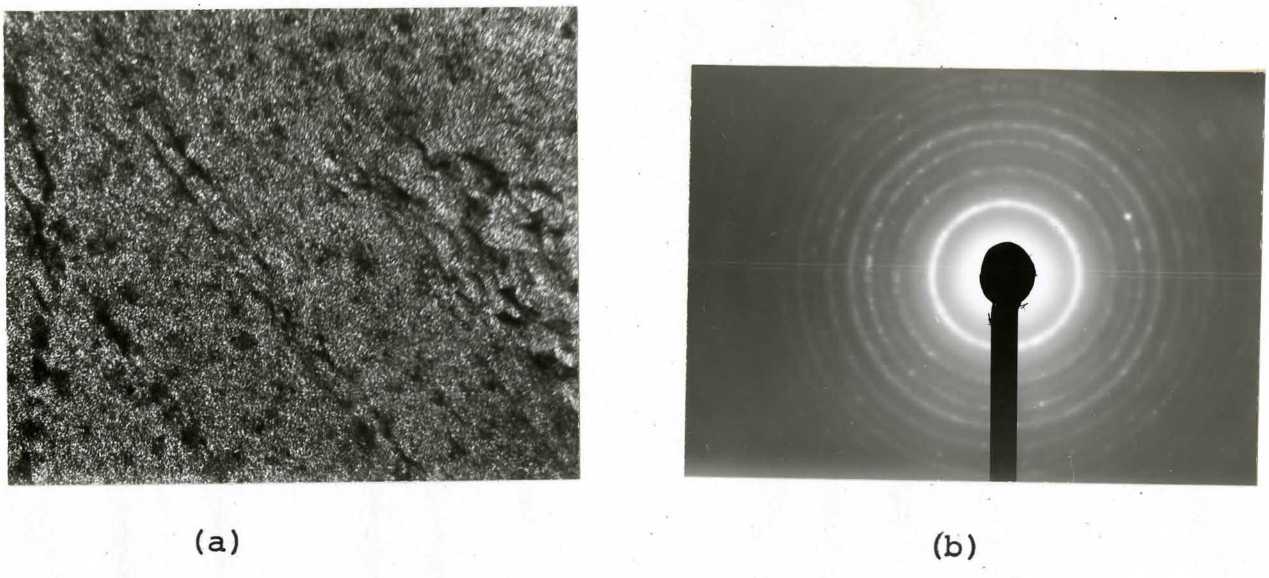

(a) (b)

Figure 7.5 TiO_x sputtered onto a hot substrate (250^{o}C) in (a) transmission - 10,500x and (b) diffraction.

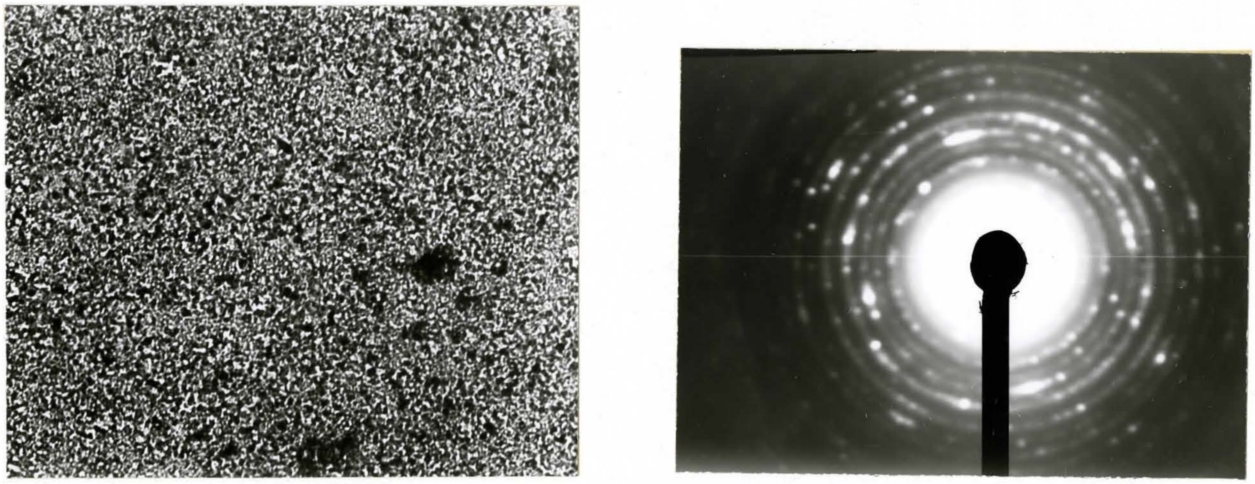

(a) (b)

Figure 7.6 TiO_x sputtered onto a hot substrate (335^{o}C) in (a) transmission - 34,400x and (b) diffraction.

TABLE 7-II - Analysis of diffraction pattern 7.6(b)

Hot substrate sputtered film		Brookite ASTM #16-617	
I/Io (expt'l)	d (expt'l) (Å)	d (Å)	I/Io
100	3.53	3.51 3.47	100
10	2.90	2.90	40
60	2.36	2.409	18
40	2.09	2.133	30
60	1.88	1.893	30
80	1.67	1.662	10
40	1.47	1.466	10
20	1.34	1.336	10
20	1.255	1.238	10

of an unirradiated but heat affected grid shadow and a matrix of directly bombarded squares.

(i) Medium dose - The exposed regions (i.e. squares) after medium dose bombardment had the characteristic rutile diffraction pattern while the surrounding heat affected region was not amorphous but had transformed to anatase similar to section 7.1.2. Radial dark bands about the squares were the bend extinction contours due to film buckling which could be associated with the density difference between rutile and anatase (4.26 vs 3.84 gm/cm^3 respectively).

(ii) High dose (170 μamp-min/cm^2 or 6.3×10^{16} ions/cm^2) Bombarding as before using a 1000 mesh Cu grid, to higher doses still produced the same results, namely squares of rutile surrounded by anatase. The behaviour is graphically summarized in Figure 7.7.

Even at the highest doses, the analog of Ti_2O_3 formation in oxide pellets did not occur for the case of thin films, in fact the only result was to sputter the thin film completely leaving a symmetrical array of void areas. The most plausible explanation for not realizing Ti_2O_3 is that in thin film form there is a significant heating problem whence annealing processes (e.g. above say 200°C) override the possibility of radiation damage accumulating enough to generate the lower oxide.

7.2 Ti metal thin films

7.2.1 General - Since Ti_2O_3 is the stable product of inert gas bombardment of TiO_2 (the thin film experiments notwith-

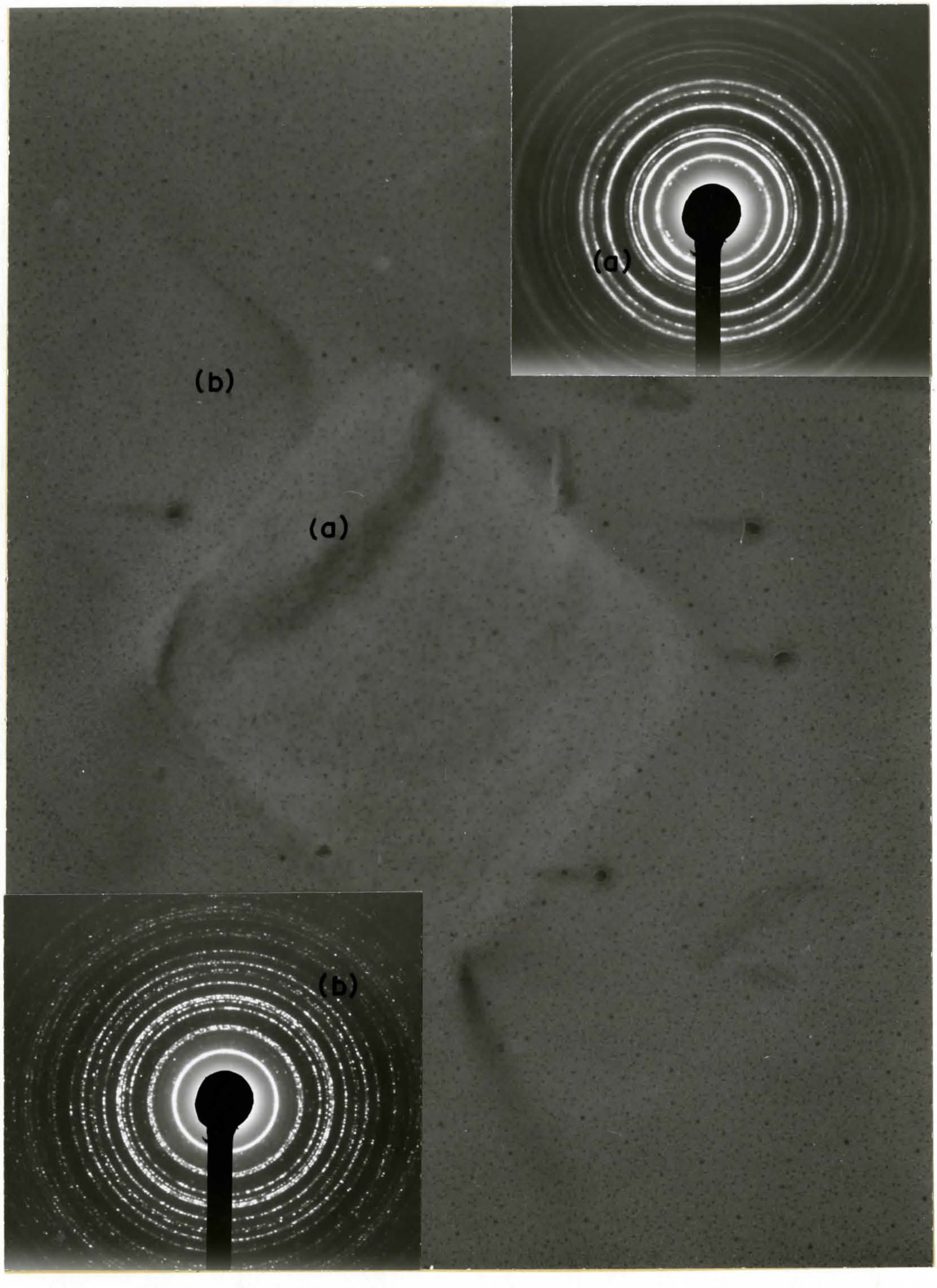

Figure 7.7 High dose Kr ion bombarded TiO_2 (R.T. sputtered) through a 1000 mesh Cu grid producing a (a) square of rutile (b) surrounded by anatase.

standing) it was considered of interest to investigate whether it also represents the end result when approached from the other direction, namely oxygen bombardment of Ti metal.

7.2.2 Preparation and thin film analysis - Ti metal films were prepared by evaporating Ti onto NaCl substrates at R.T. in a standard evaporator[†] at 6 x 10^{-6} Torr. Film thickness was controlled by varying the NaCl exposure time to the molten Ti in a W boat. The films again were floated off in distilled water and mounted on grids. The as-deposited films exhibited amorphous halos, however slight electron beam heating generated a well defined pattern which was α - Ti the expected structure as shown in Table 7-III.

7.2.3 Oxygen-ion bombardment - At doses as low as 2.4 x 10^{16} ions/cm^2 and greater than 1.0 x 10^{17} ions/cm^2 oxygen ion bombardment produced only one structure namely, TiO (NaCl type) (Table 7-IV) the development and persistence of which is summarized in the series of diffraction patterns in Figure 7.8(a) to (d). Even at low doses the diffraction pattern (Figure 7.8(a)) shows an ordered state of the oxygen to be present similar to Andersson's αTi-Ti_2O |45| and by 2.4 x 10^{16} ions/cm^2 the transformation to TiO (NaCl type) is completed. There was no evidence of the generation of higher oxides, although it is conceivable that at extreme doses, for example, greater than 10^{19} ions/cm^2, other phases might appear.

[†] Model CVE-15, Bendix, Rochester, N.Y.

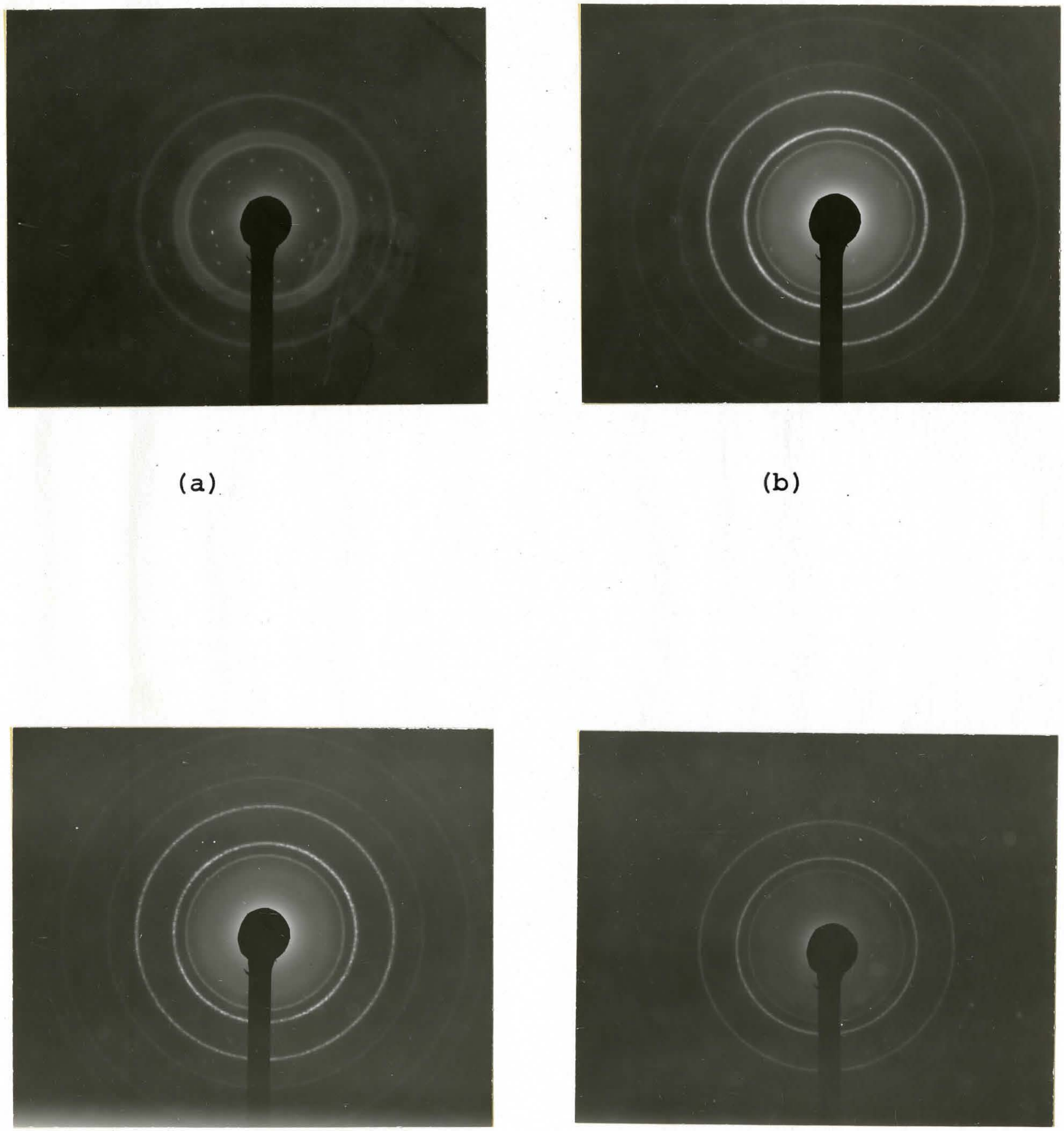

(a) (b)

(c) (d)

Figure 7.8 (a) to (d) - Diffraction patterns of evaporated Ti thin films bombarded with oxygen to the indicated doses in ions/cm^2. (a) 2.4×10^{15}, (b) 2.4×10^{16}, (c) 7.1×10^{16}, (d) 1.4×10^{17}.

TABLE 7-III Analysis of e^- beam heated evaporated Ti thin film

Diffraction pattern		α-Ti ASTM 5-0682	
I/Io	d (Å)	d (Å)	I/Io
60	2.51	2.56	30
100	2.14	2.24	100
100	1.51	1.48	17
10	1.24	1.25 1.23	16
faint	1.07	1.07	3
10	.956	.946	11
5	.866	.863	2

TABLE 7-IV Analysis of diffraction pattern 7.8(b)

Diffraction pattern		TiO (NaCl type)†	
I/Io	d (Å)	d (Å)	I/Io
60	2.38	2.417	80
100	2.063	2.092	100
80	1.46	1.480	100
10	1.24	1.262	60
40	1.19	1.208	60

† |44|

SECTION 8

Overall Discussion and Interpretation of Results

8.1 Possible mechanisms involved in the production of a lower oxide by Kr-ion bombardment

The effect of Kr ions on TiO_2 is the catastrophic disruption of the TiO_2 lattice. First there is the amorphization of the initially crystalline TiO_2 surface, an effect common to some 16 other oxides |60|. Further, however, a loss of oxygen from the lattice occurs until the well defined stoichiometry Ti_2O_3 is reached, at which point the Ti_2O_3 crystalline form appears on the surface, perhaps by bombardment-induced crystallization analogous to that found for ZrO_2 and other oxides |60|. This surface Ti_2O_3 persists under further bombardment. Associated changes in the electrical conductivity and colour are consistent with the surface transformation to Ti_2O_3.

Estimates of the thickness of the conducting layer are in the range of 100 Å, and since the mean projected range $<R_p>$ of 30 KeV Kr ions in TiO_2 is 113 Å |Section 5.2.1|, it is tempting to conclude that the phenomenon of bombardment induced oxygen loss is mainly collisional. (One would conclude this since the mean projected damage range $<R_d>$, would be slightly less than $<R_p>$ for heavy ions on TiO_2 |61|.)

However, this conclusion would seem premature since over the 113 Å Kr ion range or somewhat greater one could envisage the following processes occurring:

8.1.1 Mechanism (a) - Collisional

Oxygen atoms are displaced internally (i.e. collisionally) and then either precipitate internally in an athermal manner or precipitate as a result of diffusion to nucleating centers. In effect, the behaviour is analogous to that postulated with regard to neutron |36| or oxygen |37| bombarded LiF. Van der Bosch suggests that, for high neutron doses, as much as 8% of the Li exists in metallic precipitates and that the corresponding F may have escaped to some extent. Carroll and Birnbaum emphasize that the precipitated Li is finely polycrystalline in spite of the LiF being single crystalline, that the precipitation is thermally reversible and that the corresponding F is present as interstitial F_2 molecules or escapes.

One further example of this type of collisional phenomenon is the oxidation of Cu at R.T. in an energetic beam of oxygen ions for which Meyer |14| stated that the only factor affecting oxide growth was the ion penetration depth governed by the angle of incidence (and the ion energy).

In the case of TiO_2 many experimental facts support this collision type phenomenon.

(i) The damage layer extends to a depth commensurate with the penetration of Kr ions in TiO_2

(ii) The induced (I/V) saturates and remains constant suggesting that the altered layer has a well defined and constant thickness and must therefore move inward since it is experimentally known that the surface is sputtered away quite rapidly. Hence new material must continuously transform to Ti_2O_3 at the inner interface.

(iii) Annealing of the Ti_2O_3 in an inert gas[†] (see Section 3) revealed a reoxidation through some members of the homologous series Ti_nO_{2n-1} (e.g. Ti_4O_7) suggesting that the oxygen must indeed come from some internal source (e.g. precipitated O or O_2 molecules).

(iv) In the case of single crystal TiO_2 on which a polycrystalline structure developed under Kr ion bombardment, if the reintroduction of oxygen occurred at the surface one would expect polycrystalline TiO_2 on the surface after annealing in vacuum. However clearly the surface is single crystalline (Figure 4.4) hence the damage layer annealed out toward the surface not inward, and again the oxygen is inferred to originate from an internal source.

(v) Bombarding along a low index direction in a rutile single crystal, thus encouraging channeling, did not produce the same catastrophic increases in (I/V) as the off-axis bombardment. Since $\frac{dE}{dx}{}_{\eta}$ predominates with a random target at the ion energies involved, then, the oxygen loss is

---

[†] It is noted that oxygen impurities in the inert gas supply could provide a source of oxygen, however in that case one would have expected TiO_2 (rutile) at the highest temperatures since the diffusion length is so small.

predominantly a collisional process.

A schematic of this collisional mechanism is given in Figure 8.1.

8.1.2 Mechanism (b) - Preferential surface sputtering

Oxygen atoms are preferentially sputtered from the surface while at the same time oxygen vacancies (V_O) or Ti interstitials (Ti_i) diffuse to the interior. (Note that sputtering alone would not give the observed results unless the expelled atoms were postulated to come from depths up to or slightly greater than 100 Å, the latter figure being the estimated thickness of the Ti_2O_3 layer as discussed in Section 6.) A precedent for this mechanism, including the recognition that diffusion is a necessary concomitant process, occurs in work by Gillam |62| on the sputtering of binary alloys such as Cu_3Au[†]. Sputtering coefficients are high for Kr on TiO_2 namely 3-4 mean atoms/ion at an accelerating voltage of 30 KeV, and hence one could expect preferential oxygen sputtering, thus a net loss of oxygen in the target. Further, experimentally there is very little increase in (I/V) with oxygen bombardment, as would be expected from a sputtering point of view. Sputtering coefficients for the system O-TiO_2 were obtained in previous work |30| and revealed a value at 10 KeV of 0.6 mean atoms/ion. This is equivalent to 0.4 oxygen atoms/ion and even extrapolating to 30 KeV, leads to the obvious conclusion that a net oxygen

---

[†] this work was low energy only.

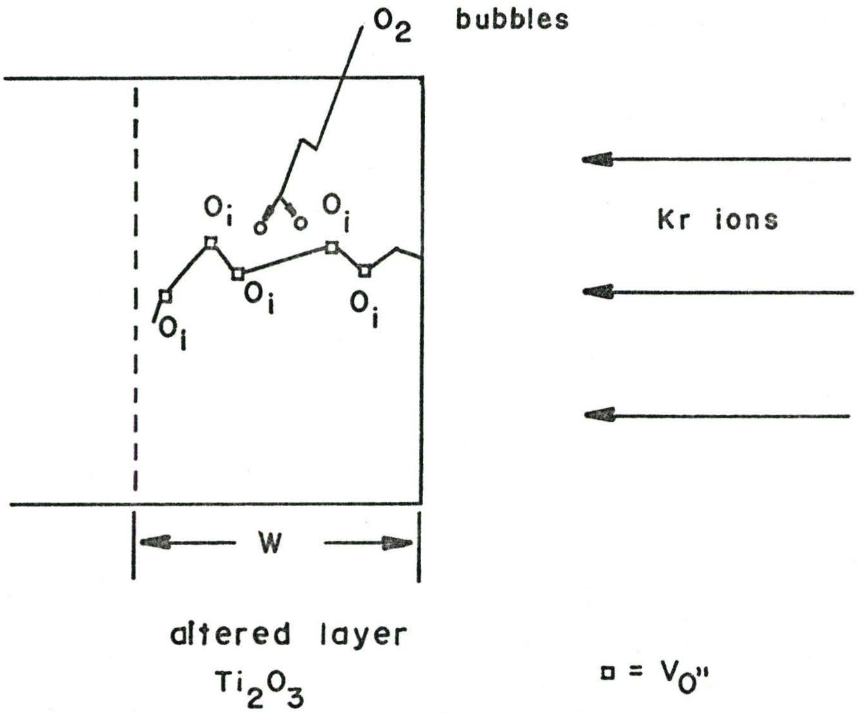

Figure 8.1 A collisional mechanism for the production of lower oxides of TiO_2 .

loss would be quite improbable during oxygen bombardment. Alternatively, since no net oxygen loss should occur (I/V) should show no change, but since it does (from 10^{-7} to 3×10^{-6} ohm^{-1} at 10^{17} ions/cm^2) there must be some internal collisional component to the oxygen bombardment.

This sputtering/diffusion mechanism is shown schematically in Figure 8.2.

8.1.3 Mechanism (c) - Thermal spike vaporization

Thermal spike vaporization occurs such that oxygen molecules are vaporized at the surface near an impact, while at the same time V_O or Ti_i diffuse to the interior. The main precedent here lies in work where sputtering was shown to be in part collisional and in part thermal |63,64|.

Thus an ion impact would distribute energy just beneath the surface of a solid (i.e. form a thermal spike) and cause atoms to evaporate. The analysis of this problem has been discussed elsewhere |47| and the conclusion only is quoted: impact induced oxygen loss from TiO_2 is not due to thermal spike vaporization in that the reaction $2TiO_2(S) = Ti_2O_3(S) + \frac{1}{2}O_2(g)$ has too low an oxygen pressure to occur to a significant extent.

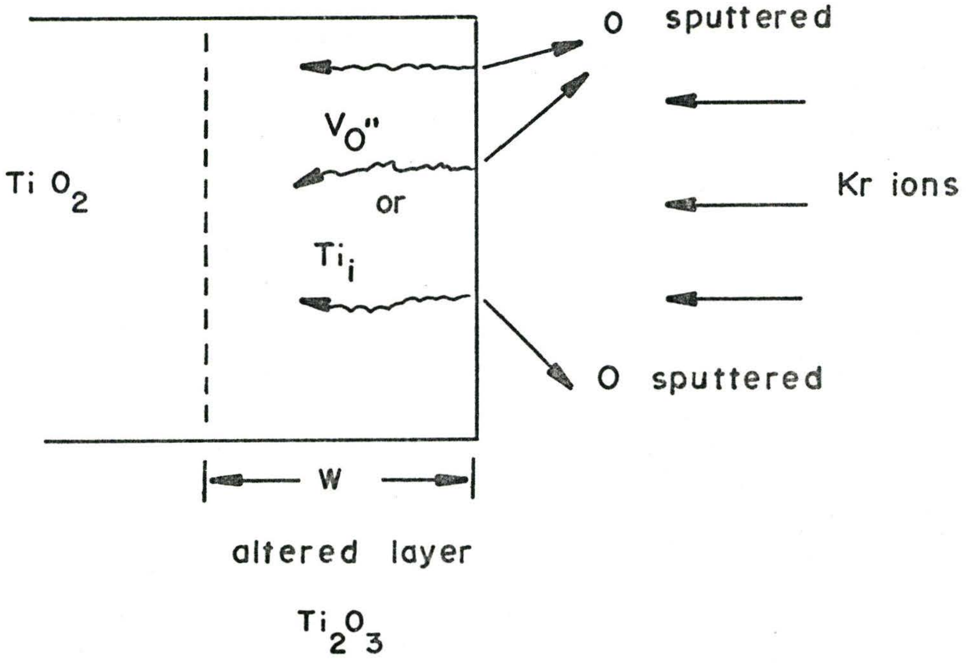

Figure 8.2 A sputtering/diffusional mechanism to produce a lower oxide of TiO_2 .

8.2 Ionicity criterion for the stability of TiO_2 on irradiation and the radiation stability of Ti_2O_3

The response of TiO_2 to heavy ion bombardment has been established as a process of amorphization, oxygen loss by a collisional or sputtering mechanism and crystallization to a lower oxide, Ti_2O_3. The question arises however as to why crystalline Ti_2O_3 is the end product, since numerous shear structures of the form Ti_nO_{2n-1} exist in the TiO_2 - Ti_2O_3 stoichiometry interval. One possible explanation is that Ti_2O_3 is the first oxide in the series that is stable with respect to further bombardment. Previous workers |65,73| have considered the nature of the bonding as a criterion for rationalizing the response of a wide range of materials to irradiation. In particular, a quantitative expression for the amount of ionic character of a binary material is given by the Pauling expression |33|:

$$\%\ \text{Ionic character} = 100\ \{1-\exp\ |-\tfrac{1}{4}(x_A - x_B)^2|\} \qquad (8.1)$$

where x_A and x_B are the electronegativities of the constituent atoms A and B respectively. The variation of the ionic character given by Equation 8.1 is illustrated in Figure 8.3. A tabulation of the calculated % ionic character of some 35 substances (including some oxides of V, W and Mo) of known radiation damage behaviour yielded the following criterion|8|:

$< 55\%$ ionic character - the material amorphizes readily.

60 to 63% ionic character - mixed behaviour.

$> 67\%$ ionic character - material is stable to radiation damage.

These limits are also included in Figure 8.3. In the case of TiO_2 irradiation, it is known experimentally that amorphization occurs |47,53| and further that Ti_2O_3 is stable to further irradiation |Sections 2.3.5 and 2.3.8|. Hence for consistency of the % ionic character criterion these observations should be predicted. Two series of electronegativity data were used, due to Gordy and Thomas |33| and Batsanov |34|, to determine ionic character. Where specific valence electronegativities were unlisted, values were inferred by analogy with the valence states of V and the electronegativity of oxygen was taken as 3.5 |33,34|. The predicted behaviour based on the ionic character is in fact consistent with the experimental observations. Hence as shown in Figure 8.3 TiO_2 should amorphize under impact and Ti_2O_3 should be stable with respect to further bombardment, once formed. This may explain why oxides in the homologous series Ti_nO_{2n-1} are not seen, that is, none of them is stable with respect to ion bombardment and only the first stable oxide (Ti_2O_3) is seen.

8.3 Thermodynamical considerations in the reduction of TiO_2 by Kr-ion bombardment.

Though Ti_2O_3 is the stable phase with respect to radiation damage the question arises whether thermodynamically one would predict this particular oxide as an end product. A cursory glance at an oxide Ellingham diagram |66| indicates that the reduction of any metal oxide will require energy input to the system since the spontaneous reaction is always

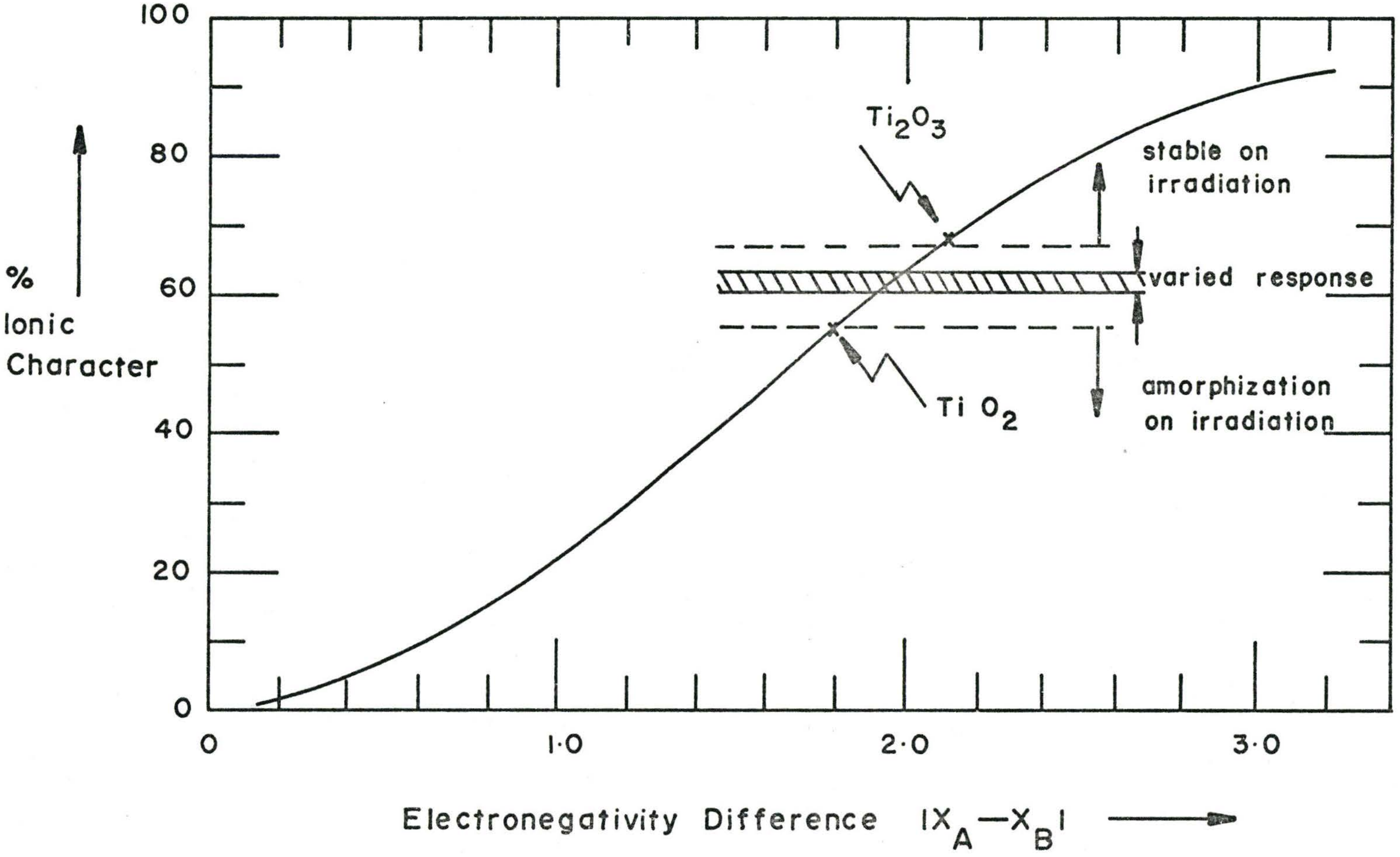

Figure 8.3 Ionic character vs. electronegativity difference and the target stability criteria.

toward metal oxidation. It would be reasonable to assume then that the reduction process that occurs is that which requires the least energy input (i.e. the most probable process), and produces an appropriate loss of oxygen without specifying the exact mechanism, provided that a mechanism does exist. Consider the reaction, for example;

$$TiO_2(S) = TiO(S) + O(g) \tag{8.2}$$

in which atomic oxygen is taken as the ejected species. The assumption of atomic oxygen is arbitrary, since the fate of the oxygen is not known experimentally. Possibly the oxygen is lost as an atomic species, however, it could be molecular O_2 or in fact may be precipitated internally. Nevertheless, if we assume that the fate of oxygen is always the same in comparing various reaction processes, free energy differences for the reaction will be constant, their absolute value being varied only by the energy base-line associated with the final state of the oxygen. Therefore taking the ejected oxygen to be a monatomic ideal gas, Table 8-I contains possible reduction reactions for TiO_2 (rutile). The overall enthalpies (ΔH_{298}) and free energies (ΔG_{298}) are also tabulated based on the thermodynamic data |35,39|, listed in Table 8-II.

The thermodynamic quantities are accurately known and as shown are similar for the two references. Enthalpies and free energies per gm-atom oxygen produced for the various reactions are shown graphically in Figure 8.4 as a function

TABLE 8-I Possible TiO_2 reduction reactions

Reaction	ΔH_{298} (Kcal)	ΔG_{298} (Kcal)	$\Delta H_{298}/O(g)$ (Kcal/mole)	$\Delta G_{298}/O(g)$ (Kcal/mole)	$\Delta G_{1500}/O(g)$ (Kcal/mole)	$\Delta H_{1500}/O$ (Kcal/mole)
1. $TiO_2(s) \rightleftarrows Ti(g)+2O(g)$	+456.70	+424.43	+228.35 (+152.23)†	+214.22 (+141.44)†	+174.37 (116.25)†	+198.92 (132.61)†
2. $2TiO_2(s) \rightleftarrows Ti_2O_3(s)+O(g)$	+147.65	+137.73	+147.65	+137.73	+141.22	+153.59
3. $TiO_2(s) \rightleftarrows TiO(s) + O(g)$	+161.15	+150.78	+161.15	+150.78	+151.51	+163.96
4. $3TiO_2(s) \rightleftarrows Ti_3O_5(s)+O(g)$	+149.15	+139.20	+149.15	+139.20	+143.2	+154.08
5. $TiO_2(s) \rightleftarrows Ti(s) + 2O(g)$	+344.60	+323.07	+172.30	+161.53	+162.02	+173.11
6. nil $\rightleftarrows$ Vo + 2_e- +O(g)	+164.9*	---	---	---	---	+164.9

†calculated per gas atom produced

* |77|

TABLE 8-II Thermodynamic data of the System Ti-O

Material	Kubashewski et al |35|		Janaf Tables |39|	
	ΔH^o Kcal/mole	S^o_{298} cal/mole-deg.	$\Delta H^o_f(298)$ K cal/mole	$S^o(298)$ cal/mole-deg.
TiO_2 (rutile)	-225.5±1.0	12.0±0.05	-223.0	12.031
Ti_3O_5(s)	-586.9±1.5	30.9±0.3	(α) -587.75	30.93
			(β) -585.35	33.91
Ti_2O_3(s)	-362.9±0.8	18.83±0.2	-363.49	18.82
TiO(s)	-123.9±0.8	8.3±0.1	(α) -124.19	12.20
			(β) -123.87	12.37
Ti(s)	0	7.3±0.05	(α) 0	7.32
			(β) 1.43	8.69
Ti(g)	+112.1±1.5	43.07	113.00	43.07
O(g) atomic	+ 59.55±0.2	38.48±0.01	59.56	38.47

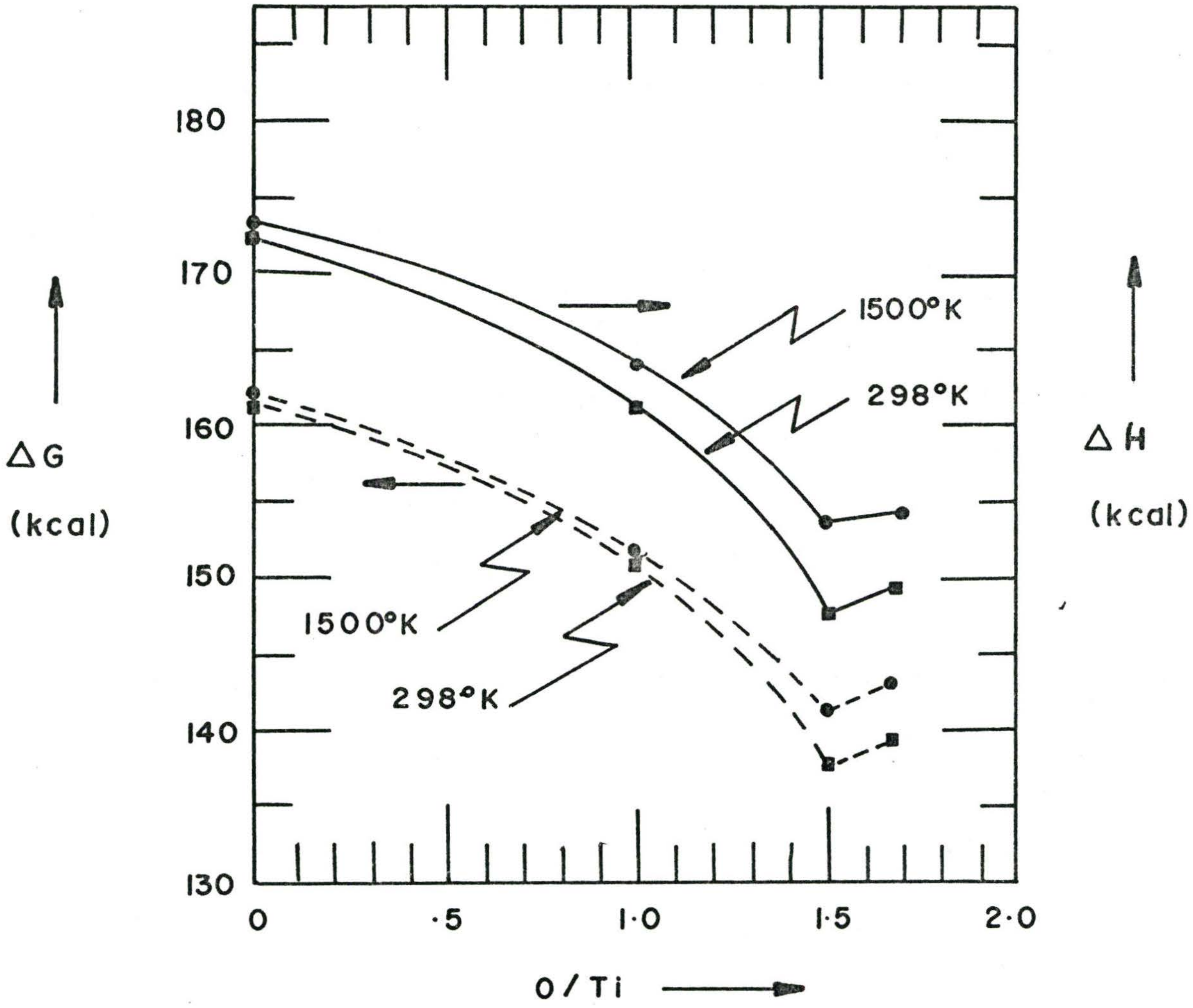

Figure 8.4 The free energy per atomic oxygen associated with producing a lower oxide of TiO_2 with respect to the O/Ti atomic ratio of that lower oxide.

of the O/Ti atomic ratio of the oxide product of the reaction. Two temperatures only were considered 298^{o}K and 1500^{o}K. At 298^{o}K a minimum in both the enthalpy and free energy occurs at the Ti_2O_3 stoichiometry, and this interestingly enough holds for the high temperatures curves as well. Thus provided a mechanism does exist, Ti_2O_3 should have been expected thermodynamically. The validity of this type of approach will be clearer in later work when V_2O_5, MoO_3, Nb_2O_5, and WO_3, oxides which undergo or probably undergo lower oxide generation on ion bombardment, are considered.

SECTION 9

Conclusions

(1) Bombarding TiO_2 with Kr ions induces electrical conductivity changes in the near surface region.

(2) The conductivity (I/V) is ohmic at all but the lowest doses.

(3) The induced (I/V) is permanent at room temperature but anneals out rapidly above 250°C.

(4) The induced (I/V) increases rapidly with ion dose but saturates above 1×10^{17} ions/cm^2.

(5) The effect is not singular to TiO_2 being known to occur also in Nb_2O_5, V_2O_5, MoO_3 and WO_3.

(6) Structural determinations based on electron diffraction patterns suggest the following bombardment sequence:

TiO_2(rutile) → TiO_2(amorphous) → TiO_x(amorphous) → Ti_2O_3 (crystalline)

Thus there is a net oxygen loss from the lattice, though the fate of the lost oxygen is unspecifiable.

(7) Total surface transformation to Ti_2O_3 is consistent with the saturation level of (I/V) since it is well known that Ti_2O_3 has a conductivity greatly in excess of TiO_2.

(8) Gas-release experiments (i.e. annealing in the presence of a radioactive marker) indicated the following sequence for

the damage layer:

$$Ti_2O_3\text{(crystalline)} \rightarrow TiO_x\text{(amorphous)} \rightarrow Ti_4O_7\text{(crystalline)} \rightarrow Ti_nO_{2n-1}\text{(crystalline)}$$

in an inert gas atmosphere.

(9) (I/V) saturation levels increased with target temperature and beam current.

(10) Thickness estimates derived from conductivity measurements, diffraction pattern, and dissolution data suggest a value of ~100 Å for the damaged layer.

(11) Induced (I/V) through Kr bombardment occurs also for single crystal rutile, though at increased dose levels (a factor of 2) and only when the incident beam is not near a low index or channeling direction.

(12) Oxygen bombardment causes minimal (I/V) increases. This may be reconciled either in terms of the difference in sputtering coefficients of Kr and O (3-4 mean atoms/ion for Kr vs .6 mean atoms/ion for O) or in terms of replenishing the lattice with oxygen lost by bombardment.

(13) Predictions based on the extent of ionic character or ionicity are consistent with the observation that TiO_2 amorphizes under ion impact and that Ti_2O_3 is stable to further irradiation.

(14) Thin films of TiO_2 did not exhibit oxygen loss on Kr bombardment but rather the energy deposition results in the transformation of the as deposited amorphous films to rutile.

(15) Oxygen bombardment of evaporated Ti thin films produces the NaCl type monoxide TiO and not Ti_2O_3 as might have been expected. The TiO persisted to doses of 1.4×10^{17} ions/cm^2.

(16) V_2O_5, MoO_3 and TiO_2 exhibit the same <u>type</u> of response in an energetic inert gas beam. The conditions necessary for this phenomena in other systems cannot yet be specified in full, though the following two are fairly obvious:

(i) The cation should be multivalent and a series of suboxides should exist among which some are stable in a radiation environment.

(ii) The starting substance should have a comparable or lower oxygen binding energy than total binding energy.

SECTION 10

Suggestions for Further Research

(1) Bombardment induced oxygen loss is a rather more general phenomenon than had initially been expected. Hence an obvious area of research would include the characterization of the behaviour of such oxides as CuO, Fe_2O_3, MnO_2, Ta_2O_5 and U_3O_8.

(2) Additional experiments should be considered to evaluate the mechanism involved in lower oxide generation and the relative contributions of sputtering and internal collisional processes. For example one might expect sputtering to dominate at the lowest energies and collisional processes at higher energies. Simple measurements of (I/V) versus energy do not distinguish between these.

(3) Since annealing of the Ti_2O_3 damage layer on TiO_2 yielded higher oxides (e.g. Ti_4O_7), the Ti_3O_5 stoichiometry, for example, must exist but is not crystalline. Experiments should be undertaken to induce crystallization to yield this stoichiometry in view of its technological importance.

(4) Many oxides of the Ti-O system where $O/Ti > 1.5$ exhibit semiconductor to metal transitions |67| that have potential device application (e.g. Ti_3O_5), but generally the transition temperatures (T_t) are not suitable. However the

T_t may be modified significantly by the addition of an alloying element, hence altering the lattice parameters and crystal symmetry. A case in point would be VO_2 with additions of W yielding $V_{1-\underline{x}}W_{\underline{x}}O_2$ |68,69|, where, for $\underline{x} = 0$, $T_t = 70^{o}C$ and for $\underline{x} = 0.067$, $T_t = -110^{o}C$. This suggests that bombardment of TiO_2 by an <u>appropriate</u> species could (i) produce a lower oxide having a transition of suitable magnitude and (ii) provide the necessary impurity concentration to alter the T_t to a value of interest.

APPENDIX I

Electron Diffraction Data and Analysis

I.1 Electron diffraction analysis

All structural determinations were based on the analyses of electron diffraction patterns generated in the Philips EM-300 in both the transmission and back reflection (BRD) mode from thin films and bulk samples respectively†. In both cases, interplanar "d" spacings in units of Å were evaluated from the diffraction patterns by applying the relation |41,42|:

$$\lambda L = \frac{R}{|g_{hkl}|} = Rd_{hkl} \tag{I-1}$$

where λL is the camera constant consisting of the product of λ, the wavelength of the impinging electrons as determined by the accelerating voltage, and L, the physical distance in cm from the specimen to the photographic plate. R is the ring radius for polycrystalline ring patterns (or the distance from a chosen spot to the central one in a single crystal spot pattern) and d_{hkl} is the interplanar spacing for the particular reflecting planes {hkl}. "g_{hkl}" is the corresponding point or operating reflection in reciprocal space for those {hkl}

---

† The geometries of the two modes are aptly described by Murr |41|.

reflecting planes |43|. The camera constant λL, was determined by the use of a standard material, in this case polycrystalline Au, to generate a ring pattern from which ring radii were measured. Since the d_{hkl} spacings are easily calculable for Au from the relation for a cubic crystal lattice |43|,

$$d_{hkl} = \frac{a}{\sqrt{h^2 + k^2 + l^2}} \tag{I-2}$$

where a is the lattice constant, λL may be evaluated. Hence if R(cm) is plotted against $1/d_{hkl}$, the slope of the straight line is in fact the camera constant. This is summarized in Figure I.1 for the BRD mode at operating voltages of 60, 80 and 100 KV. The camera constant was verified using the standard Au sample <u>each</u> time before generating patterns with the "unknown"† structures.

The camera constants in the transmission mode were similarly evaluated, however unlike the BRD mode, in transmission the intermediate and diffraction lenses are operational and their currents modify the pattern size, hence λL is specified for the recorded lens current values. Again when generating patterns from unknown crystal structures standard Au <u>thin films</u> were included so as to provide the correct λL for that particular group of patterns.

---

† for <u>non-conducting</u> specimens (e.g. TiO_2) charge build-up was avoided by using a discharge gun.

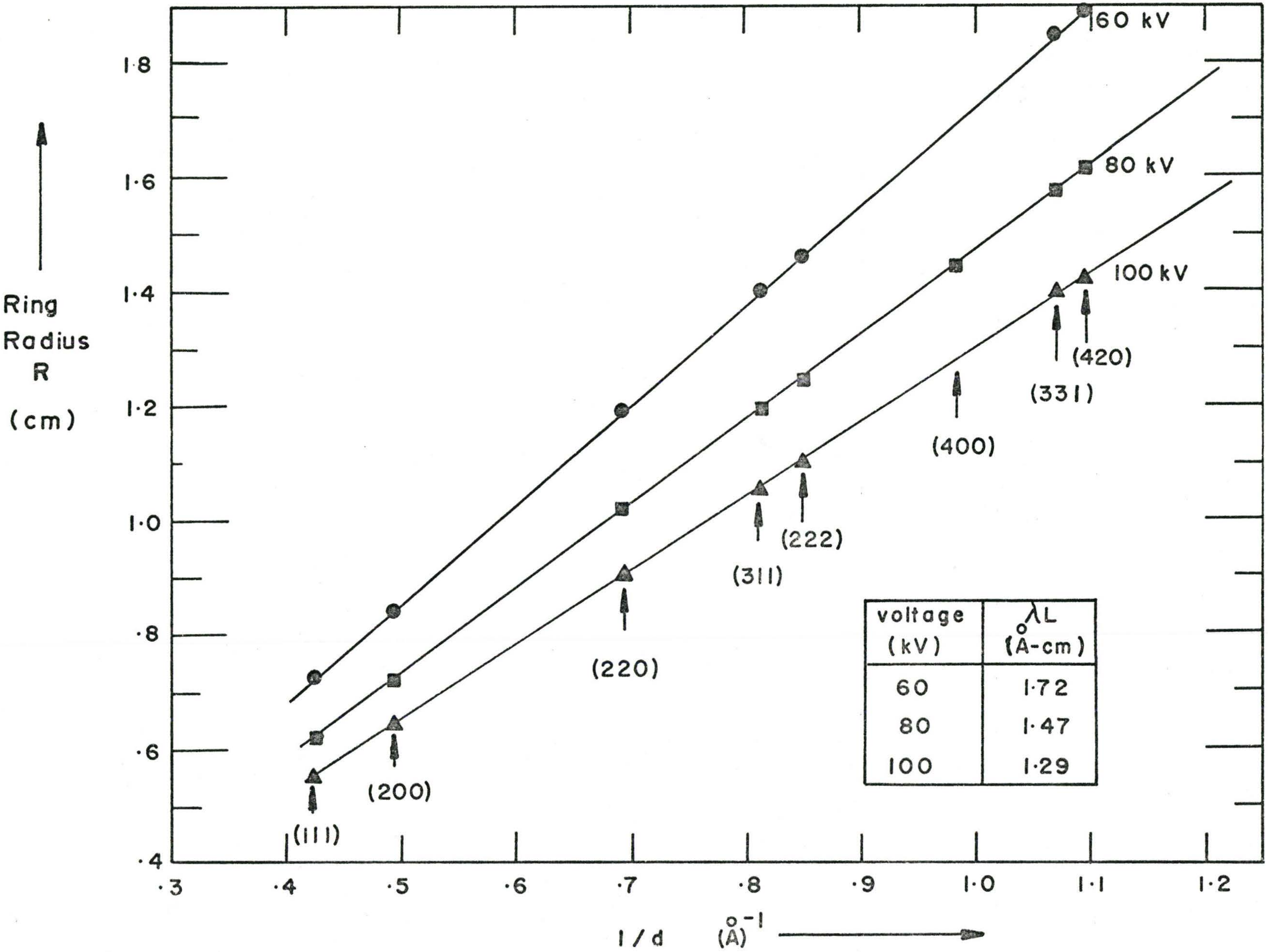

Figure I.1 λL evaluated from Au standard specimens in the Back Reflection Electron Diffraction Mode.

I.2 Polycrystalline ring patterns

Interplanar d spacings for the unknown specimen were evaluated using Equation I.1, where λL was known from the standard and R the ring radii were measured from the "unknown" diffraction pattern. A structural determination was made by comparing these calculated d values with the literature values for all available members of the oxide system. It is noted that the literature data were invariably based on X-ray work |44,45,46| and since the structure factor F, hence the intensities for X-rays and electrons are not quite the same, the comparison of intensities cannot be taken too far. For example some rings which do appear might in principle be forbidden and vice versa. Nevertheless, the comparisons have in all cases been surprisingly adequate, as evidenced by the Au standard (80 KV) diffraction pattern where all the expected rings were present and indexed, where the intensities were remarkably similar between electron and X-ray results and where no extra reflections occurred (Table I-I).

I.3 Single crystal spot patterns

Here analysis consisted of assigning the centre spot as the origin and measuring the distances to the respective spots in the symmetrical array. Evaluation of d spacings and a comparison with literature values inferred the specific operating reflection or set of reflecting planes {hkl} corresponding to each spot. Determination of a consistent set of indices for all the spots, thus identifying the appropriate Laue zone was completed by requiring that in Figure I.2 for

TABLE I-I A comparison of "d" spacings and intensities for electron (BRD) and X-ray diffraction of Au.

Ring #	I/Io (expt'l)† (0-100)	d (expt'l)† (Å)	d (Å) *	I/Io* (0-100)	{hkl}*
1	100	2.35	2.355	100	111
2	70	2.06	2.039	52	200
3	48	1.44	1.442	32	220
4	54	1.23	1.230	36	311
5	19	1.18	1.177	12	222
6	7	1.02	1.020	6	400
7	24	0.935	0.936	23	331
8	22	0.915	0.912	22	420
9	10	0.833	0.833	23	422

† microdensitometer trace data - electron diffraction

* ASTM card #4-0784 - X-ray diffraction

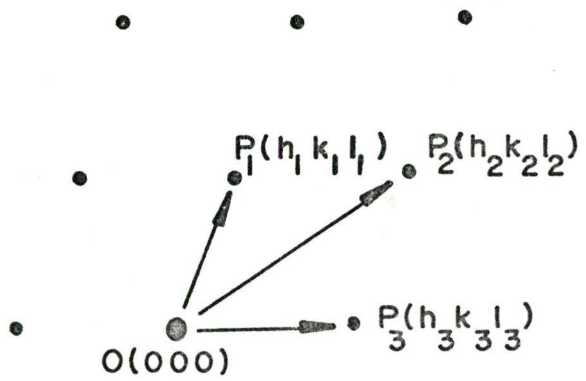

Figure I.2   Indexing a spot pattern

the three spots P_1, P_2, P_3 the following relations hold |42|:

$$\overrightarrow{OP}_1 + \overrightarrow{OP}_3 = \overrightarrow{OP}_2 \qquad (I.3)$$

with respect to the centre spot (000). This necessarily meant that for a correct indexing |42|:

$$(h_1k_1l_1) + (h_3k_3l_3) = (h_2k_2l_2) \qquad (I.4)$$

An example of such an indexing is given in Section 4, Figure 4.2(b) for single crystal rutile.

I.4 Diffraction data/Ti-O system

The following are the available data (first ten d spacings and intensities) on members (17 in number) of the Ti-O system from which structural determinations have been made at the time of writing this thesis. The list is necessarily incomplete as new phases are reported at frequent intervals.

TABLE I-II Diffraction data/Ti-O System

α-Ti*

d(Å)	I
2.56	30
2.34	26
2.24	100
1.73	19
1.48	17
1.33	16
1.28	2
1.25	16
1.23	13
1.17	2
+ etc.	

Ti_2O *

d(Å)	I
4.84	10
2.57	60
2.43	60
2.27	100
1.76	80
1.62	20
1.48	80
1.37	60
1.28	20
1.26	60
+etc.	

$TiO_{\sim 0.65}$ *

d(Å)	I
2.50	80
2.40	80
1.89	40
1.73	60
1.44	60
1.42	40
1.25	40

TiO *(NaCl type)

d(Å)	I
2.42	80
2.09	100
1.48	100
1.26	60
1.21	60

TiO (low temp)*

d(Å)	I
5.59	40
4.45	40
4.14	40
3.76	60
3.32	80
2.95	60
2.79	60
2.77	60
2.44	40
2.42	80
+ etc.	

Ti_2O_3

d(Å)	I
3.74	60
2.71	60
2.58	60
2.24	40
2.12	10
1.87	40
1.70	100
1.64	20
1.51	40
1.49	60

Ti_3O_5*

d(Å)	I
9.45	20
4.72	10
4.28	60
3.55	100
3.44	20
3.35	40
3.33	40
3.31	40
3.15	60
2.85	20
+ etc.	

Ti_3O_5(anasovite) *

d(Å)	I
4.78	60
3.46	100
2.70	100
2.42	60
2.37	40
2.17	60
2.14	20
1.93	80
1.85	100
1.81	40
+ etc.	

---

* |44,45|

Ti-O System (continued)

Ti_4O_7*

d(Å)	I
6.18	20
5.27	40
4.28	80
3.77	40
3.38	100
3.35	40
3.12	40
3.02	100
2.91	60
2.82	100

+ etc.

Ti_5O_9*

d(Å)	I
7.82	20
5.21	40
4.72	20
4.04	80
3.43	20
3.37	100
3.35	20
3.24	40
3.12	40
3.08	100

+ etc.

Ti_6O_{11}*

d(Å)	I
4.97	40
3.90	80
3.37	100
3.25	40
3.12	80
2.97	100
2.84	40
2.69	60
2.63	40
2.59	80

+ etc.

Ti_7O_{13}*

d(Å)	I
4.71	40
3.89	20
3.79	80
3.36	100
3.31	40
3.14	80
3.01	100
2.75	20
2.66	60
2.63	40

+ etc.

Ti_8O_{15}*

d(Å)	I
5.20	40
3.71	80
3.35	100
3.16	80
3.05	100
2.64	60
2.57	80
2.51	80
2.49	80
2.42	40

+ etc.

Ti_9O_{17}*

d(Å)	I
5.00	20
4.35	20
3.65	80
3.36	40
3.35	80
3.21	40
3.17	80
3.07	80
2.92	20
2.90	20

+ etc.

TiO_2 (brookite)†

d(Å)	I
3.51	100
3.47	80
2.90	90
2.73	4
2.48	25
2.41	18
2.37	6
2.34	4
2.33	4
2.30	6

+ etc.

TiO_2 (anatase)‡

d(Å)	I
3.52	100
2.43	20
2.38	60
2.34	20
1.89	80
1.70	60
1.67	60
1.50	20
1.48	60
1.37	20

+ etc.

* |44,45|

† ASTM card #16-617

‡ ASTM card #4-0479

Ti-O System (continued)

TiO_2 (rutile)[‡]

d(Å)	I
3.25	80
2.49	60
2.30	20
2.19	40
2.06	40
1.69	80
1.63	60
1.48	40
1.45	40
1.36	40

+ etc.

[‡] ASTM card #4-0563

APPENDIX II

Electrical Conductivity Measurement Technique

II.1 General

The electrical conductivities of the pellet specimens were measured using a linear four-point D.C. probe† technique similar to |48,49,50|, for which the experimental arrangement is schematically shown in Figure II.1. Measurements consisted in passing a known direct current I, through the outer pair of probes and measuring the potential V, across the inner pair of probes. Thus, the effective conductivity (I/V) in units of ohm^{-1} was evaluated. An average value of (I/V) was established from 18 separate measurements by changing the polarity, magnitude of I and probe head position on the pellet. Varying I also served as a verification of the ohmic behaviour of the specimens. Only two specimen geometries were considered: (i) a semi-infinite volume of material (Valdes case 1)and (ii) a conducting layer of thickness W, on a non-conducting substrate where $W << S$ (Valdes case 7), when evaluating the bulk conductivities in units of $\text{ohm}^{-1}\text{-cm}^{-1}$ from the measured values.

---

† A.M. Fell (Mfg) Ltd., Sussex, England.

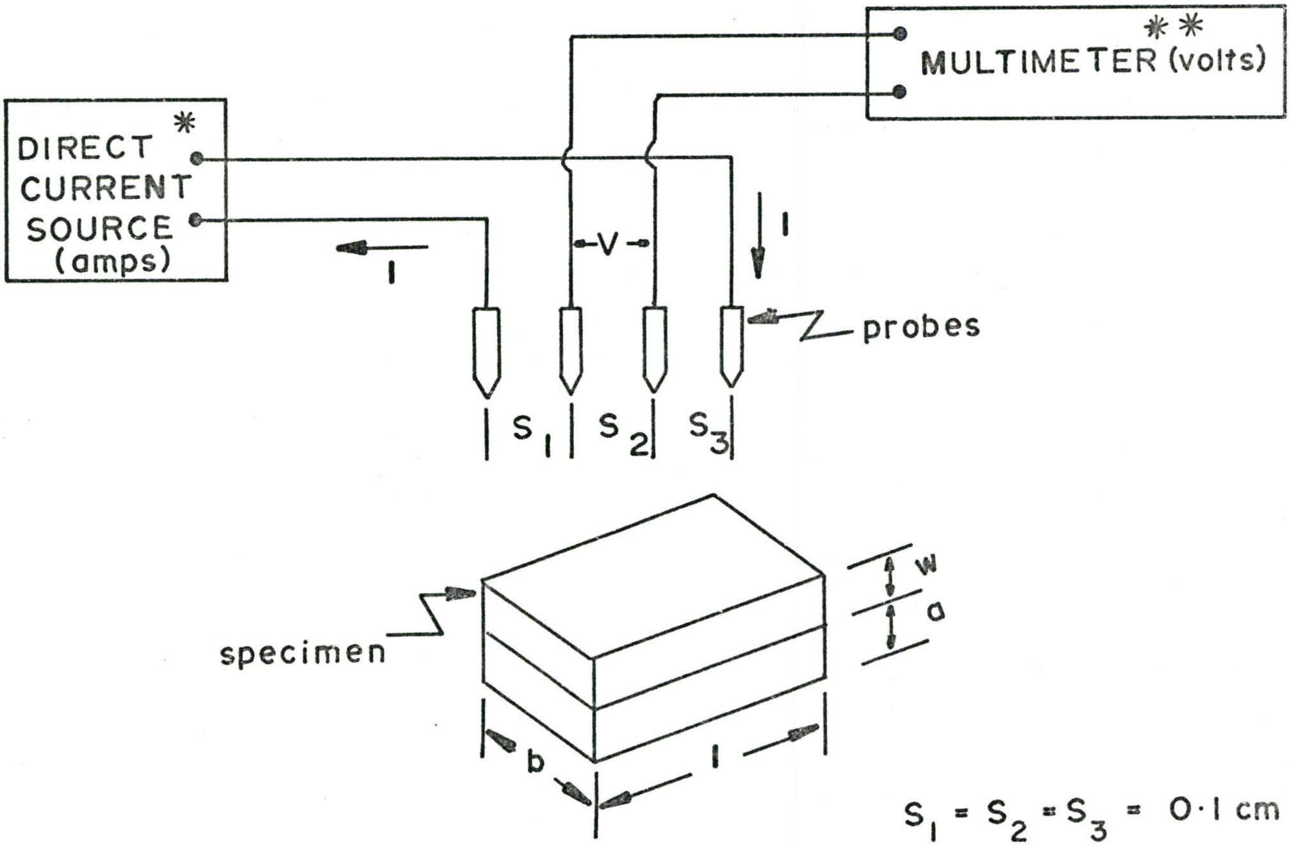

Figure II.1 Schematic of conductivity measurement method; S_1, S_2, S_3 are the inter-probe spacings; W is the conducting thickness; a, b, and l are the specimen dimensions where generally W << S (after Valdes |48|).

* Keithley Model 225

** Keithley Model 160 - Input Resistance = 10 megohms.

II.1.1 Semi-infinite volume of material (no W exists):

This was the case for a homogeneous unbombarded pellet, for which the conductivity relation is:

$$\sigma_o = \frac{I}{2\pi V}\left[\frac{1}{S_1} + \frac{1}{S_2} - \frac{1}{S_1+S_2} - \frac{1}{S_2+S_3}\right] \qquad \text{(II.1)}$$

Since the probe spacings S_1, S_2, S_3 were equal, the equation II.1 simplifies to:

$$\frac{1}{\rho_o} = \sigma_o = \frac{1}{2\pi S}(I/V) \qquad \text{(II.2)}$$

I = known current through the outer probes (amps)

V = floating potential difference between the inner probes (volts)

S = probe spacing (0.1 cm)

σ_o = (bulk) conductivity ($\text{ohm}^{-1}\text{cm}^{-1}$)

ρ_o = (bulk) resistivity (ohm-cm)

II.1.2 A very thin layer W, on a non-conducting substrate (W<<S):

This was the case for a surface altered layer on a pellet induced by ion bombardment, for which the electrical conductivity relation is:

$$\frac{1}{\rho} = \sigma = \sigma_o \cdot G_7\left(\frac{W}{S}\right) \qquad \text{(II.3)}$$

where W and S have their usual meaning, σ_o is given by equation II.2, and $G_7(\frac{W}{S})$ is the correction factor for the new geometry. Since the altered layer was only of the order of 100 Å thick[†] therefore W<<S and $G_7(\frac{W}{S})$ approaches the

---

[†] Estimates in the text of this thesis (e.g. dissolution) establish a W of approximately 100 Å.

limiting expression for an "infinitely thin" conducting layer;

$$G_7\left(\frac{W}{S}\right) = \frac{2S}{W} \ln 2 \qquad \text{(II.4)}$$

whence,

$$\frac{1}{\rho} = \sigma = \sigma_o \frac{2S \ln 2}{W} = \frac{I \ln 2}{V \pi W} \qquad \text{(II.5)}$$

where W is in cm.

Since the altered layer geometry is of interest in this investigation, Figure II.2 has included the variation of $G_7(\frac{W}{S})$ with W, the altered layer thickness in Å units. The figure also includes the calculated bulk conductivity (σ) (± 1 standard deviation) from Equation II.5 assuming an average saturation (I/V) of 1×10^{-4} ohm^{-1} which is the case for the high dose 30 KeV Kr bombardment of polycrystalline rutile pellets.

II.2 Correction for the porosity of sintered pellets

Bulk density determinations of pellets sintered at 1280°C revealed approximately .05 volume fraction of pores. Therefore the electrical conductivity measurements should be corrected by a factor defined by the Loeb equation |51|:

$$\sigma_c = \sigma_m \left[1 + \left(\frac{p}{1-p^{2/3}}\right)\right] \qquad \text{(II.6)}$$

where σ_c = corrected conductivity (ohm^{-1}-cm^{-1})

σ_m = measured conductivity (ohm^{-1}-cm^{-1})

p = volume fraction pores

However, for small percentage porosities, the correction is small (typically less than the error involved in measuring the electrical conductivity due to ion beam

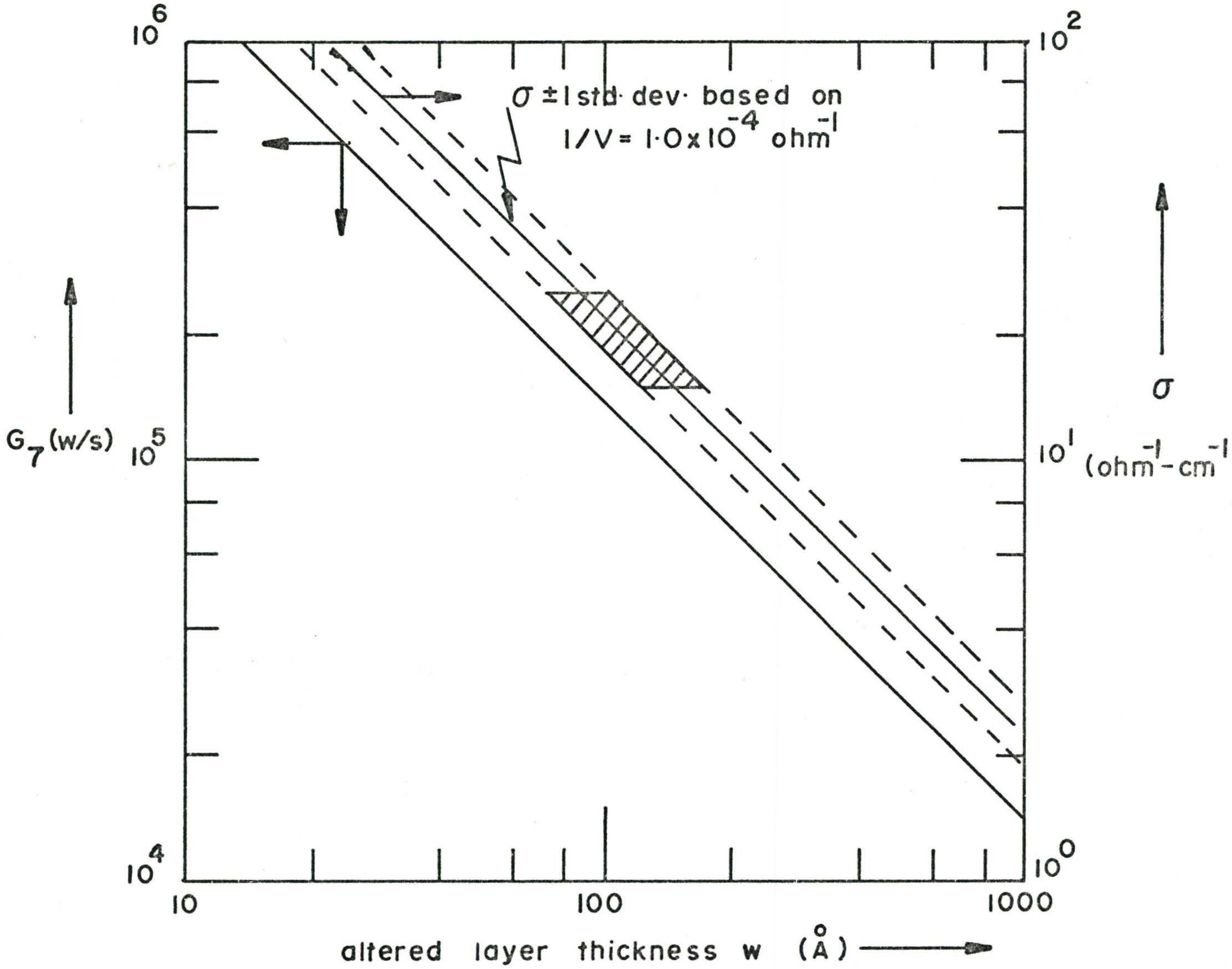

Figure II.2 G_7 $(\frac{W}{S})$ and bulk conductivity (σ) variation with altered layer thickness, w.

inhomogenieties) and hence has been neglected for the pellets fired for 24 hours at 1280°C.

APPENDIX III

Heavy-ion Accelerator

III.1 General

Irradiations of all specimens whether thin films or pellets, were carried out in a heavy ion accelerator, with a 77 megahertz, radio frequency ion source capable of producing ion beams of energies from 0 to 40 KeV and currents 0 to 50 μA. In these experiments the heavy ion beams were confined to inactive Kr and radioactive (Kr^{85}) krypton, and oxygen.

Focussing was achieved using five electrostatic lenses. The vacuum system, consisting of a roughing pump, oil diffusion pump, and liquid nitrogen cold trap to prevent oil contamination of the specimen surface, provided operating specimen chamber pressures of typically $10^{-5} - 10^{-6}$ Torr. There was no mass separation, however since only heavy ions or oxygen were the bombarding species this problem is not significant. Also although the energy spread of the r-f ion source is large (20 - 100 eV) |38| all bombardments were of high energy (i.e. - 30 KeV) hence this error was negligible. The ion bombardment apparatus and peripheral equipment are shown in Figure III.1.

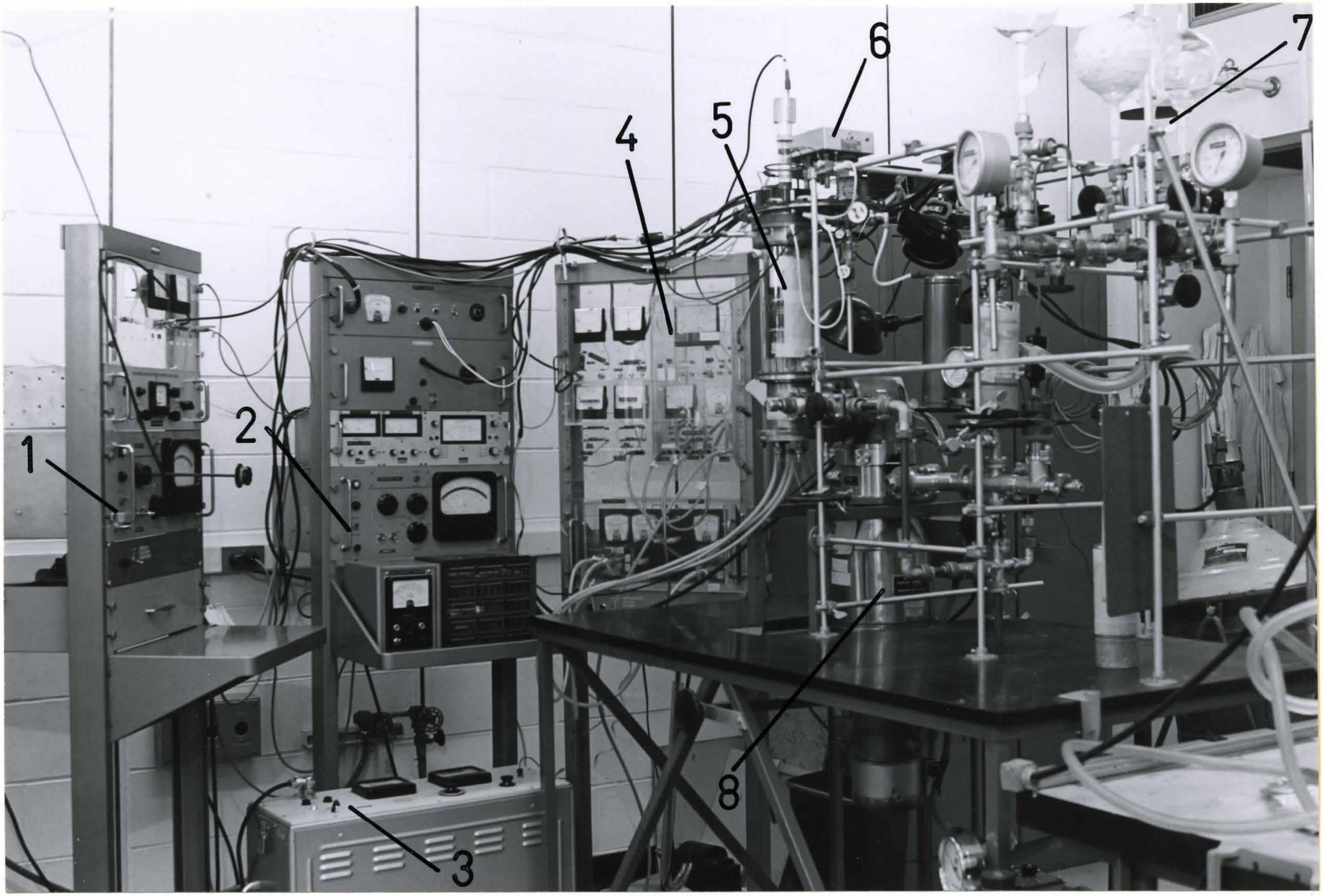

Figure III.1 Ion Acceleration and peripheral equipment; 1 - Focusing system; 2 - Extraction power supply; 3 - High voltage supply; 4 - Current and Voltage meters; 5 - Specimen chamber; 6 - R.F. ion source; 7 - gas supplies; 8 - vacuum system.

III.1.1 Dose (fluence) determination

Property changes induced by ion bombardment are generally characterized as a function of the ion dose (number density of incident ions on the target material) for which (a) the ion beam current portion of the total current in the accelerator and (b) the beam area must be known. For the measured I to represent only the ions and not the backstreaming electrons, electron suppression in the form of a Faraday Cage was used with an applied potential of 850V, 425V on each of the aperture and shutter. Previous investigation |52| established this condition as effectively eliminating the electron component of the total current.

The beam area was known by confining it to a fixed diameter (usually 1.5 cm). This was accomplished by "painting" the edge of a 1.5 cm diameter circular specimen holder with a fluorescent screen material in this case Zn_2SiO_4 with 20% Na_4SiO_4 thus enabling the beam to be adjusted manually to 1.5± .1 cm. In addition, this large beam size relative to sample size avoided the problem of charge buildup of the initially non-conductive TiO_2 pellets by producing secondary electrons from ion impact with the aluminium sample holder.

Thus the ion dose or fluence follows as:

$$\text{dose(fluence)} = \frac{It}{A} \qquad \text{(III.1)}$$

where I is the ion current to the target in μamp, t is the duration of bombardment in minutes, and A is the ion beam area in cm^2.

Doses calculated from equation III.1 in units of μamp-min/cm^2 may be readily transformed to ions/cm^2 realizing that 1 μamp-min/cm^2 = 3.74×10^{14} ions/cm^2.

The errors involved in this determination are characteristically quite large. Though beam size errors represent a significant portion of the overall error (5-10%) the greatest error is introduced by beam instabilities and discharge fluctuations which are inevitable during long irradiations (1½ hr). In conjunction with beam inhomogenieties, the uncertainty in the total dose is typically of the order of 20 %.

III.2 Specimen target stages

Figure III.2 illustrates the room temperature specimens holder stage used, which could be altered by changing specimen holders for single crystals, thin films and powders. Several experiments were carried out with a high temperature stage (to 600°C), which is aptly described elsewhere |52|, and with a low temperature stage, which is shown in Figure III.3. The design was basically that of the room temperature stage, but in addition the copper target was cooled by a copper rod immersed in liquid nitrogen, and shielded from contamination by a copper disc similarly cooled by liquid nitrogen. A chromel-alumel thermocouple served to measure actual target temperature.

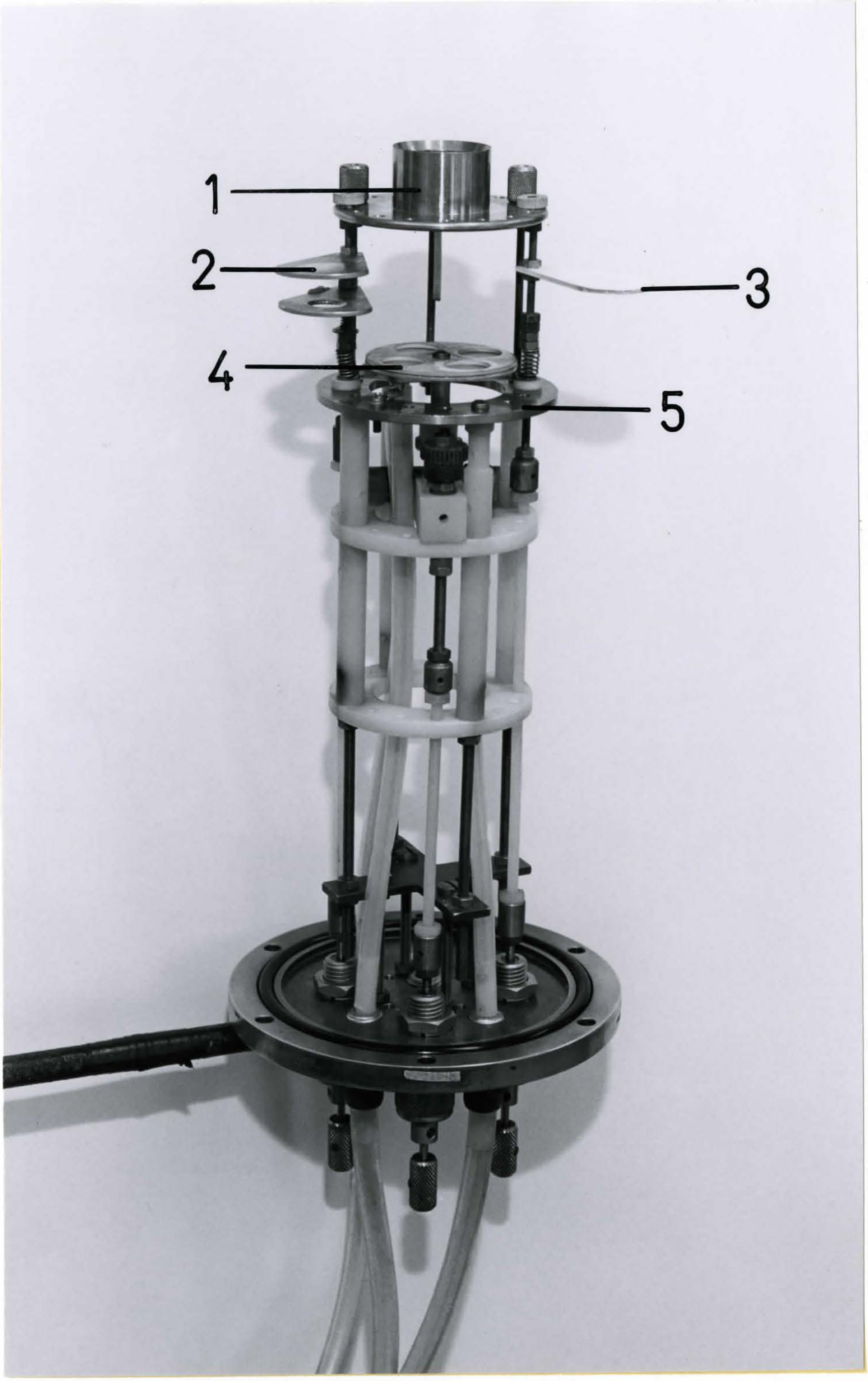

Figure III.2 R.T. target stage; 1 - upper part of Faraday cage; 2 - shutter; 3 - fluorescent screen; 4 - rotatable high voltage target and sample holder; 5 - lower part of Faraday cage.

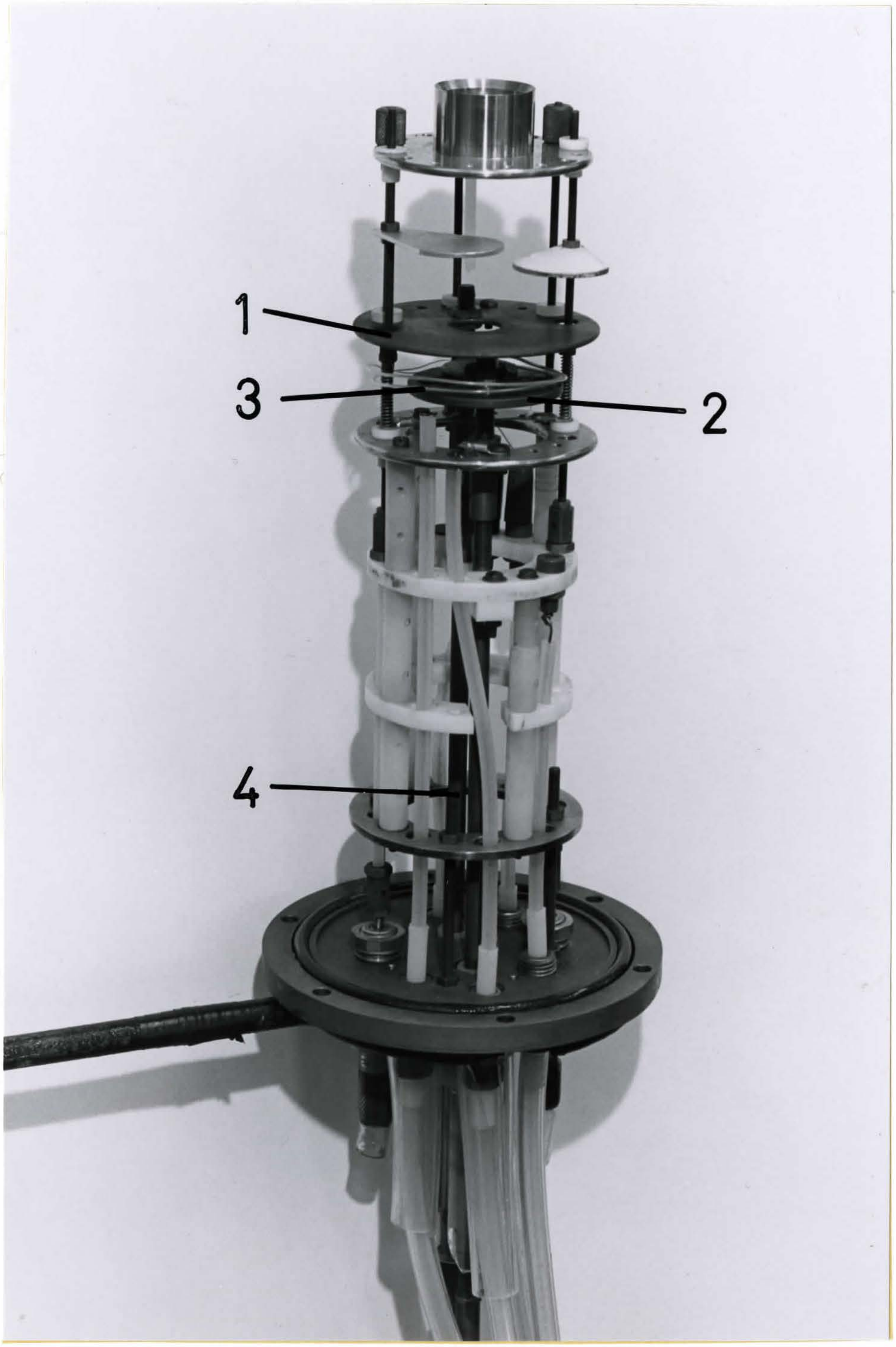

Figure III.3 Low temperature target stage; 1 - copper cooling disc; 2 - copper target and sample holder; 3 - chromel-alumel thermocouple; 4 - copper rods to conduct heat away from the target by immersion in liquid nitrogen.

APPENDIX IV

Gas Release Experimental Apparatus

In order to investigate the nature of the Ti_2O_3 surface layer, gas release experiments similar to |53| were conducted. The technique involves irradiating a specimen to produce the desired property change and then labelling with an appropriate radioactive isotope of the bombarding species. The specimen is then heated at a constant rate (generally 25 C°/min) in a regulated flow of inert gas (usually He). As the specimen heats the damaged region transforms and as the various damage-annealing mechanisms occur the radioactive label is released. The rate of released label is then monitored by means of a G.M. counter above a chamber through which the gas flows. The experimental arrangement is given in Figure IV.1 with a schematic of the specimen holder in Figure IV.2. In these particular experiments the label was $_{36}Kr^{85}$ which decays via a β^- mode of energy 0.67 MeV and has a half-life of 10.8 years |55|.

Since there was a "time lag" between release of "label" and the registration of the event at the G.M. counter, it was necessary to calibrate the apparatus for a specific inert gas flow. This was accomplished by labelling a commercially pure Al ($T_m = 660^oC$) sample with $_{36}Kr^{85}$ and

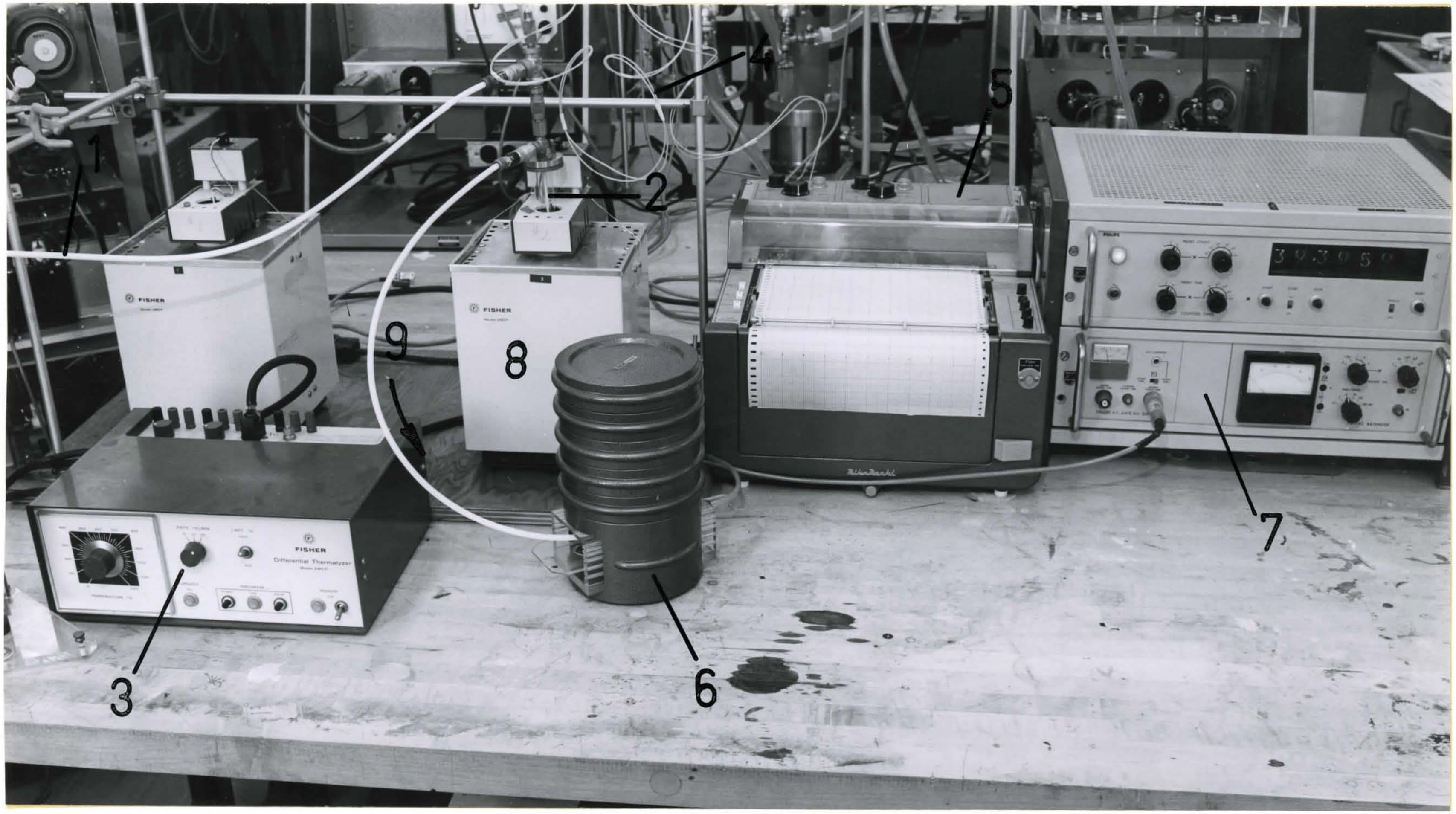

Figure IV.1 Gas Release Apparatus; 1 - Inert Gas supply; 2 - Specimen chamber; 3 - furnace temperature programmer; 4 - chromel-alumel thermocouple; 5 - recorder; 6,7 - G.M. counter system; 8 - furnace; 9 - direction of gas flow.

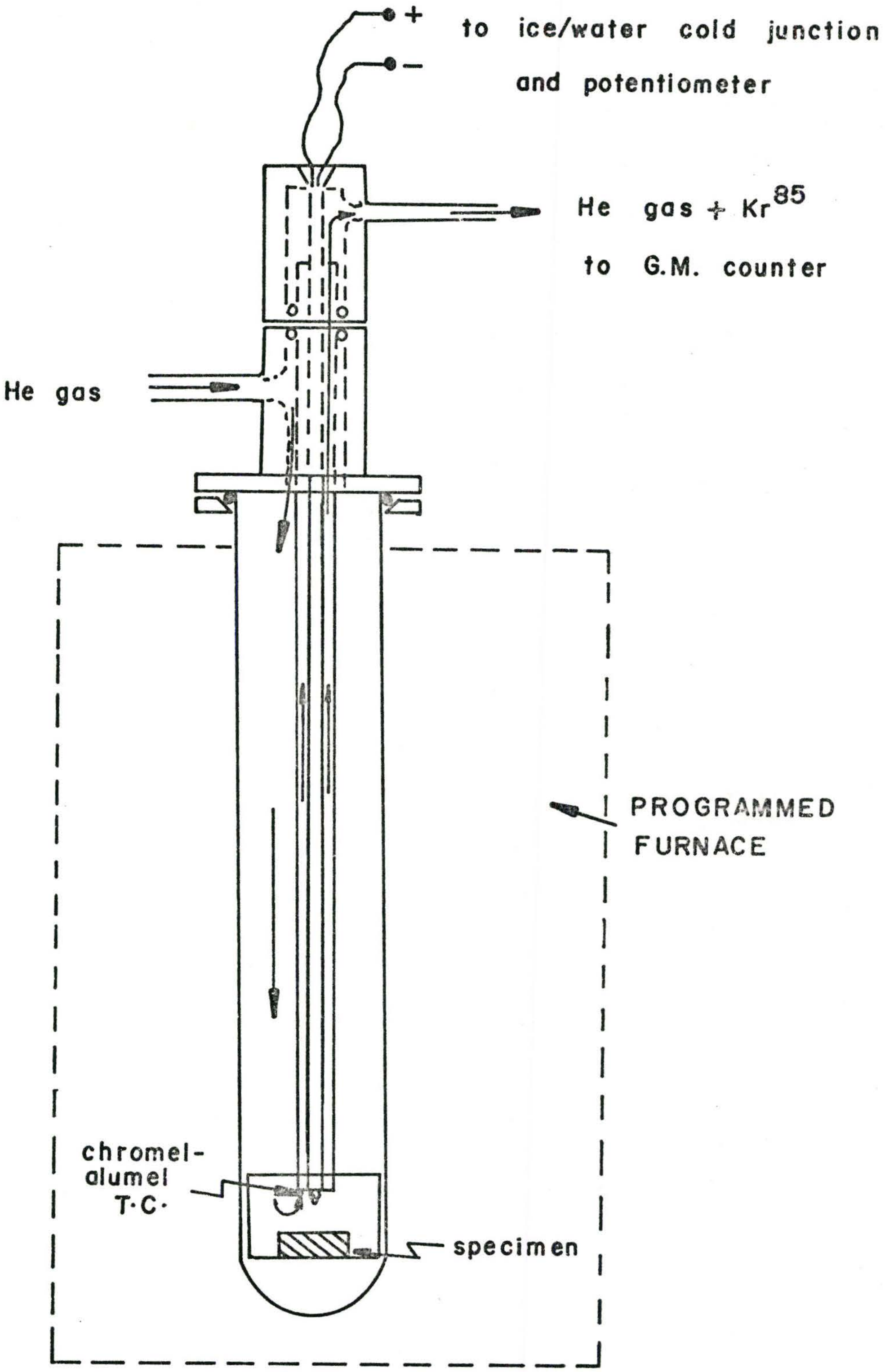

Figure IV.2 Gas release specimen chamber.

evaluating the gas release curve of activity versus temperature. Since the majority of the gas is released on melting (c.f. peak 5 Figure IV.3) the time lag is readily found and in this case was equivalent to 49C^o as shown in Figure IV.3. The extra peaks 1, 2, 3 and 4 in the gas release spectrum are believed to be due to fortuitous interstitial positioning of inert gas enabling it to readily escape, annealing of radiation damage and volume diffusion as described in |54| and hence will not be discussed further here.

Although the gas release technique is somewhat indirect as a method of probing the TiO_2 surface alteration induced by ion bombardment, nevertheless, gas release experiments coupled with electron diffraction data provide a surprisingly detailed understanding of the formation and annealing of gross structural radiation damage[†]|56|.

[†] For example, the peak at 600-700°C in the gas release spectrum of α-Al_2O_3 bombarded with 40 KeV Kr is associated with an amorphous-crystalline transition |53,57|.

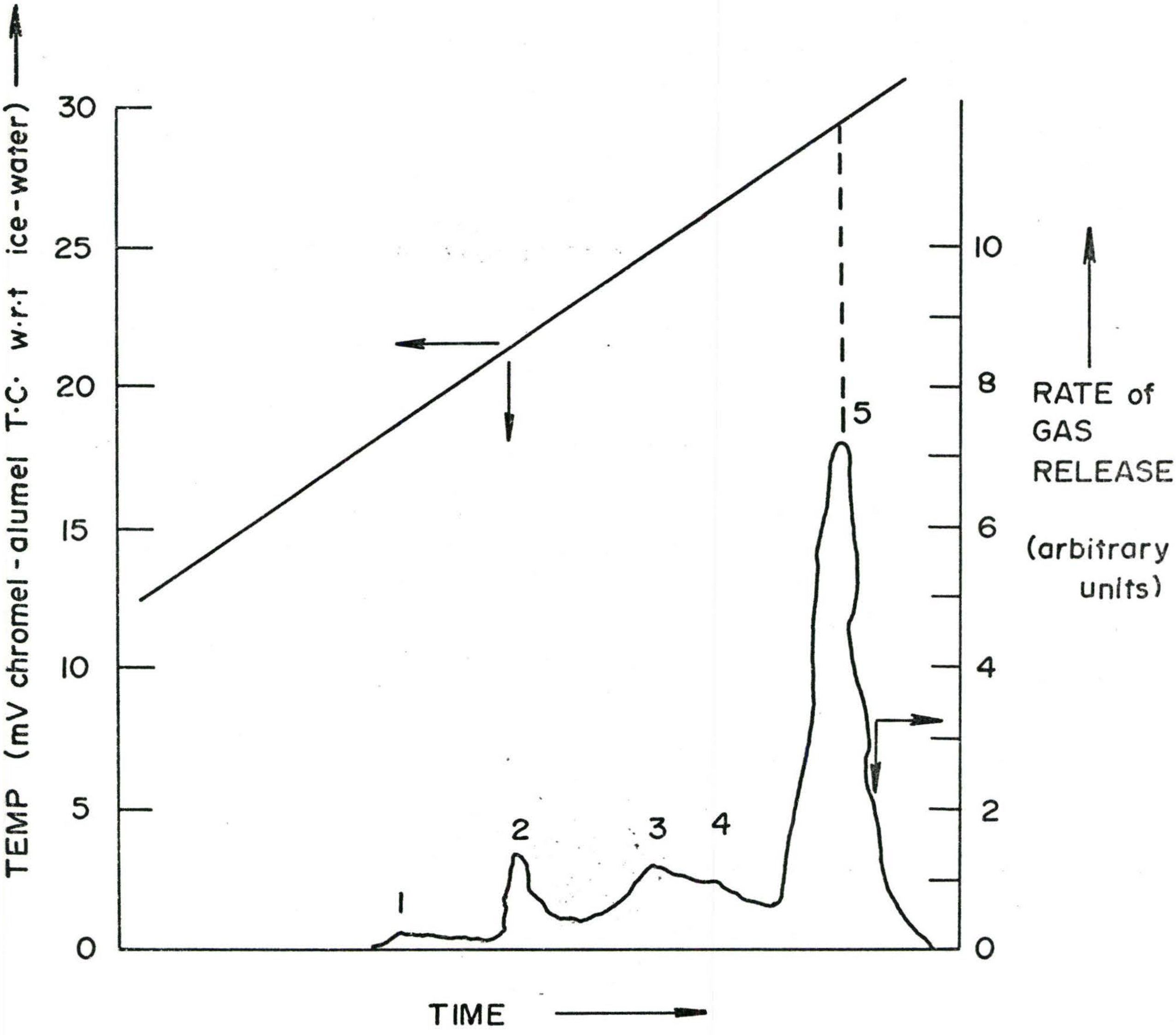

Figure IV.3 Temperature and gas release vs time, Pt 5 represents the gas release from labelled Al on melting and occurs at a temperature of 709°C (29.5 mV w.r.t. ice water cold junction, chromel-alumel thermocouple). Since pure Al melts at 660°C, the time lag (corresponding to specimen chamber to counter time) is equivalent to 49C°.

APPENDIX V

Single Crystal Rutile Orientation Determination

V.1 Laue method

The orientation, and in particular the normal to the bombarded surface, of the TiO_2 single crystals was determined by the back reflection X-ray diffraction technique using "white" radiation from a copper tube operated at a potential of 30 kV and a current of 20 mA.

The crystal was mounted with the prepared face (i.e. the face to be ion bombarded) perpendicular to the X-ray beam, thus parallel to the photographic plate. The specimen film distance was the usual 3 cm |43|, hence the pattern was analysable using a standard Greninger chart. A stereographic projection of the resultant spot pattern was made where spots of the same zone were joined along "great" circles and the corresponding poles plotted. These poles should then be low index and may be identified by measuring the angles between pole pairs and comparing these with the known interplanar angles for plane pairs of the form $\{h_1k_1l_1\} - \{h_2k_2l_2\}$. However rutile is tetragonal, $\alpha = \beta = \gamma = 90^\circ$ but $a = b \neq c$. Therefore interplanar angles are dependent upon the specific material and are not generally available unlike the cubic system where the interplanar angle values are fixed and tabulated |43,58|.

V.2 Calculating interplanar-angles (in degrees) for rutile between planes of the form $\{h_1k_1l_1\}$ and $\{h_2k_2l_2\}$.

Interplanar angles were calculated using a computer program |59|. The modified version with explanatory comment cards used to generate a table of interplanar angles is included (Section V.4.1). The calculation is based on the fact that the angle ϕ between any two planes $(h_1k_1l_1)$ and $(h_2k_2l_2)$ of spacings d_1 and d_2 respectively is equal to the angle between the corresponding reciprocal lattice vectors r_1^* and r_2^* (i.e. the respective plane normals). That is, forming the dot product defines the appropriate angle ϕ;

$$r_1^* \bullet r_2^* = |r_1^*|\ |r_2^*| \cos\phi \qquad \text{(V-1)}$$

from which, for all crystal systems,

$$\begin{aligned}\cos\phi = \{&h_1h_2a^{*2} + k_1k_2b^{*2} + l_1l_2c^{*2} + (h_1k_2+h_2k_1)a^*b^* \cos\gamma^* \\ &+ (k_1l_2 + k_2l_1)b^*c^* \cos\alpha^* + (l_1h_2 + l_2h_1)c^*a^*\cos\beta\} \\ &d_1d_2 \qquad \text{(V-2)}\end{aligned}$$

where a^*, b^*, c^*, α^*, β^* and γ^* are the reciprocal space analogs of a,b,c, α,β and γ respectively, the crystal lattice parameters |58|.

V.2.1 Input data: The data consisted of the crystal system, tetragonal, and the crystal parameters |ASTM card #4.0553|:

$$a = b = 4.954\ \text{Å};\ c = 2.958\ \text{Å}$$

$$\alpha = \beta = \gamma = 90^{\circ}$$

Included also were two control parameters to limit the maximum value of any Miller index to 3 and to limit the sum of (h+k+l) to less than 5. Although these were arbitrarily chosen, low index planes are usually the only ones of interest in indexing Laue patterns.

V.2.2 Output: A table of pairs of planes and their associated interplanar angles were compiled as shown on the following printout (Section V.4.2).

V.3 Orientation determination: A set of measured interplanar angles were compared with the output of V.4.2 and a subsequent consistent indexing was determined that indicated the normal to the prepared face to be <100>, and was consistent with the electron diffraction pattern for single crystal rutile (c.f. Figure 4.2(b)).

```
C      PROGRAM TO GENERATE INTER-PLANAR ANGLES FOR ANY CRYSTAL SYSTEM
C      ORIGINAL PROGRAM BY H.C.CHAO TO ANALYSE LAUE DATA
C      PROGRAM MODIFIED BY T.PARKER TO CALCULATE INTERPLANAR ANGLES ONLY
C      THE ANGLE PHI BETWEEN PLANES (H1,K1,L1) AND (H2,K2,L2)OF
C      SPACINGS D1 AND D2 IS EQUAL TO THE ANGLE BETWEEN THE
C      RECIPRICOL LATTICE VECTORS R1* AND R2* THAT ARE NORMAL TO THESE
C      THEREFORE R1*.R2* =R1*R2* COS(PHI)
C      AND HENCE PHI MAY BE CALCULATED FROM THE EQUATION IN
C      THE SUBROUTINE ANGLE
       DIMENSION N(100),TEMP(25),D(25,25,16),G(15,15),IP(15)
       COMMON NONREC,ANRSQ1,ANRSQ2,S11.FJH2,S22,FK1,FK2,S33,FL1,FL2,FJH1,
      1S23,S13,S12,VOL,RSQRT1,RSQRT2,ASQD,BSQD,CSQD,JS,TEMP,D,G,EMATCH,JY
      2ES, M5, TMP
C      READ IN TNE MAX VALUE OF ANY MILLER INDEX(JBIG)
C      READ IN MAXSUM THE MAX VALUE OF THE SUM OF H+K+L
C      READ IN THE CRYSTAL SYSTEM AND MATERIAL
 9999 READ(5,52) JBIG,MAXSUM,SYSTEM,SYST
   52 FORMAT (2I6, 2A4)
      IF (JBIG) 9998, 120, 9998
C      PRINT OUT THE CRYSTAL SYSTEM AND MATERIAL
 9998 WRITE(6,3333) SYSTEM,SYST
 3333 FORMAT (3X, 73H660228 PROJECT 20.012-029 TEXTURE STRENGTHENING  H.
     1C.CHAO DIV.12 EXT 6372, 2X, 2HZZ///19X, 23HTABLE OF ANGLES FOR THE
     2, 2A5, 1CHSYSTEM AND/18X, 43HSET OF POLES FROM BACK REFLECTION LAU
     3E DATA//)
C      CONVERTING RADIANS TO DEGREES
  100 PIBY2=0.5*3.14159265
      PIB180 = PIBY2/90.
      JYES = 0
C      INITIALIZING H K L VALUES
      JH1=0
      K1=0
      L1=0
      JSUM=0
      I1=1
      MA = MAXSUM - 1
      WRITE(6,521) JBIG,MA
  521 FORMAT(5X,25HLIMIT OF A MILLER INDEX =, I6, /5X,42HLIMIT OF THE
     1SUM OF THE MILLER INDICES =, I6)
C      READING IN CRYSTAL INFORMATION A.B.C,ALPHA,BETA,GAMMA
C      NONREC IS THE NO OF NON RIGHT ANGLES
      READ(5,53) NONREC,A,B,C,ANGA,ANGB,ANGG
   53 FORMAT (I6,3F6.3,3F7.2)
C      PRINTING OUT CRYSTAL INFORMATION
      WRITE(6,531) NONREC,A,B,C,ANGA.ANGB,ANGG
  531 FORMAT (5X,37HNO. OF NON-RECTANGLES IN UNIT CELL  =, I6///10X, 3HA
     1 =, F6.3, 8X, 3HB =, F6.3, 9X, 3HC =, F6.3/6X, 7HALPHA =, F7.2, 4X
     2, 6HBETA =, F7.2, 4X, 7HGAMMA =, F7.2//)
C      IF ALL ANGLES ARE 90 THEN JRECT IS 1,IF NOT JRECT IS 0
      IF (NONREC) 55,54,55
   54 JRECT = 1
      GO TO 551
   55 JRECT = 0
C      JAB,JAC,JBC EXPRESS THE RELATIONSHIPS BETWEEN THE ANGLES AND AXES
C      FOR INSTANCE IF JAB=1 A=B,ALPHA=BETA= 90
  551 IF(A-B) 555,552,555
  552 IF(ANGA-90.) 555,553,555
  553 IF(ANGB-90.) 555,554,555
  554 JAB=1
```

```
      GO TO 56
  555 JAB=0
   56 IF (A-C) 60,57,60
   57 IF (ANGA-90.) 60,58,60
   58 IF(ANGG-90.) 60,59,60
   5  JAC=1
      GO TO 61
   60 JAC=0
   61 IF (B-C) 65,62,65
   62 IF (ANGB-90.) 65,63,65
   63 IF (ANGG-90.) 65,64,65
   64 JBC=1
      GO TO 101
   65 JBC=0
C     THE FOLLOWING SEQUENCE SELECTS PLANES OF INTEREST
C     DUPLICATION OF PLANES IS AVOIDED
C     PLANES ARE LISTED IN ARRAY N(I1) AS 3 DIGIT NUMBERS
  101 L1=L1+1
      JSUM=JSUM+1
      IF(JSUM-MAXSUM) 1014,1011,1014
 1011 L1= 0
      K1=K1+1
      JSUM=JH1+K1
      IF(JSUM-MAXSUM) 1014,1012,1014
 1012 K1=0
      JH1=JH1+1
      JSUM=JH1
      IF(JH1-(JBIG-1)) 1014,1013,1014
 1013 I0=I1-1
      GO TO 102
 1014 J0=L1
      IF(L1)  1017,1015,1017
 1015 J0=K1
      IF(K1) 1017,1016,1017
 1016 J0=JH1
      IF(JH1-1) 101,1017,101
 1017 IF(JAB) 402,402,401
  401 IF (JH1-K1) 402,402,101
  402 IF(JAC) 404,404,403
  403 IF (JH1-L1) 404,404,101
  404 IF(JBC)406,406,405
  405 IF (K1-L1) 406,406,101
  406 IF (J0-1) 1019,1019,407
  407 M=JH1/J0
      IF(J0*M-JH1)1019,408,1019
  408 M=K1/J0
      IF(J0*M-K1) 1019,101,1019
 101  N(I1)=100*JH1+10*K1+L1
C     PRINT OUT THE SELECTED PLANES
      WRITE(6,10) N(I1)
   10 FORMAT (1X, 1H(, I4, 1H))
      I1=I1+1
      GO TO 101
  102 WRITE(6,11)
   11 FORMAT(5X,24HEND OF SELECTING PLANES )
      WRITE(6,450)
  450 FORMAT (//1X, 13H( HKL)-( UVW), 8X, 27HINTERPLANAR ANGLE (DEGREES)
     129X, 2HZZ/)
```

```
C     CALCULATING THE SQUARES OF UNIT CELL DIMENSIONS
      ASQD=A*A
      BSQD=B*B
      CSQD=C*C
      IF(NONREC-1) 1022,1021,1022
C     CALCULATING COSINES OF UNIT CELL ANGLES AND THE SQUARES
 1021 COSA = COS(PIB180*ANGA)
      COSB = COS(PIB180*ANGB)
      COSG = COS(PIB180*ANGG)
      COSSQA=COSA*COSA
      COSSQB=COSB*COSB
      COSSQG=COSG*COSG
      S11=BSQD*CSQD*(1.-COSSQA)
      S22=ASQD*CSQD*(1.-COSSQB)
      S33=ASQD*BSQD*(1.-COSSQG)
      S12=A*B*CSQD*(COSA*COSB-COSG)
      S13=A*BSQD*C*(COSG*COSA-COSB)
      S23=ASQD*B*C*(COSB*COSG-COSA)
C     CALCULATING VOLUME OF UNIT CELL
      VOL=ASQD*BSQD*CSQD*(1.-COSSQA-COSSQB-COSSQG+2.*COSA*COSB*COSG)
C     ASSIGNING VALUES TO H,K,L
 1022 DO 109 I1= 1,I0
      ANO=N(I1)
      JH1=ANO/100.
      FJH1=JH1
      ANO=ANO-FJH1*100.
      K1=ANO/10.
      FK1=K1
      L1=ANO-FK1*10.
      FL1=L1
      IF(NONREC) 581,580,581
C     RSQRT1 =INTERPLANAR SPACING FOR AN ALL RIGHT ANGLE SYSTEM
  580 RSQRT1=1./SQRT(FJH1*FJH1/ASQD+FK1*FK1/BSQD+FL1*FL1/CSQD)
  581 DO 109 I3=I1,I0
      ANO=N(I3)
      JH2=ANO/100.
      FJH2=JH2
      ANO=ANO-FJH2*100.
      K2=ANO/10.
      FK2=K2
      L2=ANO-FK2*10.
      FL2=L2
      JS=0
      IF(JAB) 613,613,611
  611 IF(JH2-K2) 612,613,612
  612 JFLPAB=1
      GO TO 614
  613 JFLPAB=0
  614 IF(JAC) 617,617,615
  615 IF(JH2-L2) 616,617,616
  616 JFLPAC=1
      GO TO 618
  617 JFLPAC=0
  618 IF(JBC) 621,621,619
  61  IF(K2-L2) 620,621,620
  620 JFLPBC=1
      GO TO 622
  621 JFLPBC=0
```

```
  622 IF(NONREC) 104,623,104
  623 RSQRT2=1./SQRT(FJH2*FJH2/ASQD+FK2*FK2/BSQD+FL2*FL2/CSQD)
  104 IF(NONREC-1) 105,1041,105
C     ANRSQ1 AND 2 ARE D SPACINGS CORRESPONDING TO THE TWO PLANES
C     IN A SYSTEM WHERE THE ANGLES ARE NOT ALL 90
 1041 ANRSQ2=SQRT(VOL/(S11*FJH2*FJH2+S22*FK2*FK2+S33*FL2*FL2+
     1         2.*(S12*FJH2*FK2+S13*FJH2*FL2+S23*FK2*FL2)))
  105 IF(NONREC-1) 1052,1051,1052
 1051 ANRSQ1=SQRT(VOL/(S11*FJH1*FJH1+S22*FK1*FK1+S33*FL1*FL1+
     1         2.*(S12*FJH1*FK1+S13*FJH1*FL1+S23*FK1*FL1)))
 1052 FJH3=FJH2
      FK3=FK2
      FL3=FL2
      CALL ANGLE
      IF(JFLPAB) 1054,1054,1053
 1053 FJH2=FK3
      FK2=FJH3
      FL2=FL3
      CALL ANGLE
 1054 IF(JFLPAC) 1056,1056,1055
 1055 FJH2=FL3
      FK2=FK3
      FL2=FJH3
      CALL ANGLE
 1056 IF(JFLPBC) 1058,1058,1057
 1057 FJH2=FJH3
      FK2=FL3
      FL2=FK3
      CALL ANGLE
 1058 IF(JFLPAB) 2592,2592,1059
 1059 IF(JFLPAC) 2592,2592,2591
 2591 FJH2=FK3
      FK2=FL3
      FL2=FJH3
      CALL ANGLE
      FJH2=FL3
      FK2=FJH3
      FL2=FK3
      CALL ANGLE
 2592 FJH2=FJH3
      FK2=FK3
      FL2=FL3
  107 FL1=-FL1
      IF (FL1) 105,1071,1071
 1071 FK1=-FK1
      IF (FK1) 105,1072,1072
 1072 FJH1=-FJH1
      IF (FJH1) 105,1001,1001
 1001 IF (NONREC) 1002,108,1002
 1002 FL2=-FL2
      IF (FL2) 104,1003,1003
 1003 FK2=-FK2
      IF (FK2) 104,1004,1004
 1004 FJH2=-FJH2
      IF (FJH2) 104,108,108
  108 IF(JS-16) 1081,125,125
 1081 JS=JS+1
      TEMP(JS)=100.
```

```
C       THE OUTPUT  GIVES THE TWO PLANES AFTER WHICH ARE LISTED
C       THE CORRESPONDING INTERPLANAR ANGLES
        WRITE(6,770) N(I1),N(I3),(TEMP(I4),I4=1,JS)
   770  FORMAT (1X,1H(,I4,3H)-(,I4,1H),5F10.2/14X,5F10.2/14X,5F10.2)
    10  CONTINUE
   125  CONTINUE
   120  STOP
        END
        SUBROUTINE ANGLE
        DIMENSION TEMP (25), D(25,25,16), G(15,15)
        COMMON NONREC,ANRSQ1,ANRSQ2,S11,FJH2,S22,FK1,FK2,S33,FL1,FL2,FJH1,
       1S23,S13,S12,VOL,RSQRT1,RSQRT2,ASQD,BSQD,CSQD,JS,TEMP,D,G,EMATCH,JY
       2ES, M5, TMP
        IF (NONREC) 35,36,35
    35  COSPHI= ANRSQ1*ANRSQ2*(S11*FJH1*FJH2+S22*FK1*FK2+S33*FL1*FL2
       1+S23*(FK1*FL2+FK2*FL1)+S13*(FL1*FJH2+FL2*FJH1)+S12*(FJH1*
       1FK2+FJH2*FK1))/VOL
        GO TO 38
    36  COSPHI= RSQRT1*RSQRT2*(FJH1*FJH2/ASQD+FK1*FK2/BSQD+FL1*FL2/CSQD)
    38  IF(COSPHI) 40,39,40
    3   PHI = 90.
        GO TO 43
    40  IF (ABS(COSPHI)-.99999) 42,42,41
    41  PHI = 0.
        GO TO 43
    42  TANPHI = SQRT(1./(COSPHI * COSPHI) - 1.)
        PHI = 57.29583* ATAN(TANPHI)
    43  IF (JS) 44,45,44
    44  DO 46 I4 = 1,JS
        IF(PHI-(TEMP(I4)+1.E-04)) 47,46,46
    47  IF(PHI-(TEMP(I4)-1.E-04)) 46,46,48
    46  CONTINUE
    45  JS = JS + 1
        IF (JS-17) 49,48,48
    49  TEMP(JS) = PHI
    48  RETURN
        END

   3      5 TET-TIO2
   0 4.594 4.594 2.958   90.00   90.00   90.00


                                   CD TOT    0273
```

V.4.2

```
              TABLE OF INTERPLANAR ANGLES FOR
              TETRAGONAL TIO2


   LIMIT OF A MILLER INDEX =      3
   LIMIT OF THE   SUM OF THE MILLER INDICES =      4
   NO. OF NON-RECTANGLES IN UNIT CELL   =      0


      A = 4.594          B = 4.594            C = 2.958
   ALPHA =  90.00     BETA =  90.00     GAMMA =  90.00


    PLANES CONSIDERED

(    1)
(   10)
(   11)
(   12)
(   13)
(   21)
(   31)
(  110)
(  111)
(  112)
(  120)
(  121)
(  130)
   END OF SELECTING PLANES


( HKL)-( UVW)          INTERPLANAR ANGLE (DEGREES)

(    1)-(    1)      0.00     100.00
(    1)-(   10)     90.00     100.00
(    1)-(   11)     32.78     100.00
(    1)-(   12)     17.85     100.00
(    1)-(   13)     12.11     100.00
(    1)-(   21)     52.17     100.00
(    1)-(   31)     62.63     100.00
(    1)-(  110)     90.00     100.00
(    1)-(  111)     42.32     100.00
(    1)-(  112)     24.48     100.00
(    1)-(  120)     90.00     100.00
(    1)-(  121)     55.22     100.00
(    1)-(  130)     90.00     100.00
(   10)-(   10)      0.00      90.00     100.00
(   10)-(   11)     57.22      90.00     100.00
(   10)-(   12)     72.15      90.00     100.00
(   10)-(   13)     77.89      90.00     100.00
(   10)-(   21)     37.83      90.00     100.00
(   10)-(   31)     27.37      90.00     100.00
(   10)-(  110)     45.00     100.00
(   10)-(  111)     61.57     100.00
(   10)-(  112)     72.96     100.00
(   10)-(  120)     26.57      63.44     100.00
(   10)-(  121)     42.73      68.45     100.00
```

```
(  10)-( 130)     18.43     71.57    100.00
(  11)-(  11)      0.00     45.02     65.55    100.00
(  11)-(  12)     14.93     36.84     50.62    100.00
(  11)-(  13)     20.66     34.71     44.89    100.00
(  11)-(  21)     19.39     58.96     84.95    100.00
(  11)-(  31)     29.85     67.26     84.59    100.00
(  11)-( 110)     67.49    100.00
(  11)-( 111)     28.43     68.66    100.00
(  11)-( 112)     22.51     52.66    100.00
(  11)-( 120)     61.04     75.99    100.00
(  11)-( 121)     28.68     47.27     85.30     73.69    100.00

(  11)-( 130)     59.10     80.14    100.00
(  12)-(  12)      0.00     25.03     35.69    100.00
(  12)-(  13)      5.73     21.46     29.96    100.00
(  12)-(  21)     34.32     54.28     70.01    100.00
(  12)-(  31)     44.78     64.05     80.48    100.00
(  12)-( 110)     77.49    100.00
(  12)-( 111)     31.82     56.09    100.00
(  12)-( 112)     17.04     39.06    100.00
(  12)-( 120)     74.09     82.12    100.00
(  12)-( 121)     39.81     49.04     71.46     64.50    100.00

(  12)-( 130)     73.10     84.44    100.00
(  13)-(  13)      0.00     17.07     24.23    100.00
(  13)-(  21)     40.06     53.15     64.28    100.00
(  13)-(  31)     50.52     63.29     74.74    100.00
(  13)-( 110)     81.47    100.00
(  13)-( 111)     34.63     51.46    100.00
(  13)-( 112)     17.95     24.07    100.00
(  13)-( 120)     79.18     84.62    100.00
(  13)-( 121)     44.61     50.59     66.20     61.27    100.00

(  13)-( 130)     78.52     86.20    100.00
(  21)-(  21)      0.00     67.90     75.66    100.00
(  21)-(  31)     10.46     73.62     65.20    100.00
(  21)-( 110)     56.05    100.00
(  21)-( 111)     33.95     85.56    100.00
(  21)-( 112)     37.85     70.93    100.00
(  21)-( 120)     45.05     69.32    100.00
(  21)-( 121)     21.55     50.21     76.68     86.57    100.00

(  21)-( 130)     41.47     75.54    100.00
(  31)-(  31)      0.00     77.80     54.74    100.00
(  31)-( 110)     51.10    100.00
(  31)-( 111)     40.30     85.25    100.00
(  31)-( 112)     47.26     80.90    100.00
(  31)-( 120)     37.41     66.60    100.00
(  31)-( 121)     23.85     53.95     67.04     86.33    100.00

(  31)-( 130)     32.60     73.69    100.00
( 110)-( 110)      0.00     90.00    100.00
( 110)-( 111)     47.68     90.00    100.00
( 110)-( 112)     65.52     90.00    100.00
( 110)-( 120)     18.43     71.57    100.00
( 110)-( 121)     38.81     74.95    100.00
( 110)-( 130)     26.57     63.44    100.00
( 111)-( 111)      0.00     84.64     56.86    100.00
```

```
( 111)-( 112)       17.84       66.80       47.71      100.00
( 111)-( 120)       50.30       77.71      100.00
( 111)-( 121)       18.85       84.10       75.70       53.37      100.00

( 111)-( 130)       52.97       72.48      100.00
( 112)-( 112)        0.00       48.96       34.08      100.00
( 112)-( 120)       66.85       82.47      100.00
( 112)-( 121)       32.64       78.68       65.70       51.19      100.00

( 112)-( 130)       68.25       79.32      100.00
( 120)-( 120)        0.00       36.87       53.13       90.00      100.00

( 120)-( 121)       34.78       48.92       60.48       90.00      100.00

( 120)-( 130)        8.13       45.00       81.87      100.00
( 121)-( 121)        0.00       30.11       69.56       77.63       85.45
                    71.01       43.10      100.00
( 121)-( 130)       35.60       54.50       83.33      100.00
( 130)-( 130)        0.00       53.13       36.87       90.00      100.00


                              CD TOT    0136
```

REFERENCES

1. C. M. Drum, Phys. Stat. Sol. 9, 635(1965).
2. S. M. Davidson and G. R. Booker, Radiation Effects, 6, 33-43(1970).
3. N. Q. Lam and Roger Kelly, Can. J. Phys. 50, 17, 1887-1895(1972).
4. M. D. Matthews, AERE-R 6802, Harwell, May (1971).
5. H. M. Naguib and Roger Kelly, J. Nucl. Materials, 35, 293-305(1970).
6. B. Navinšek, Proceedings of the International Summer School on the Physics of Ionized Gases, Split, Yugoslavia (1972).
7. J. H. Evans, Nature, 229, 5284, 403-404(1971).
8. H. M. Naguib and Roger Kelly, J. Phys. Chem. Solids, 33, 1751-1759(1972).
9. L. B. Griffiths, Nature 188, 43(1960).
10. P. J. Harrop et al, Proc. Brit. Ceram. Soc., 9, 279(1967).
11. L. N. Cojocaru, Radiation Effects, 1, 11-13(1969).
12. J. R. MacEwan and R. R. Meadowcroft, J. Nucl. Materials, 40, 311-324(1971).
13. J. J. Trillat and K. Mihama, C. R. Acad. Sc. 248,(1959).
14. M. Meyer et al, C. R. Acad. Sc. 268,(1969).
15. J. J. Trillat et al, C. R. Acad. Sc. 261 (1965).
16. D. C. Cronemeyer, Phys. Rev. 87, 5, 876-886(1952).

17. D. B. Rogers et al, Inorg. Chem. 8, 841-849(1969).

18. K. Murti, McMaster University (unpublished).

19. T. Parker, McMaster University (unpublished).

20. L. A. Bursill and B. G. Hyde, Phil. Mag. 20, 164, 347-359(1969).

21. F. J. Morin, Phys. Rev. Lett. 34, 3(1959).

22. J. Yahia and H.P.R. Frederiske, Phys. Rev. 123, 1257(1961).

23. J. M. Honig and T. B. Reed, Phys. Rev. 174, 3, 1020-1026 (1968).

24. C.N.R. Rao et al, J. Solid State Chem. 3, 83-88(1971).

25. H. K. Eastwood et al, Appl. Phys. Lett. 20, 2(1970).

26. K. Gamo et al, Japan J. Appl. Phys. 10, 523-525(1971).

27. W. S. Johnson and J. F. Gibbons "L.S.S. - Projected Range Statistics in Semiconductors", Stanford University (1969).

28. H. S. Carslaw and J. C. Jaegar , "Conduction of Heat in Solids", Oxford University Press (1959).

29. J. Lindhard et al, Mat. Fys. Medd. Dan. Vid. Selsk . 33 , 14(1968).

30. Roger Kelly, Can. J. Phys. 46, 473-482(1968).

31. M. Shiojiri, Memoirs of the Faculty of Industrial Arts, Kyoto Tech. Univ., Science and Technology, Vol. 16.

32. L. Pauling, "Nature of the Chemical Bond" 4th Edition, Cornell Univ. Press (1967).

33. W. Gordy and W.J.O. Thomas, J. Chem. Phys. 34, 439(1956).

34. S. S. Batsanov, Russian Chem. Rev. 37 (5), (1968).

35. O. Kubaschewski et al, "Metallurgical Thermochemistry", Pergamon Press (1967).

36. A. Van den Bosch, J. Phys. Chem. Solids, 25, 1293-1304 (1964).

37. D. B. Carroll and H. K. Birnbaum, J. Appl. Phys. 36, 9 (1965).

38. G. Carter and J. S. Colligon ,"Ion Bombardment of Solids", 425-441, Heinemann Educational Books Ltd., London (1968).

39. Janaf Thermochemical Tables, 2nd Edition, D.R. Stull and H. Prophet, June (1971).

40. G. R. Piercy et al, Can. J. Phys. 42, 1116-1134(1964).

41. L. E. Murr,"Electron Optical Applications in Materials Science", McGraw-Hill Inc., Toronto (1970).

42. P.B. Hirsch et al."Electron Microscopy of Thin Films", Butterworth & Co.(Publishers)Ltd., London (1969).

43. B. D. Cullity, "Elements of X-ray Diffraction", Addison-Wesley Publishing Co.Inc., (1967).

44. S. Anderssonet al, Acta Chem. Scand. 11, 1653-1657(1957).

45. S. Anderssonet al, Acta Chem. Scand. 11, 1641-1652(1957).

46. S. Andersson and L. Jahnberg, Arkiv. för Kemi. Band. 21, nr 39, 413(1963).

47. T. Parker and R. Kelly, Proc. Third Intern. Conf. on Ion-implantation in Semiconductors (Yorktown Heights, N.Y. 1972).

48. L. B. Valdes, Proc. I.R.E. 42, 420 (1954).

49. F. M. Smuts, Bell Systems Technical Journal 37,(1958).

50. A. Uhlir, Jr., Bell Systems Technical Journal, 34, 105(1955).

51. R. R. Willardson et al, J. Inorg. Nucl. Chem. 6, 19(1958).

52. I. Reid, Masters Thesis, McMaster University, submitted (1971).

53. Č. Jech and Roger Kelly, J. Phys. Chem. Solids, 30, 465-474(1969).

54. Roger Kelly and Č. Jech, J. Nucl. Materials 30, 122-123 (1969).

55. Handbook of Physics and Chemistry, The Chemical Rubber Publishing Co., (1969-70).

56. Hj. Matzke, Can. J. Phys. 46, 621-634(1968).

57. Hj. Matzke and Whitton, Can. J. Phys. 44,(1966).

58. C. S. Barrett and T. B. Massalski, "Structure of Metals", McGraw-Hill Co., New York (1966).

59. D. T. Champ and J. A. Clum, Trans. Met. Soc. of A.I.M.E. 236, 1952-3(1966).

60. R. Kelly, N.Q. Lam, D.K. Murti, H.M. Naguib and T. E. Parker, Proc. Intern. Summer School on Physics of Ionized Gases, (Split, Yugoslavia,1972) (in press).

61. K. B. Winterbon, P. Sigmund and J.B. Sanders, Kgl. Danske Videnskab. Selskab., Mat.-Fys.Medd. 37, no. 14(1970).

62. E. Gillam, J. Phys. Chem. Sol. 11, 55(1959).

63. R. S. Nelson, Phil. Mag. 11, 291(1965).

64. R. Kelly and N. Q. Lam, Rad. Effects (in press).

65. J. H. Crawford, Jr., and M. C. Wittels, Proc. Int. Conf. on Peaceful Uses of Atomic Energy (United Nations) Vol.7, 654(1956).

66. R. G. Ward, "An Introduction to the Physical Chemistry of Iron and Steel Making", Edward Arnold (Publishers) Ltd. (1962).

67. R. E. Mills et al, "Critical Phenomenon in Alloys, Magnets and Superconductors", 567, McGraw Hill Publishers.

68. M. Israelson and M. Nygren; Mat. Res. Bull. Vol. 4, 881 (1969).

69. M. Israelson and L. Kihlborg; Mat. Res. Bull. Vol. 5, 19(1970).

70. P. D. Townsend et al, Proc. Brit. Ceram. Soc., 1, 71-83 (1964).

71. T. Kawakubo et al, J. Phys. Soc. Japan 15, 2102(1960).

72. D. Onderdelinden, Can. J. Phys. 46, 449(1968).

73. H. M. Naguib, Ph.D. Thesis, McMaster University (1971).

74. N. Q. Lam, Ph.D. Thesis, McMaster University (1971).

75. H. E. Schiøtt, Univ. of the Aarhus, Denmark (personal communication to R. Kelly)

76. M. Meyer, P. Haymann and J. J. Trillat, Growth of Crystals, 8, 120-124(1969).

77. P. Kofstad, "Nonstoichiometry, Diffusion and Electrical Conductivity in Binary Metal Oxides", Wiley-Interscience, New York, 1972.